

Department of Physics and Astronomy

University of Heidelberg

Master thesis

in Physics

submitted by

Felix Hahne

born in Emmendingen

2020

Investigation of a Novel Method for Sympathetic Laser Cooling of Highly Charged Ions in a Penning Trap

This Master thesis has been carried out by Felix Hahne

at the

Max-Planck-Institut für Kernphysik, Saupfercheckweg 1, 69117

Heidelberg, Germany

under the supervision of

Prof. Dr. Klaus Blaum & Dr. Sven Sturm

Untersuchung einer Neuartigen Methode zur Sympathetischen Laserkühlung von Hochgeladenen Ionen in einer Penningfalle

Das Penningfallenexperiment ALPHATRAP testet die Quantenelektrodynamik durch Messung des g -Faktors gebundener Elektronen in hochgeladenen Ionen (HCI). Die Präzision der Messung lässt sich durch Kühlung des HCIs verbessern. Diese Arbeit beschreibt eine neuartige und vielseitige Methode, um hochgeladene Ionen mit lasergekühlten Berylliumionen in einer Hochpräzisions-Penningfalle effizient sympathetisch zu kühlen. Die Methode basiert darauf, die Kopplung zweier in getrennten Penningfallen gespeicherter Ionen unter Hinzunahme eines elektrischen Schwingkreises zu erhöhen. Dies wird in zwei Messungen anhand eines $^{84}\text{Kr}^{23+}$ und $^{40}\text{Ar}^{11+}$ Ions demonstriert: In der Ersten wiesen wir ein *avoided crossing* der Ionenmoden nach, in der Zweiten zeigten wir eine Rabi-Oszillation im Energieaustausch. Unsere Kopplungstechnik ermöglicht eine aktive Kontrolle der Kopplungsstärke zwischen den Ionen, so dass eine Kopplungszeit von $\tau = 0.856(16)$ s erreicht werden konnte. Wir sehen darin ein mögliches Werkzeug eine Vielzahl von Ionenarten effizient zu kühlen.

Zusätzlich wurde im Rahmen dieser Arbeit eine aktive Strahlstabilisierung installiert, um Schwankungen der Position und Orientierung des Kühllasers zu reduzieren und die Ausrichtung des Kühllasers in Bezug auf die Berylliumionen zu verbessern. Dieses System wurde kalibriert und die geometrischen Verluste der Lasertransmission durch unseren Penningfallen-Aufbau abgeschätzt.

Investigation of a Novel Method for Sympathetic Laser Cooling of Highly Charged Ions in a Penning Trap

The Penning trap experiment ALPHATRAP tests quantum electrodynamics via g -factor measurements of bound electrons in highly charged ions (HCI). The precision of the measurements can be improved by cooling the HCI. This thesis describes a novel and versatile method to sympathetically cool HCIs with laser-cooled beryllium ions efficiently in high-precision Penning traps. The method is based on increasing the coupling of two ions stored in separate penning traps by adding an electrical tank circuit. In a proof of principle measurement this was demonstrated using a $^{84}\text{Kr}^{23+}$ and $^{40}\text{Ar}^{11+}$ ion: first, we saw an avoided crossing of the ion modes, and second, we showed a Rabi oscillation in the energy transfer. Our coupling technique enables active control of the coupling strength between the ions, so that a coupling time of $\tau = 0.856(16)$ s was achieved. We see this as a possible tool to efficiently cool a wide range of ion species.

In addition, an active beam stabilization system was installed to reduce fluctuations of the cooling laser beam position and orientation, and to improve the alignment of the laser with respect to the beryllium ions. This system was calibrated and geometric losses of the laser transmission through our Penning trap setup were estimated.

Contents

1	Introduction	1
2	The Penning trap	3
2.1	Description of the Ideal Penning Trap	3
2.2	The Confined Motion	4
2.3	The Real Penning Trap	6
2.4	Frequency Detection of the Ion	9
2.4.1	Image Current Detection with a Tank Circuit	9
2.4.2	The Resonator Line Shape Model	12
2.4.3	The Line Shape Model Including the Ion	12
2.5	Ion Excitation and Sideband Coupling	16
2.5.1	Dipole Excitation	16
2.5.2	Quadrupole Sideband Coupling	16
3	The Experimental Setup	18
3.1	Outer Trap Setup - Magnet and Cryostat	18
3.2	The Inner Trap Tower	20
3.2.1	Capture Trap - CT	20
3.2.2	Precision Trap - PT	21
3.2.3	Analysis Trap - AT	21
3.3	Laser System	22
3.4	Mm-Wave and Laser Beam Injection	22
4	Laser Beam Stabilization	26
4.1	Calibration	27
4.2	Performance	29
4.3	Trap Transmission	30
5	Ion-Ion Coupling	34
5.1	Motivation for an Alternative Sympathetic Cooling Technique in a Penning Trap	34
5.2	Effective Resonator Model	36
5.3	Interaction of Two Ions Coupled via a Common Resonator	37
5.3.1	Tuning C_{eff}	39
5.3.2	Avoided Crossing Line Shape	41
5.4	The Proof of Coupling Measurement	46
5.4.1	Preparation of the Beryllium Trap - BeT	46
5.4.2	Avoided Crossing Measurement	48
5.4.3	Energy Transfer Measurement	52
6	Outlook	55
	References	58
7	Acknowledgements	64

Appendices	66
A Effective Resonator Parameters	67
A.1 Effective Capacitance C_{eff}	67
A.2 Effective Resistance R_{eff}	67
B Derivation of the Rabi Frequency with and without Detuning	69
B.1 No Detuning - Ideal Coupling	69
B.2 With Detuning - Real Coupling	69
C Avoided Crossing Fitting Routines	71
C.1 Effective Electrode Distance D_{eff}	71
C.2 Resonator Parameters	72
C.3 Ion Frequencies and Jitter	73
C.4 C_{eff} Fitting Routines	73
D Time-Independent Modes of the Coupled Ion System	76

1 Introduction

The Standard Model (SM) describes three of the four known fundamental interactions: electromagnetic, weak and strong. Though the SM has provided predictions of observables with great success, we know that the SM is not universal. It does not include aspects such as gravity or viable dark matter particles and leaves open questions such as the observed matter/anti-matter asymmetry with the current sources of combined charge- and parity violation or the accelerated expansion of the universe. New physics beyond the SM can be tested via direct observation of new particles and processes in large high-energy facilities or by precise measurements of quantities that are predictable by the SM, where discrepancies between theory and measurement pave the way to new physics [1]. One advantage of the latter precision experiments is their comparably small apparatus scale. According to [2], "the highest accuracy in measurements of any quantity in any field of science is obtained when the measurand can be converted into frequency". A versatile tool to correlate fundamental properties of ions to a frequency is the Penning trap. It stands out against other ion traps in ultra-high precision measurements testing fundamental physics of the SM, as it provides storage for single ions in an arbitrary charge state within a well-defined environment for theoretically an infinite amount of time.

Quantum electrodynamics (QED) was the first developed field theory of the SM and is the best tested one. It describes the interaction of light and matter and was stringently tested in free and bound electron g -factor measurements [3,4] in low and moderate field strengths. The g -factor relates the magnetic moment of a fundamental particle with its angular momentum. To verify theoretical predictions in the strong-field regime highly charged ions (HCIs) provide favorable conditions. There, the electron is naturally exposed to the one of the strongest accessible Coulomb fields¹, e.g. $\sim 10^{18} \text{ V m}^{-1}$ in hydrogenlike lead. The ALPHATRAP experiment [5] at the Max Planck Institute for Nuclear Physics is dedicated to bound electron g -factor measurements of such heavy HCIs with unrivaled precision in a cryogenic double Penning-trap setup. Recently, we presented the g -factor measurement of $^{40}\text{Ar}^{13+}$ as one of the most stringent tests of many-electron QED in strong fields [6] and successfully demonstrated extremely precise spectroscopy of highly suppressed transitions in the fine structure of $^{40}\text{Ar}^{13+}$ without fluorescence detection [7].

One solution for further improved measurement accuracy in Penning traps is a lowering of the amplitudes of the ion motion [8] – we speak of 'cooling' the ion. In general, ion cooling improves the systematic uncertainties in frequency measurements related to amplitude-dependent shifts by effectively decreasing the impact of trapping field inhomogeneities over the decreased ion motion. Cooling also reduces the Doppler broadening of linewidths, which is crucial for spectroscopy. While the first-order Doppler shift can in principle be eliminated by other techniques as well, the second-order Doppler shift requires such cooling [9]. Furthermore, cold ion clouds/plasmas undergo Coulomb crystallization forming highly structured and stable ion formations,

¹Even stronger fields can be found in muonic atoms or during the collision process of heavy ions.

which introduce a new field of research with a variety of applications [10]. So far, with resistive cooling the ions can be thermalized with the cryogenic detection system at approximately ~ 4 K. This can be lowered with a negative feedback loop [11] to reach an equivalent of ~ 1 K. With the technique of adiabatic cooling [12] the ion's amplitude can be reduced even further. E.g. a numerical calculation in [13] yielded a temperature of ~ 10 mK for a cloud of antiprotons. In [7] the application of negative feedback and adiabatic cooling were combined to reduce the temperature of the resistively cooled $^{40}\text{Ar}^{13+}$ ion by a factor of ~ 20 . Yet, it is still possible to go one step further. Probably the most commonly used cooling technique in atomic physics is laser cooling. Atoms can be reliably laser cooled to their Doppler limit T_D or even to their ground state with sophisticated techniques. However, the electronic level scales of HCIs are rigorously changed, and they often lack suitable cooling transitions that are accessible for lasers. One way to circumvent this issue is to sympathetically cool the HCI via Coulomb interaction with laser-cooled ions.² Sympathetic laser cooling in the context of high-precision frequency measurements in Penning traps still proves to be difficult and is rather used in Paul traps. First, precision Penning traps do not provide easy laser access due to their closed setup. Furthermore, the laser drastically alters the trap potential over time and also co-trapping the HCI with beryllium ions systematically perturbs the HCI's motion. The latter issue is solved with the common endcap technique [14]. But this method lacks the flexibility to cool arbitrary ions as their cooling times can get too long for efficient application. We have worked out a novel technique to perform sympathetic laser cooling of the HCI that circumvents laser-induced potential shifts and the co-trapping while providing control of the coupling strength and theoretically improving the efficiency of the similar common endcap technique by orders of magnitudes. We propose to trap the HCI and the laser cooled $^9\text{Be}^+$ in two different traps, that can be spatially separated, and only interact via a common detection system in a controlled way without irradiating the measurement trap with the cooling laser.

²Typically $^9\text{Be}^+$ ions are used, because they exhibit such a suitable laser cooling transition.

2 The Penning trap

We measure the g -factor via the *Larmor frequency* ω_L and additionally make use of the *free-space cyclotron frequency* ω_c to account for the external magnetic field strength B_0 :

$$\omega_L = g \frac{q_e}{2m_e} B_0 \quad \text{and} \quad \omega_c = \frac{q}{m} B_0. \quad (1)$$

The Larmor frequency corresponds to the precession of the spin around the magnetic field axis. A photon with the Larmor frequency can flip the spin-state between the electron spin-up $|\uparrow\rangle$ and spin-down state $|\downarrow\rangle$. The free-space cyclotron frequency describes the circulation of an ion with charge-to-mass ratio q/m (subscripts of q_e/m_e denote the electron charge-to-mass ratio) perpendicular to the magnetic field direction. When we probe ω_L via the *continuous Stern-Gerlach effect* [15] and combine it with a measurement of ω_c , the g -factor relation becomes independent of the magnetic field and is determined by the ratio of the two frequencies:

$$g = 2 \frac{\omega_L}{\omega_c} \frac{m_e}{m} \frac{q}{q_e}. \quad (2)$$

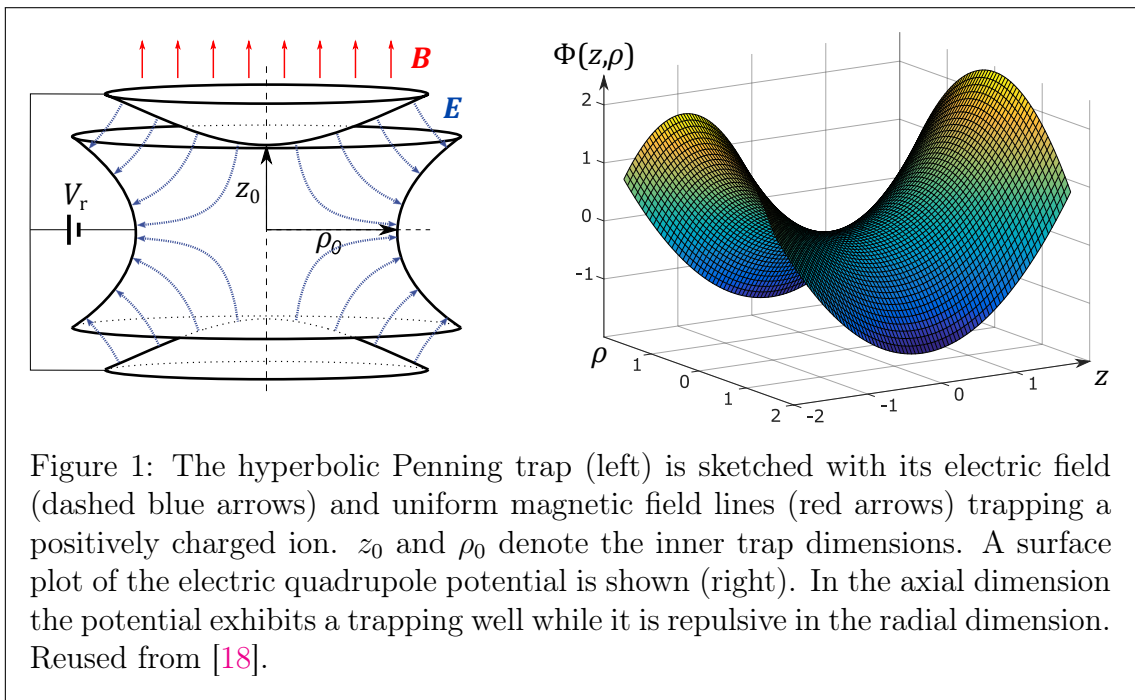
An elaborate frequency detection method forms the basis of our measurements. It allows us to measure ω_c to high precision and detect necessary spin-flips for probing ω_L . In this chapter I will outline a physical description of the Penning trap together with the detection system. The Penning trap physics has been explicitly reviewed in [16, 17].

2.1 Description of the Ideal Penning Trap

The Penning trap makes use of a strong homogeneous magnetic field $\mathbf{B}(z) = B_0 \mathbf{e}_z$ to force ions on a ω_c like trajectory and confine their motion radially in the corresponding (x, y) plane. However, with the slightest external disturbance the ion can still move in the z -axis along the magnetic field lines. To close this residual loophole an electrostatic field $\mathbf{E}(z, \rho) = -\nabla\Phi(z, \rho)$ is superimposed created by a potential Φ of quadrupolar form:

$$\Phi(z, \rho) = \frac{U_0 C_2}{2d_{\text{char}}^2} \left(z^2 - \frac{\rho^2}{2} \right). \quad (3)$$

A straight forward solution to produce such a field is to shape the electrodes according to the quadrupolar equipotential surfaces. The result is a hyperbolic Penning trap consisting of a circular ring electrode and two axisymmetric endcaps. Such a trap is depicted in figure 1 (left). U_0 is the potential of the ring electrode related to the two endcaps. Typically, the endcap potentials are grounded, and we can replace $U_0 \equiv U_r$ with the negative voltage applied to the ring electrode. Due to radial symmetry we can define the radius $\rho^2 = x^2 + y^2$ and the *characteristic trap length* $d_{\text{char}}^2 \equiv \frac{1}{2}(z_0^2 + \frac{\rho_0^2}{2})$, which serves as a trap dimension parameter. This makes C_2 a dimensionless but geometry dependent coefficient, which will be put into more context in section 2.3. The electrostatic trap potential is plotted (right). It acts



on positively charged ions radially repulsive towards the ring electrode but confines them axially.

2.2 The Confined Motion

The two superimposed trapping fields exert a force

$$\mathbf{F} = -q(\nabla\Phi - \dot{\mathbf{r}} \times \mathbf{B}) \quad (4)$$

on the ion at position $\mathbf{r} = (x, y, z)$ and confines it spatially in all three dimensions, if specific stability criteria are satisfied (see below). From this equation of motion (EOM) we can directly observe a purely electrostatic nature of the ion's axial motion because the magnetic cross product term vanishes in the z -component. From eq. (4) we deduce an axial oscillation with the *axial frequency*

$$\omega_z = \sqrt{\frac{qU_r C_2}{md_{\text{char}}^2}}. \quad (5)$$

The oscillation is stable as long as an electric potential with $qU_r C_2 > 0$ and $U_r > E_{\text{kin},z}/q$ is present for an ion with axial kinetic energy $E_{\text{kin},z}$. In the radial dimension the magnetic field couples the x - and y -motion and confines the ion in two independent radial modes. The first is a modification of (1) to what is called *modified cyclotron frequency* ω_+ as a result of the repulsive electrostatic field, which reduces the radial magnetic trapping potential and thus the original cyclotron frequency as well. Second, there is the *magnetron frequency* ω_- . It occurs because the electric outwards repulsion is deflected by the Lorentz force which gives rise to an

additional circular orbit of the ion's guiding center around the trap center.³ The frequencies of the two circulations are

$$\omega_{\pm} = \frac{1}{2} \left(\omega_c \pm \sqrt{\omega_c^2 - 2\omega_z^2} \right). \quad (6)$$

Radial stability is given under the strict condition

$$\omega_c > \sqrt{2}\omega_z \quad \text{which implies} \quad B_0 > \sqrt{\frac{2mU_0C_2}{qd_{\text{char}}^2}}. \quad (7)$$

This means that the magnetic field must be sufficiently strong to compensate for the electrostatic repulsion and prevent loss of the ion to the electrode surfaces. In conclusion, a trapped ion undergoes a complex motion of three independent

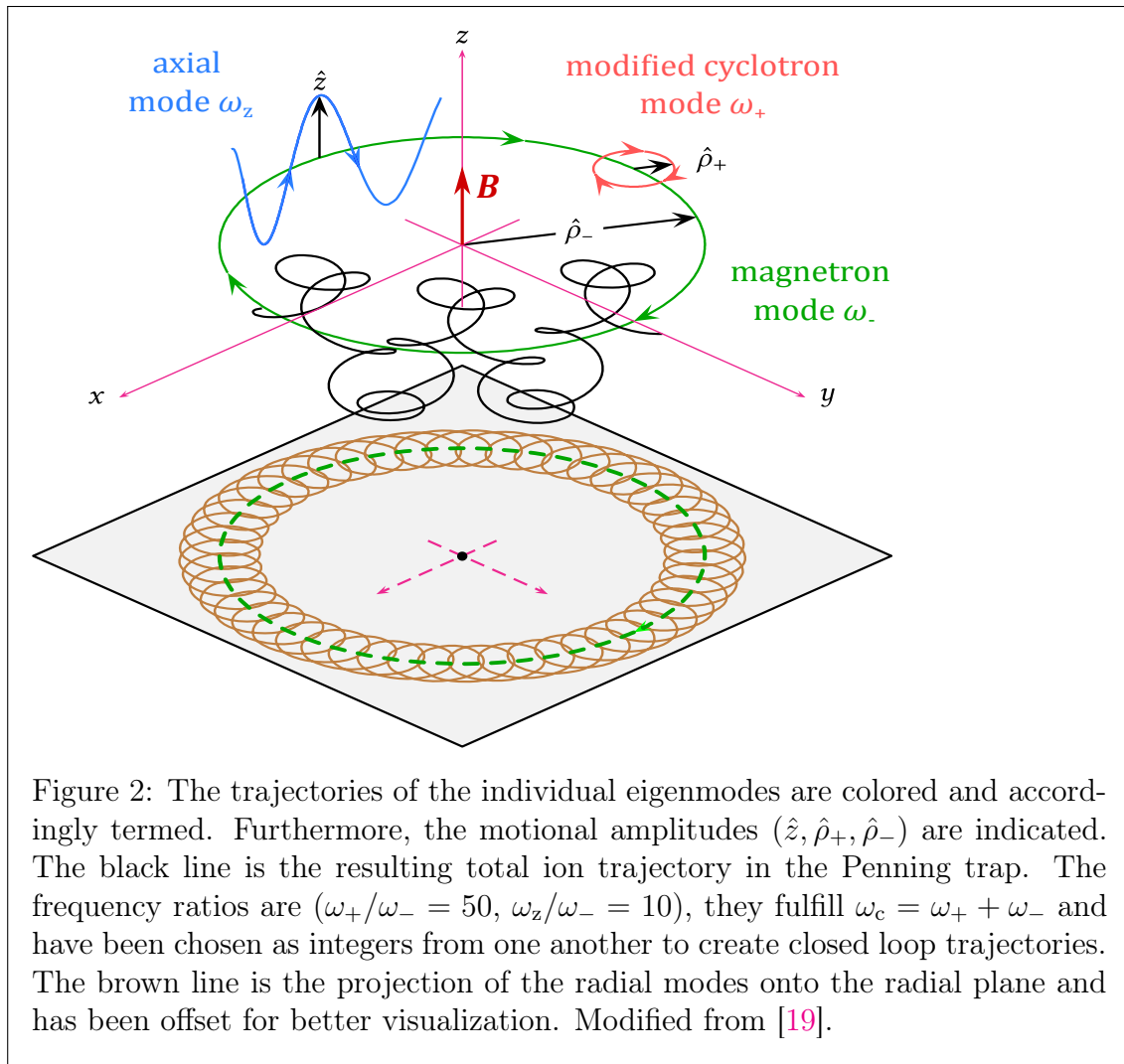


Figure 2: The trajectories of the individual eigenmodes are colored and accordingly termed. Furthermore, the motional amplitudes (\hat{z} , $\hat{\rho}_+$, $\hat{\rho}_-$) are indicated. The black line is the resulting total ion trajectory in the Penning trap. The frequency ratios are ($\omega_+/\omega_- = 50$, $\omega_z/\omega_- = 10$), they fulfill $\omega_c = \omega_+ + \omega_-$ and have been chosen as integers from one another to create closed loop trajectories. The brown line is the projection of the radial modes onto the radial plane and has been offset for better visualization. Modified from [19].

³This additional ' $\mathbf{E} \times \mathbf{B}$ drift' of the guiding center has the same direction of rotation as the modified cyclotron motion. The modified cyclotron motion orbits around the guiding center.

harmonic oscillations. The trajectories and the amplitudes⁴ ($\hat{z}, \hat{\rho}_+, \hat{\rho}_-$) of these eigenmodes are depicted in figure 2. A Taylor expansion of eq. (6) yields to first order a mass independent magnetron mode⁵ and a typical hierarchy⁶ of the frequency magnitudes for our apparatus:

$$\omega_- \ll \omega_z \ll \omega_+ < \omega_c. \quad (8)$$

With elaborate detection techniques we can measure these frequencies with high precision (see section 2.4). However, we cannot directly measure the important free-space cyclotron frequency ω_c , instead we determine it via the *invariance theorem* [16]:

$$\omega_c^2 = \omega_z^2 + \omega_+^2 + \omega_-^2. \quad (9)$$

Because ω_+ contributes the most, we have to measure it with the highest relative precision out of the three modes. In section 2.3 and in subsection 2.4.2 I describe the detection of ω_z and of ω_{\pm} , respectively. The invariance theorem holds even for some specific trapping field imperfections: a misalignment or tilt of the magnetic field lines with respect to the electrostatic field and elliptical deformations of the electrostatic equipotential lines.

The total time averaged energy of the trapped ion is the sum of potential and kinetic energy of the three independent modes (see [20]):

$$\bar{E}_{\text{tot}} = \frac{m}{2} [\omega_z^2 \hat{z}^2 + \omega_+(\omega_+ - \omega_-) \hat{\rho}_+^2 - \omega_-(\omega_+ - \omega_-) \hat{\rho}_-^2] \quad (10a)$$

$$\stackrel{(8)}{\approx} \frac{m}{2} \left[\omega_z^2 \hat{z}^2 + \omega_+^2 \hat{\rho}_+^2 - \frac{1}{2} \omega_z^2 \hat{\rho}_-^2 \right]. \quad (10b)$$

The magnetron mode contributes with a negative sign. The reason is, that it stores predominantly potential energy but on the other hand the electrostatic potential is repulsive. Thus an increase of ρ_- corresponds to an energy decrease and the magnetron motion is unbound. It is effectively metastable because radiative decay is negligible [16]. Over time the magnetron mode would decay, therefore spatially enlarge until the ion is lost to the electrodes surface. In contrast, the modified cyclotron mode mainly stores kinetic energy.

2.3 The Real Penning Trap

Ideally, the confined ion motion in the Penning trap consists of three independent harmonic oscillatory modes. But field imperfections in a Penning trap bring along a slight coupling and distortion of the three modes. The challenge in the field of high-precision Penning traps has always been to minimize those unavoidable field imperfections while ensuring reliable experimental trap operation. We can distinguish between electric and magnetic field imperfections. I will discuss the electric

⁴I term the axial amplitude as well as the radius of the radii modes likewise 'amplitude'.

⁵In this first order it equals the drift frequency $\omega_- = \frac{|\mathbf{E} \times \mathbf{B}|}{B^2 \hat{\rho}_-}$ of the ' \mathbf{E} cross \mathbf{B} drift'.

⁶Our precision trap has $d_{\text{char}} \approx 9.2$ mm and the magnetic field is $B_0 \approx 4$ T. For HCI's the frequencies are then in the order of $\omega_+ \sim 25$ MHz, $\omega_z \sim 650$ kHz and $\omega_- \sim 10$ kHz.

ones in the following.

First of all, to ensure an ideal electric potential of the form (3) the hyperbolic electrodes would need to extend over infinite length. This on its own contradicts experimental feasibility. Furthermore, the electrodes special shape cannot be manufactured and the electrode stack not aligned with infinite precision. It is thus obvious that the real electrostatic potential exhibits imperfections [21]. A cylindrical⁷ multipole expansion of the real potential Φ_{real} at the trap center simplifies to

$$\Phi_{\text{real}}(r, \theta) = \frac{U_0}{2} \sum_{\substack{k \neq 0 \\ k \text{ even}}}^{\infty} C_k \left(\frac{r}{d_{\text{char}}} \right)^k P_k(\cos \theta) \quad (11)$$

because the rotational terms vanish. It is $r = \sqrt{\rho^2 + z^2}$, $\cos \theta = \frac{z}{r}$ and P_k are the Legendre polynomials. Due to axial symmetry under $z \rightarrow -z$ odd terms vanish. Additionally, the zeroth-order term can be ignored, because a uniform potential offset does not generate a force on the particle. Note that the quadrupolar term $k = 2$ is equivalent to eq. (3) and represents the ideal electrostatic potential. This means, all higher order terms denote imperfections of the real trapping potential. The coefficients C_k describe their extent.

With present field imperfections the ion modes become anharmonic and their frequencies energy/amplitude dependent. The first-order frequency shifts by higher order terms have been calculated in [23] for all even orders. As an example the shifts for a non-zero C_4 are listed:

$$\frac{\Delta\omega_z}{\omega_z} = \frac{C_4}{C_2} \frac{3}{4d_{\text{char}}^2} (\hat{z}^2 - 2\hat{\rho}_+^2 - 2\hat{\rho}_-^2), \quad (12a)$$

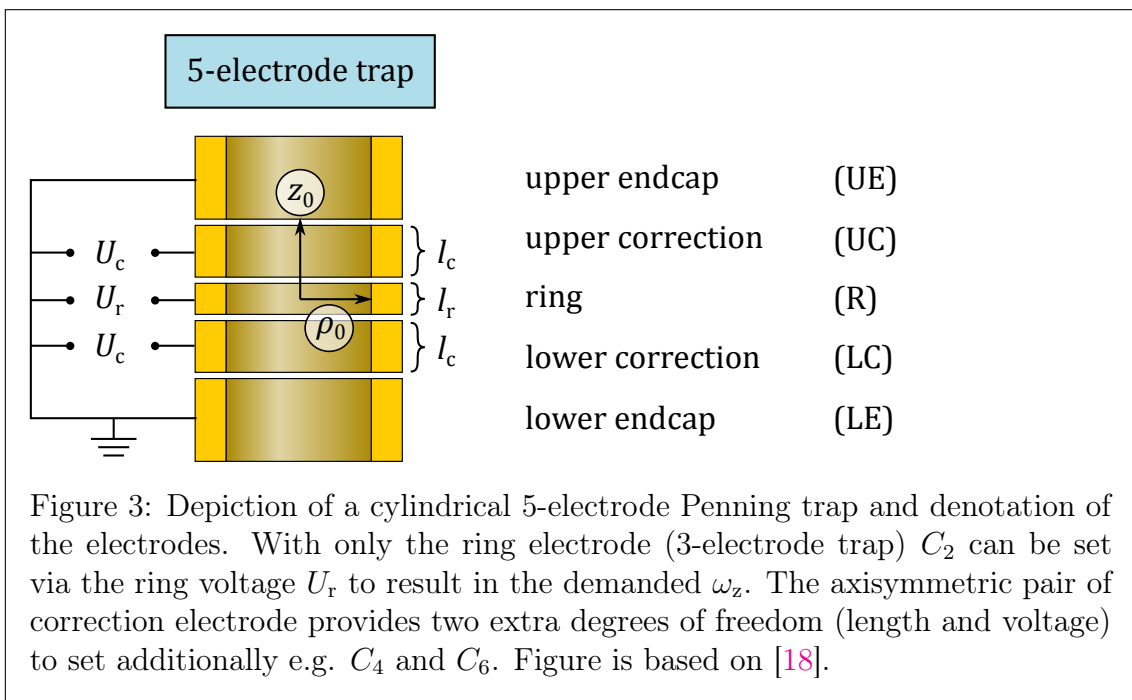
$$\frac{\Delta\omega_+}{\omega_+} = \frac{-C_4}{C_2} \frac{3}{2d_{\text{char}}^2} \frac{\omega_-}{\omega_+ - \omega_-} (2\hat{z}^2 - \hat{\rho}_+^2 - 2\hat{\rho}_-^2), \quad (12b)$$

$$\frac{\Delta\omega_-}{\omega_-} = \frac{C_4}{C_2} \frac{3}{2d_{\text{char}}^2} \frac{\omega_+}{\omega_+ - \omega_-} (2\hat{z}^2 - 2\hat{\rho}_+^2 - \hat{\rho}_-^2). \quad (12c)$$

The series order terms in (11) correspond with $\left(\frac{r}{d_{\text{char}}}\right)^k$. The shift caused by C_4 is therefore usually the most dominant one near the trap center. For ions at higher temperatures and larger amplitudes, higher order coefficients become more and more relevant. For high frequency precision, it is important to optimize the trap and keep the ion at small amplitudes, e.g. by cooling it.

In 1989 Tan and Gabrielse [24] came up with a cylindrical trap design which is easier to produce, because hyperbolic Penning traps were difficult to manufacture back then. ALPHATRAP utilizes such a trap as it provides more convenient access in the axial direction, e.g. for ion loading or electromagnetic radiation. Figure 3 depicts a cylindrical 5-electrode trap. It features a pair of correction electrode (UC, LC) next to the ring and endcap electrodes. Those electrodes provide more parameters to tune out trap anharmonicities and have also been used in hyperbolic Penning

⁷We can treat the deviations as cylindrical symmetric when we average over the radial motions of the ion [20, 22].



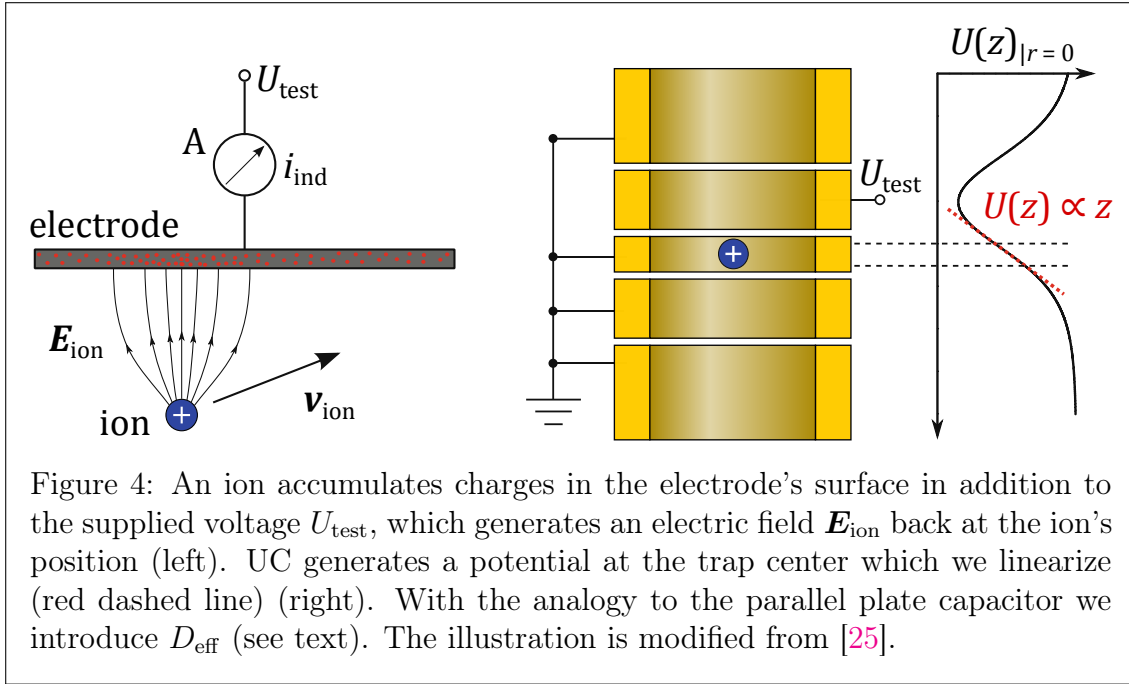
traps [21]. In general, for a 5-electrode trap the coefficients decompose into

$$C_k = C_{k,r} + D_k \cdot TR \quad \text{with} \quad TR = \frac{U_c}{U_r}, \quad (13)$$

where $C_{k,r}$ are the imperfections produced by the ring electrode and $D_k \cdot TR$ describes the influence of the correction electrodes in the trap center. While U_r sets ω_z , the length (l_r, l_c) and supplied voltage (U_c) of ring and correction electrode pair are three degrees of freedom for further optimization purposes.⁸ We typically choose to meet the following useful operation conditions. The trap is *compensated*, meaning the dominant coefficients $C_4 = C_6 = 0$ vanish for the right choice of the *tuning ratio* (TR). A proper design of electrode dimensions yields *orthogonality* ($D_2 = 0$), meaning that ω_z is independent of the TR. More correction electrode pairs allow compensating even more higher order terms at a cost of a more complex trap design and optimization process (see [25]).

For magnetic imperfections I refer to [20] for an in-depth formalism. Nevertheless, let me comment on them. It is common to use superconducting magnets for generating strong magnetic fields. With configurations of built-in shimming coils they can be tuned to good field homogeneity. Still, there exist residual inhomogeneities and additionally the strong magnetic field locally magnetizes materials depending on their susceptibility. Similar to the electric imperfections the axial magnetic field can be decomposed into a series expansion, whose contributions apart from B_0 also lead to frequency shifts and weak mode coupling.

⁸In principle the pair of correction electrode provide four individual parameters (l_c, U_c) for the upper and lower electrode. But as a result of this, the trap would not be axisymmetric and odd coefficients such as C_3 and C_5 would arise.



2.4 Frequency Detection of the Ion

ALPHATRAP utilizes a non-destructive ion detection method, referred to as *bolometric* detection [26]. The oscillating ion induces image charges in the electrodes corresponding to a fA image current. With an impedance we can translate the current via Ohm's law into an AC voltage signal and then extract the ion's frequency information from the voltage signal with a fast Fourier transformation (FFT) analysis. However, the experimental realization of the detection and read out of the ion frequencies from such tiny image currents is a sophisticated task. This chapter provides the essential fundamentals for the main work of my thesis given in section 5.

2.4.1 Image Current Detection with a Tank Circuit

The description of an induced current in conductors by a charge q moving with velocity v was made by [27] and [28] back in 1939:

$$i_{\text{ind}} = q\mathbf{v} \frac{\mathbf{E}_{\text{ion}}(\mathbf{r}(t))}{U_{\text{el}}}. \quad (14)$$

In Penning traps typically one or more electrodes act as the *pick-up electrode* for the image currents. $\mathbf{E}_{\text{ion}}(\mathbf{r}(t))$ denotes then the electric field at the ion position $\mathbf{r}(t)$ produced by the pick-up electrode, when a $U_{\text{test}} = 1\text{ V}$ test-voltage is applied to it while all other electrodes are grounded. This situation is depicted in figure 4. The induced charges in a conductor and the field lines of \mathbf{E}_{ion} are depicted on the left. On the right we apply this to a Penning trap with grounded electrodes except the pick-up electrode and plot the resulting total axial potential $U(z)$. For small axial ion amplitudes we can linearly approximate $U(z)$ (red dashed line) and thus obtain

a constant electric field in the vicinity of the ion ($\mathbf{E}_{\text{ion}} = -\partial_z U(z)|_{z_{\text{ion}}} = \text{const}$). This is equivalent to the electric field of a parallel plate capacitor and allows us to introduce the *effective electrode distance* D_{eff} with

$$D_{\text{eff}} = \frac{U_{\text{test}}}{E_{\text{ion}}}. \quad (15)$$

It represents an axial distance from the ion center to the pick-up electrode analogously to the distance between the plates of a parallel plate capacitor. We can in principle calculate E_{ion} numerically from an electrostatic field simulation⁹ and thus estimate D_{eff} as a value for orientation. The new parameter allows us to rewrite (14):

$$i_{\text{ind}}(t) = \frac{q\dot{z}}{D_{\text{eff}}} \stackrel{10}{=} -\frac{q\omega_z \hat{z}}{D_{\text{eff}}} \sin(\omega_z t + \phi_z) \quad \Leftrightarrow \quad i_{\text{ind}}^{\text{rms}} = \frac{q\omega_z \hat{z}^{\text{rms}}}{\sqrt{2}D_{\text{eff}}}. \quad (16)$$

In the right equation the quadratic mean transforms the alternating current to an effective direct current.¹¹ While the induced currents in other electrodes flow freely into their voltage sources, the pick-up electrode is connected to a tank/resonator-circuit with a large impedance $Z(\omega)$ at the ions axial frequency ω_z . The induced current causes a voltage drop across the resonator's impedance according to

$$u_{\text{sig}}(t) = (Z(\omega)i_{\text{ind}}(t))|_{\omega=\omega_z}. \quad (17)$$

We require $Z \sim 100 \text{ M}\Omega$ to obtain a voltage drop of $\sim 10 \text{ nV}$ from a fA current. Figure 5 (top left, red area) depicts the resonator circuit connected to the trap. In a nutshell the resonator (blue block of impedance Z) is an inductance L connected to the trap. The trap itself, the coil winding, the amplifier, wiring, etc. exhibit parallel stray capacitances which we combine to one parallel trap capacitance C_p . This forms a parallel LC-circuit in the first place (see bottom left, green area). However, the losses of L and C_p can be modeled by the equivalent series resistance R_L and R_C , respectively, which we can further combine to a parallel resistance R_p [29]. Ultimately, we end up with a parallel RLC-circuit, whose L shunts C_p and has the impedance

$$Z_{\text{res}}(\omega) = Z_R \parallel Z_C \parallel Z_L = \left(\frac{1}{R_p} + i\omega C_p + \frac{1}{i\omega L} \right)^{-1}. \quad (18)$$

⁹However, it simulates only an ideal configuration. It lacks the real deviations e.g. electrode manufacturing.

¹⁰We can describe the axial oscillation via $z = \hat{z} \cos(\omega_z t + \phi_z)$ with an arbitrary initial oscillation phase ϕ_z [20].

¹¹Let me give an idea of the tiny image current produced for realistic Penning-trap parameters: with $D_{\text{eff}} = 3 \text{ mm}$, $\omega_z = 2\pi \times 650 \text{ kHz}$ and $\hat{z} = 10 \mu\text{m}$ the induced current is in the order of $i_{\text{ind}}^{\text{rms}} \approx 0.3 \text{ fA}$. Looking at the parameters, we can increase it to some degree by choosing a higher ion charge state. D_{eff} is a trap constant, and we can only decrease it with an alternative trap design e.g. smaller electrode radii. The amplitude of the thermalized ion is fixed by the environment temperature.

At the resonance frequency $\omega_r = \frac{1}{\sqrt{LC}}$ (or *resonator center frequency*) the absolute value of $Z_{\text{res}}(\omega)$ and thus u_{sig} becomes maximal. In figure 5 (right, blue area) I plotted the real and complex part of $Z_{\text{res}}(\omega)$ based on our resonator parameters determined in [18] (see caption). In fact the impedance at the resonator center becomes purely real, because the capacitive and inductive reactance cancel each other. This allows us to quantify R_p via

$$Z_{\text{res}}(\omega_r) \equiv R_p = Q \sqrt{\frac{L}{C_p}} = Q \omega_r L = \frac{Q}{\omega_r C_p}. \quad (19)$$

The *quality factor* $Q = \omega_r / \Delta\omega$ describes the selectivity of the resonator within the FWHM resonance bandwidth $\Delta\omega$. Eq. (19) sets the requirements for a sufficiently large voltage drop u_{sig} : a high Q -value and inductance. The resonator must be carefully designed in consideration of C_p to roughly achieve $\omega_r \approx \omega_z$. Afterwards, we can tune ω_z via (5) to some degree with the ring voltage. The resonators implemented at ALPHATRAP were designed and build by A. Weigel [18].

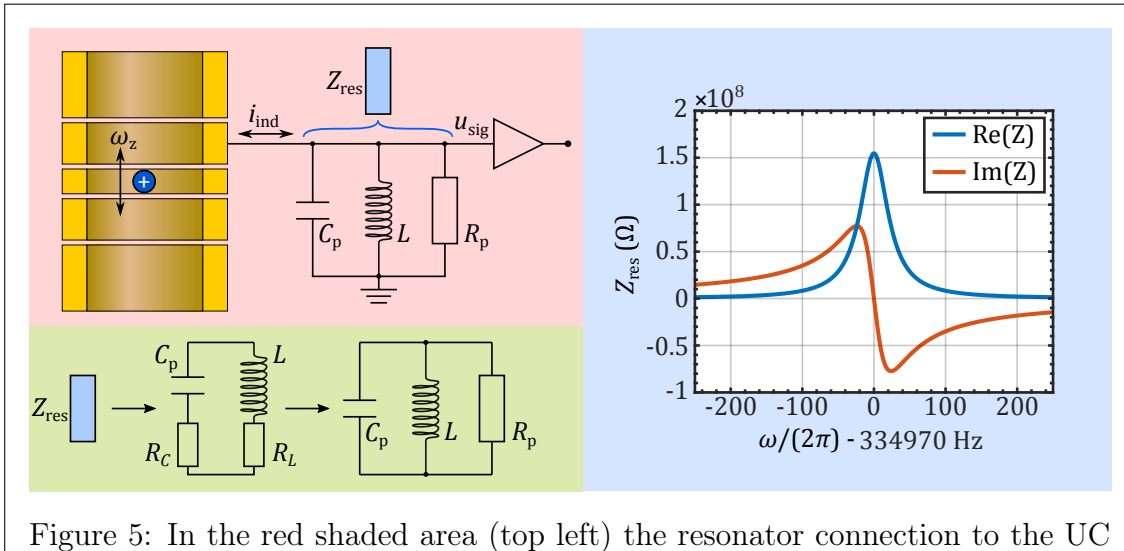


Figure 5: In the red shaded area (top left) the resonator connection to the UC electrode is shown in a simplified depiction. Actually, the amplifier is connected to a tap on the inductance. The ion oscillates with ω_z and induces a current i_{ind} . The green shaded area (bottom left) illustrates how the parallel RLC-circuit (blue Z component) originates from the inductance and the trap capacitances. The blue shaded area (right) covers the plot of the real and complex part of resonator impedance Z_{res} . The x-axis spans over ± 250 Hz detuned from the resonator center. I used ($Q \approx 7000$, $C_p \approx 21.5$ pF and $L \approx 10.5$ mH). At resonance, it is $R_p \approx 155$ M Ω . Note the sign of the complex impedance. On the resonator's left flank the inductive reactance dominates, on the right flank the capacitive reactance dominates. At the center they cancel exactly. See text for details. Modified from [18] and [30].

2.4.2 The Resonator Line Shape Model

In this subsection I consider the resonator without the ion. The only available signal is then the thermal *Johnson-Nyquist noise* [31, 32] in a given bandwidth $\Delta\nu$. This noise is caused by random thermal motion of charge carriers within the resonator bulk and is always present. We can model it by a voltage source in series to the trap resistance R_p that provides a thermal rms-voltage noise spectrum

$$u_n = \sqrt{4k_B T \Delta\nu \operatorname{Re}(Z)}, \quad (20)$$

where k_B is the Boltzmann constant. We retain our resonators at cryogenic temperatures ($T \approx 4$ K) to minimize the thermal noise. Since in this case the impedance in eq. (20) is given by the resonator ($Z \rightarrow Z_{\text{res}}$), the noise spectrum will follow the line shape of $\operatorname{Re}(Z_{\text{res}})$ as plotted in figure 5 with $u_n \propto \sqrt{\operatorname{Re}(Z_{\text{res}})}$. In order to detect the noise spectrum it is first amplified in a cryogenic low-noise amplification stage, Fourier analyzed via a FFT and at last amplified once more at room temperature. The final detected noise spectrum is [25, 33]

$$u_d(\omega) = A_{\text{amp}}(1 + \kappa_{\text{det}}(\omega - \omega_r))\sqrt{u_n^2(\omega) + u_{\text{en}}^2(\omega)} \quad (21a)$$

$$\approx 10 \log_{10} \left[\tilde{A} \operatorname{Re} \left(\frac{Z(\omega)}{R_p} \right) + \tilde{u}_{\text{en}}^2(\omega) \right] + \tilde{\kappa}_{\text{det}}(\omega - \omega_r). \quad (21b)$$

The upper equation line denotes the detected signal in units of rms-voltage [V^{rms}] while it is converted to a decibel scale [dBV^{rms}] in the lower line by the relation $1 \text{ dBV}^{\text{rms}} = 20 \log_{10}(1 \text{ V}^{\text{rms}})$. The parameters u_{en} and κ_{det} include effects of the detection system: the first represents the additional electronic noise of the amplification stages with total amplification A_{amp} , and the second accounts for any potential first order frequency dependency. It is further $\tilde{A} \equiv A_{\text{amp}}^2 \cdot 4k_B T \Delta\nu R_p$ and $\tilde{u}_{\text{en}} \equiv A_{\text{amp}} u_{\text{en}}$ and $\tilde{\kappa}_{\text{det}} \equiv \frac{20}{\log 10} \ln(\kappa_{\text{det}})$. Note the approximation $\ln(1+x) \approx x$ in the second line because we only assume a marginal slope.

This equation is our fit model for all experimentally acquired resonator noise spectra. It is universal in the sense that Z models all the physics involved in the ion detection and determines the observed Fourier transformed line shape, be it trapping non to multiple ions or interactions between ions. In this specific case I considered no trapped ion, meaning $Z \rightarrow Z_{\text{res}}$. A trapped ion alters the impedance Z additionally as I will show in the next section.

2.4.3 The Line Shape Model Including the Ion

Now I consider the resonator together with a trapped ion. The voltage drop u_{sig} in eq. (17) exerts a retroactive electric force $F_{\text{el},z}$ back on the ion. Within the picture of the parallel plate capacitor approximation, we can write:

$$F_{\text{el},z} = -q\partial_z U_{\text{el},z} = -qE_z = -q \frac{u_{\text{sig}}}{D_{\text{eff}}} \stackrel{(17)}{=} -\frac{qZ_{\text{res}}(\omega_z)i_{\text{ind}}}{D_{\text{eff}}} \stackrel{(16)}{=} -\frac{q^2 Z_{\text{res}}(\omega_z)}{D_{\text{eff}}^2} \dot{z}. \quad (22)$$

The additional force changes the original axial EOM from (4) to

$$\ddot{z} = - \underbrace{\frac{qU_0C_2}{md_{\text{char}}^2}}_{\omega_z^2} z - \underbrace{\frac{q^2 Z_{\text{res}}(\omega_z)}{mD_{\text{eff}}^2}}_{2\gamma} \dot{z}, \quad (23)$$

which is solved with the ansatz $z \propto \exp(i\omega t - \gamma t)$. The axial motion has the form

$$z(t) \propto e^{-\gamma t} e^{\pm i\sqrt{\omega_z^2 - \gamma^2} t}. \quad (24)$$

This describes a damped oscillation. Note that γ is complex. The timescale τ_{res} of the damping depends on the real part of γ and is inversely proportional to $\text{Re}(Z_{\text{res}})$:

$$\tau_{\text{res}}(\omega_z) = \frac{1}{2 \text{Re}(\gamma)} = \frac{mD_{\text{eff}}^2}{q^2 \text{Re}(Z_{\text{res}}(\omega_z))}. \quad (25)$$

In a physical picture the damping corresponds to power dissipation of the induced currents in the resistive part¹² of the resonator.¹³ We call this behavior *resistive cooling*, which was first implemented in [34]. By inserting eq. (24) into the time averaged energy (10b) and taking the derivative we see that the ion's axial motion is cooled exponentially:

$$\dot{\bar{E}}_{\text{tot}} = -2 \text{Re}(\gamma) m \omega_z^2 \bar{z}^2 = -\frac{1}{\tau_{\text{res}}} \bar{E}_{\text{tot}} \quad \longrightarrow \quad \bar{E}_{\text{tot}} = E_0 e^{-\frac{t}{\tau_{\text{res}}}}. \quad (26)$$

On the other hand, we can pull the complex part γ into the oscillation term and deduce a shifted oscillation frequency $\tilde{\omega}_z$ with

$$\tilde{\omega}_z = \underbrace{\sqrt{\omega_z^2 - \gamma^2}}_{\approx \omega_z} - \text{Im}(\gamma) \approx \omega_z - \text{Im}(\gamma). \quad (27)$$

We hereby neglect the small effect of γ in the square root (shift of 10^{-4} Hz) in the middle part of the equation. The direction of the shift $\omega_z \rightarrow \tilde{\omega}_z$ depends on the resonator flank on which the ion is positioned, because the sign of $\text{Im}(Z_{\text{res}})$ changes, but the ion's axial frequency is always pushed away from the resonator center. We call this effect *frequency pushing*. The pushing near the resonator center is very small but becomes larger (\sim Hz) when moving off the center region. In [29] and [35] they compute the frequency pushing explicitly.

In the picture of the equivalent circuit we can model the trapped and thermalized ion interacting with the resonator as a series LC-circuit. The equivalent circuit of the overall system is shown in the green area of figure 6 (top). The ion has the

¹²The reactance shifts the current's phase and stores energy, but it does not dissipate any.

¹³The heating effect on the resonator bulk is negligible because of the extremely tiny currents. Therefore, we can treat the resonator as a thermal bath in contact with the ion.

components [36]

$$L_{\text{ion}} = \frac{mD_{\text{eff}}^2}{q^2} \quad \text{and} \quad C_{\text{ion}} = \frac{q^2}{\omega_z^2 m D_{\text{eff}}^2}. \quad (28)$$

Note that L_{ion} is frequency independent. We can use it with eq. (25) to write $L_{\text{ion}} = \tau_{\text{res}}(\omega_z) \text{Re}(Z_{\text{res}}(\omega_z))$ and choose any arbitrary frequency to quantify it. If we set $\omega_z = \omega_r$ the ion's impedance can be written as¹⁴

$$Z_{\text{ion}} = i\omega L_{\text{ion}} + \frac{1}{i\omega C_{\text{ion}}} = i\omega R_p \tau_{\text{res}} \left(1 - \frac{\omega_r^2}{\omega^2} \right). \quad (29)$$

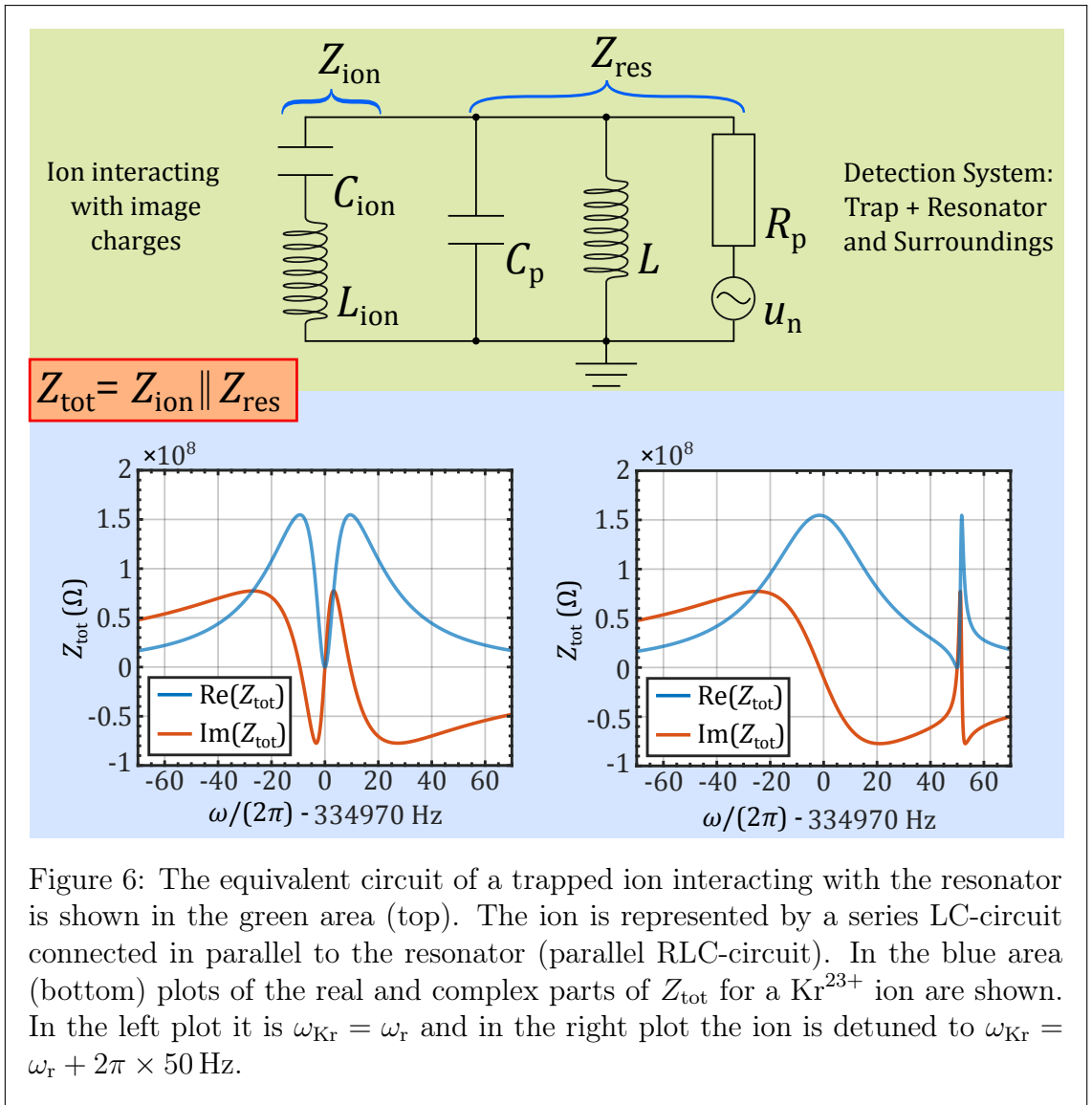


Figure 6: The equivalent circuit of a trapped ion interacting with the resonator is shown in the green area (top). The ion is represented by a series LC-circuit connected in parallel to the resonator (parallel RLC-circuit). In the blue area (bottom) plots of the real and complex parts of Z_{tot} for a Kr^{23+} ion are shown. In the left plot it is $\omega_{\text{Kr}} = \omega_r$ and in the right plot the ion is detuned to $\omega_{\text{Kr}} = \omega_r + 2\pi \times 50$ Hz.

¹⁴This is the frequency position where the impedance becomes maximal $\text{Re}(Z_{\text{res}}) = R_p$ and the damping constant minimal $\tau_{\text{res}} \equiv \tau_p$

Now the combined impedance Z_{tot} of resonator and ion determines the thermal noise spectrum via

$$Z_{\text{tot}} = Z_{\text{ion}} \parallel Z_{\text{res}} \quad (30)$$

and replaces $Z \rightarrow Z_{\text{tot}}$ in the line shape fit model (21b). A closer look on the line shape of Z_{tot} is instructive to predict the detected voltage spectrum better. In figure 6 (bottom) I compare two different cases of Z_{tot} : a Kr^{23+} ion sits on the resonator center in the left plot and it is detuned to the right resonator flank in the right plot. Both plots show a leveling of $\text{Re}(Z_{\text{tot}})$ at the ion's frequency ω_z . In the equivalent circuit picture it becomes clear why: with eq. (28) we can write the resonance frequency of the ion's LC-circuit as $\omega_{r,\text{LC}} = \frac{1}{\sqrt{L_{\text{ion}}C_{\text{ion}}}} = \omega_z$. Furthermore, a series LC-circuit exhibits an anti-resonance behavior $Z_{\text{ion}}(\omega_{r,\text{LC}}) = 0$. This means the full equivalent circuit is always shortened at ω_z because the series LC-circuit becomes completely transparent.¹⁵ We call this the *ion dip*. In a more vivid picture the signal voltage produced by the ion adds to the resonator noise but due to the retroactive force with opposite phase [17]. Those two voltages exactly cancel, if the ion has thermalized with the resonator bulk because then the induced power density by the ion is equal to the noise power density. An excited or hot ion has larger oscillation amplitudes and induces excess power density that is visual as a peak signal on top of the resonator noise. It would be therefore modeled by a current source parallel to the resonator [37].

The single ion dip has a Lorentzian shape – as a consequence of the FFT of the exponential resistive damping – with a FWHM of

$$\delta\omega = \frac{1}{\tau_{\text{res}}}. \quad (31)$$

The dip width of multiple in-phase oscillating ions scales linearly with their number N . Counter-oscillations of two identical ions do not induce currents and are not detectable.

In the right plot the frequency pushing $\omega_z \rightarrow \tilde{\omega}_z$ plays an important role. The line shape of $\text{Re}(Z_{\text{tot}})$ shows an additional peak at $\tilde{\omega}_z$ next to the dip at ω_z . We call this a *dispersive signal*. While the dip is solely a property of the ion, the peak is a result of the interaction between ion and resonator. There, the complex part of the two constituents $\text{Im}(Z_{\text{ion}})$ and $\text{Im}(Z_{\text{res}})$ cancel exactly yielding $\text{Im}(Z_{\text{tot}}(\tilde{\omega}_z)) = 0$. This means again that $Z_{\text{tot}}(\tilde{\omega}_z) \equiv R_{p,\text{tot}} = R_p$ is purely real and the frequency pushed ion sees R_p . Because of this, the voltage signal height of the dispersive peak is equal to the resonator center height, if the ion is thermalized.

¹⁵The ion is modelled lossless (infinite Q -value). Otherwise, the circuit would be only partial transparent and $\text{Re}(Z_{\text{tot}})$ would not completely drop to zero or the dispersive signal not reach the resonator height level.

2.5 Ion Excitation and Sideband Coupling

In Penning traps it is common to excite a single ion mode or to couple the radial modes to the axial mode both via radio frequency (RF) drive fields. To this end, some of our electrodes are half or quarter segmented to allow various forms of RF excitations that enable among others the following important Penningtrap techniques.

2.5.1 Dipole Excitation

A dipolar drive field alters the electric field in one direction and allows individual excitation of the motional modes. Depending on the excitation- or drive strength U_D and the effective electrode distance $D_{\text{eff},D}$ to the corresponding drive electrode, the excitation field at the ion position is

$$\mathbf{E}_{D_i}(t) = \frac{U_{D_i}}{D_{\text{eff},D_i}} \sin(\omega_{\text{rf}}t + \phi_{\text{rf}}) \cdot \mathbf{e}_i. \quad (32)$$

It is $i = (x, y, z)$ the spatial coordinate and ω_{rf} the drive field frequency. This field adds to the EOM (4) and increases¹⁶ the amplitude of the corresponding excited mode at resonance $\omega_{\text{rf}} \approx \omega_i$. A correction or endcap electrode can act as the drive electrode for axial excitation, while the segments of a split electrode produce a drive field directed in the radial plane to excite the radial modes. Excitation of ions is an effective tool for a variety of applications, e.g. we used it to test the amplitude dependent frequency shifts and field imperfections in section 5.4.1.

2.5.2 Quadrupole Sideband Coupling

A quadrupolar drive field extends in two directions and couples two otherwise (almost) independent modes. The drive field at the ion position produced by a split correction electrode is

$$\mathbf{E}_{Q_{xz}} = \frac{U_{Q_{xz}}}{D_{\text{eff},Q_{xz}}^2} \sin(\omega_{\text{rf}}t + \phi_{\text{rf}}) \cdot (x\mathbf{e}_z + z\mathbf{e}_x), \quad (33)$$

or alternatively a Q_{yz} drive of analogous form. This excitation allows us to do sideband coupling of the axial and one radial mode with a drive frequency at one of the sidebands $\omega_{\text{rf}} = \omega_{\pm} \mp \omega_z$.¹⁷ During mode coupling the modes are amplitude

¹⁶Depending on the initial phase difference of ion oscillation and drive field the ion's amplitude might decrease at first.

¹⁷Only these sidebands produce stable coupling with $\langle n_z \rangle = \langle n_+ \rangle$. At the respective other sideband the drive field heats both modes exponentially [16].

modulated with Rabi oscillations of frequency Ω_R [38]:

$$z(t) = \overbrace{\hat{z}_0 \sin\left(\frac{\Omega_R}{2}t + \varphi_R\right)}^{\hat{z}(t)} \cos(\omega_z t + \phi_z), \quad (34a)$$

$$\rho_{\pm}(t) = \underbrace{\hat{\rho}_{\pm,0} \cos\left(\frac{\Omega_R}{2}t + \varphi_R\right)}_{\hat{\rho}_{\pm}(t)} \cos(\omega_{\pm} t + \phi_{\pm}). \quad (34b)$$

The phase φ_R is an arbitrary initial phase. The coupled modes exchange energy periodically with Ω_R such that their motional amplitude vary with time. Hereby denote \hat{z}_0 and $\hat{\rho}_{\pm,0}$ their maximum amplitude. In the FFT spectrum of the resonator the modulated axial motion exhibits two dips at the frequencies ω_1 and ω_r separated by the Rabi frequency Ω_R . These correspond to the new time-independent solutions of the coupled system.¹⁸ In a more general consideration with a small but arbitrary detuning δ of the drive frequency $\omega_{rf} = \omega_{\pm} \mp \omega_z + \delta$ the Rabi oscillations occur with the higher *generalized* Rabi frequency $\tilde{\Omega}_G = \sqrt{\delta^2 + \Omega_R^2}$ [39] and energy is exchanged only partially. The separated frequencies are $\omega_{r,1} = \omega_z - \frac{\delta}{2} \pm \frac{\Omega_R}{2}$.

The mode coupling allows us to e.g. calculate the radial frequencies¹⁹ in a *double dip measurement* via

$$\omega_{\pm} = \omega_{rf} \pm (\omega_1 + \omega_r - \omega_z). \quad (35)$$

We can also combine mode coupling with resistive cooling. This way the resonator effectively dissipates excess energy of the radial mode which is transferred to the axial mode. In equilibrium the time averaged energies are [16]

$$\langle E_{\pm} \rangle = \pm \frac{\omega_{\pm}}{\omega_z} \langle E_z \rangle. \quad (36)$$

¹⁸We can no longer speak of the axial mode being an eigenmode of the coupled system. The two dips represent orthogonal modes within the new basis and are a superposition of axial and radial mode.

¹⁹In principle we can detect the modified cyclotron mode with a dedicated cyclotron resonator. In practice however, this requires a different resonator dedicated to only a limited range of q/m due to the high variation of ω_+ within different ion species.

3 The Experimental Setup

ALPHATRAP aims to perform high-precision g -factor measurements of heavy HCI. Parts of the experiment are based on the LIONTRAP experiment in Mainz, Germany, where the masses of light HCIs are measured [40–42]. There, the ions are internally produced by an electron-beam ion source [43]. Heavy HCIs however require a dedicated production facility such as accelerator storage rings, like the ESR [44] at GSI in Darmstadt to which the HITRAP [45] is connected, or large electron-beam ion traps (EBIT) like the cryogenic Heidelberg EBIT (HD-EBIT) [46] from the group of J. R. Crespo at the MPIK. The HD-EBIT can potentially reach electron beam energies up to 150 keV. This is sufficient to create hydrogenlike $^{208}\text{Pb}^{81+}$. To utilize this unique possibility ALPHATRAP is connected to the HD-EBIT via a room-temperature electrostatic beamline. A smaller Heidelberg compact EBIT (HC-EBIT) [47] and a laser ion source (LIS) [48] for singly charged $^9\text{Be}^+$ production are linked to the beamline as well.

In the following sections I give a rundown of the ALPHATRAP apparatus and the cooling laser system. A more profound description can be found in prior PhD theses [7], [18] and [6]. Many of the technical details are covered in our review paper [5] e.g. the beamline, ion production and injection, which I will not cover further in this thesis.

3.1 Outer Trap Setup - Magnet and Cryostat

We reuse the warm bore Oxford 200/130 NMR superconducting magnet from SMILETRAP [49]. It is shown together with the enclosed cryostat and parts of the beamline in figure 7. The magnet is charged to 4 T which corresponds to $\omega_L \approx 2\pi \times 112$ GHz for hydrogenlike and $\omega_L \approx 2\pi \times 37$ GHz for boronlike ions. Its spatial homogeneity in the nominal trap center is shimmed to $\delta B/B < 3 \times 10^{-7}$ based on a 1.5 cm^3 NMR probe.

A cryostat is lowered into the magnet bore (see figure) and the contained trap chamber cooled to cryogenic temperatures. To this end, the cryostat consists of two copper stages to shield the inner trap tower from the room-temperature bore environment. The outer 77 K stage (blue) and the inner 4 K stage (violet) are (thermally) anchored to a 55 l liquid nitrogen (LN_2) and 14 l liquid helium (LHe) reservoir, respectively. The stages are built and anchored in a way to suppress thermal conductivity between them. In addition to that, the magnet bore is evacuated to a $<10^{-5}$ mbar vacuum (cryostat vacuum) to increase thermal isolation even further. The total heat load on the 4 K stage is <100 mW corresponding to about 4.7 days cryogenic operation [18] before the LHe reservoir runs empty and must be refilled. A long beamtube connects the trap chamber with the room-temperature beamline for ion injection. The trapping time of ions in the Penning trap depends severely on the vacuum quality. For the production of an ultra-high vacuum inside the trap chamber a special cryogenic valve [50] can be manually closed to isolate the trap vacuum from the 10^{-11} mbar beamline vacuum. Upon cooling down, rest gas inside

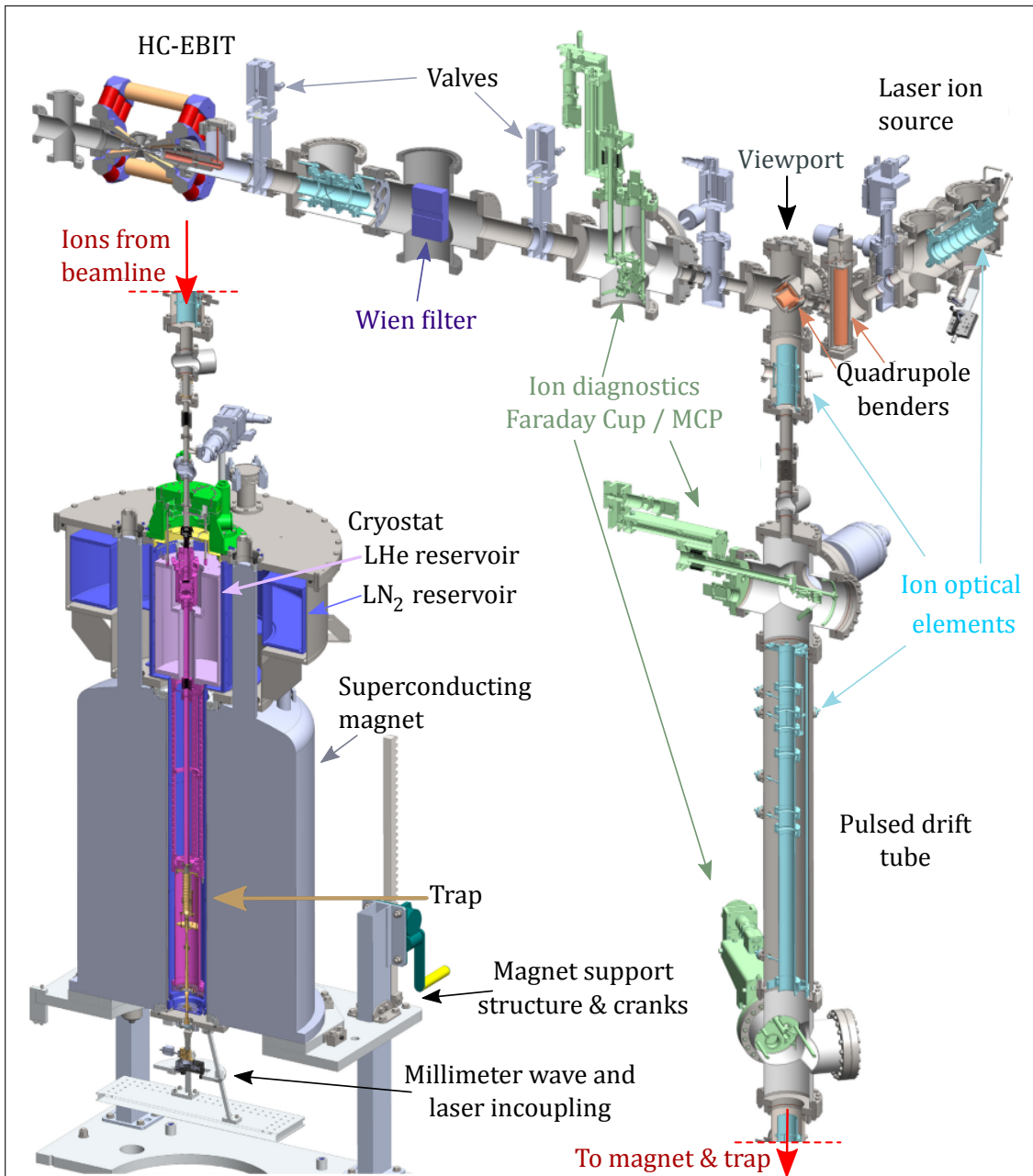
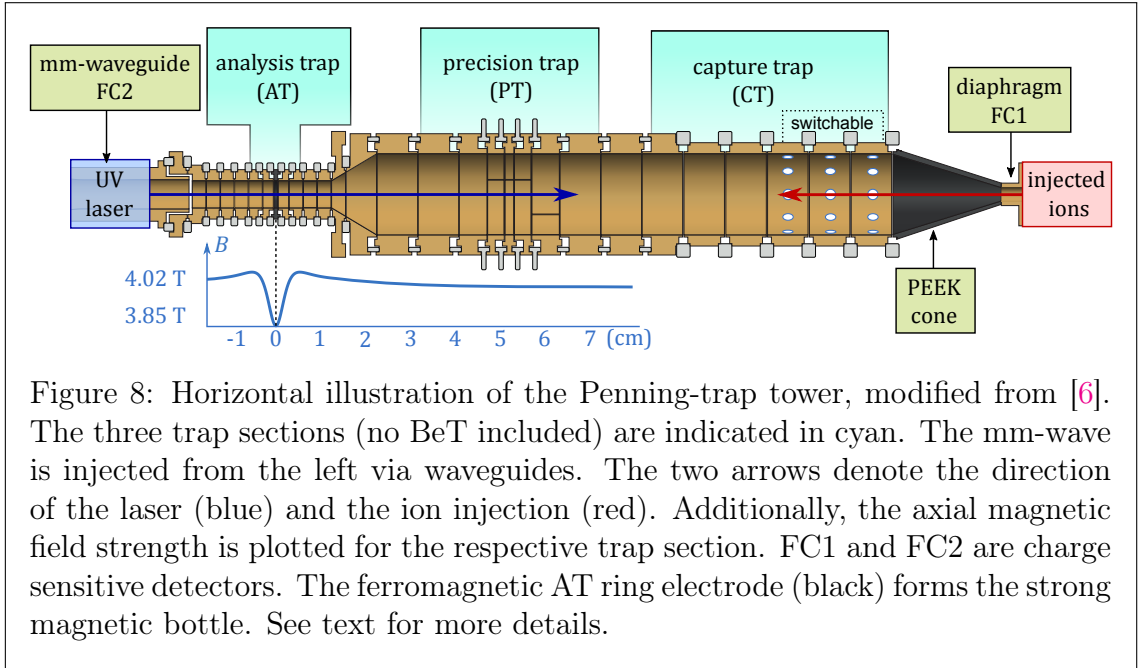


Figure 7: Overview of the magnet holding the cryostat (left) connected to the beamline (partly shown at the top right). The red dashed lines indicate the cut off transition from beamline to magnet. The HD-EBIT is not shown. The blue colored section in the cryostat is the 77 K stage, the violet section is the 4 K stage. See text for details. This figure is modified from [5].



the 4 K stage freezes out onto the surfaces except for helium and hydrogen. They are adsorbed only at unoccupied metallic spots. The cryogenic valve stops any further particle flux into the cryostat and a complete gas freeze-out occurs yielding virtually perfect vacuum.

3.2 The Inner Trap Tower

The heart of ALPHATRAP is the double Penning-trap setup shown in figure 8. In the precision trap (PT) we measure frequencies to high precision and induce spin-flips via millimeter-waves (mm-wave). In the analysis trap (AT) we detect successful spin-flips of the ion. The capture trap (CT) catches injected ions and stores them for later use. All three traps are separated by additional transport electrodes to move ions adiabatically²⁰ back and forth. The idea to use sympathetic laser cooling with beryllium came up after the trap design, thus a dedicated trap for this purpose has not been implemented yet. Nevertheless, for testing sympathetic coupling we have set up a provisional beryllium trap (BeT) within the framework of this thesis (see section 5.4.1).

3.2.1 Capture Trap - CT

Before entering the cryostat a pulse drift tube (see figure 7) decelerates the injected ion bunch to kinetic energies of about $q \times 150$ V. We can supply the six CT electrodes with ± 200 V and fast-switch the potential of the first three ones within $2 \mu\text{s}$. Ions are captured in the following way. The last electrode is set to a higher voltage than the residual ion's E_{kin}/q for repulsion, while the fast-switchable entrance electrodes are switched upon passing ions from an initial low potential to a likewise repelling

²⁰Meaning that the energy change of the ion during transport is negligible [33].

potential. By adjusting this process to the energy distribution of the ion bunch the capture efficiency can be optimized. To this end, the top diaphragm and the mm-waveguide at the bottom of the trap are operated as charge sensitive detectors (FC1/2 in figure 8) to measure the time of flight and the kinetic energy of the ions. After a successful capture the ions are stored in the CT and transported to the measurement traps if needed.

3.2.2 Precision Trap - PT

In the PT we measure $(\omega_z, \omega_+, \omega_-)$ to calculate the free cyclotron frequency ω_c . We also induce spin-flips of the ion and sample the Larmor resonance from successful spin-flips (see e.g. [6]). The trap is based on the design from [25] used at LIONTRAP, but scaled to larger dimensions ($\rho = 9$ mm) to suppress especially the image charge shift [51]. The PT is a 7-electrode trap configuration with two pairs of correction electrodes. At the cost of a more complex system than the 5-electrode trap (see section 2.3) we can tune out even higher order field imperfections up to C_{10} . This improves the harmonicity of the electric trapping potential and the frequency measurement accuracy. The ring and inner correction electrodes are half-split for dipole and quadrupole excitation while the upper outer correction electrode is quarter-split for mode coupling. The residual transport electrodes act as one combined long endcap.

3.2.3 Analysis Trap - AT

The AT is designed for spin-state detection via the continuous Stern-Gerlach effect [15] and has a ($\rho = 3$ mm) inner radius. To this end, the AT ring electrode is ferromagnetic and generates a strong magnetic field inhomogeneity B_2 called *magnetic bottle*. For the ion this represents a magnetic field imperfection (analogous to the electric imperfection) and shifts the axial frequency depending on its internal spin-state. We then compare the axial frequency in the AT before and after a mm-wave spin-flip attempt and therefore can detect successful spin-flips as long as the spin dependent shift is resolvable.

3.3 Laser System

The laser system must meet specific conditions set by the beryllium ion in order to laser cool it. The standard cooling transition between the $^2S_{1/2} \longleftrightarrow ^2P_{3/2}$ states has a vacuum wavelength of $\lambda_c = 313.132\,920(44)$ nm [53, 54], an excited state lifetime of $\tau = 8.1(4)$ ns [55], a natural linewidth of 19.7(10) MHz and a saturation intensity of $I_{\text{sat}} = 0.836(42)$ mW mm $^{-2}$ [5].

Our laser source is the commercial Toptica TA-FHG pro system [52] (see figure 9). It is located in an adjacent laboratory next to the ALPHATRAP magnet room. It produces the 313 nm beam via two second-harmonic generation stages (SHG and FHG) starting from a fundamental 1252 nm wavelength produced by an external cavity diode laser (ECDL) in Littrow configuration. A tapered amplifier (TA) stage enhances the initial 80 mW fundamental beam up to 1800 mW. The final FHG beam has up to ~ 300 mW exhibiting plenty of excess power for additional optics along the beam path to the Penning trap injection.

For the purpose of laser frequency stabilization the PID feedback of a WSU-2 [56] wavemeter, picking up a probe beam from the SHG stage, stabilizes the laser frequency with an accuracy of 2 MHz within the 10 nm vicinity of its calibration point. This point is an absolute frequency determined by a helium-neon reference laser (LJSC-3-11) [57]. It can be locked to an I $_2$ transition with an absolute uncertainty of 12 kHz. The wavemeter then is re-calibrated every 2 min.

As for the laser linewidth itself, measurements at 313 nm by the manufacturer and in [58] yielded linewidths of $\delta\nu_{\text{short}} = 27(3)$ kHz at 3 μ s and $\delta\nu_{\text{long}} = 191(3)$ kHz at 100 ms integration time, respectively. ²¹ Beyond the 100 ms scale the wavemeter regulation is active.

In conclusion the narrow intrinsic laser linewidth, which is two orders of magnitude smaller than the natural linewidth on a 100 ms timescale, is frequency stabilized to 2 MHz. This ensures reliable red detuning of the cooling laser relative to the cooling transition and allows efficient Doppler cooling with sufficient laser power.

A broader overview of our system can be found in [5, 7] and details on the laser system and its characterization in the work of S. Kraemer [58].

3.4 Mm-Wave and Laser Beam Injection

Two UV fused silica view ports at the bottom of the magnet, one at room-temperature the other at 4 K, allow transmission for both the mm-wave and the UV laser beam. A vertical cut view of the injection setup is shown in figure 10. The mm-wave passes three different pressure regions and is transported through the view ports via horn-to-horn transitions, which are anchored at the 77 K and 4 K stages. The waveguide has a 6 mm inner diameter and exhibits single-mode transportation for the 37 GHz wave. For 112 GHz operation an optional mode cleaner at the end of the wave guide, right before entering the trap tower, suppresses higher order modes.

²¹The 100 ms had been chosen as this is the minimal exposure time of the wavemeter due to experimental conditions

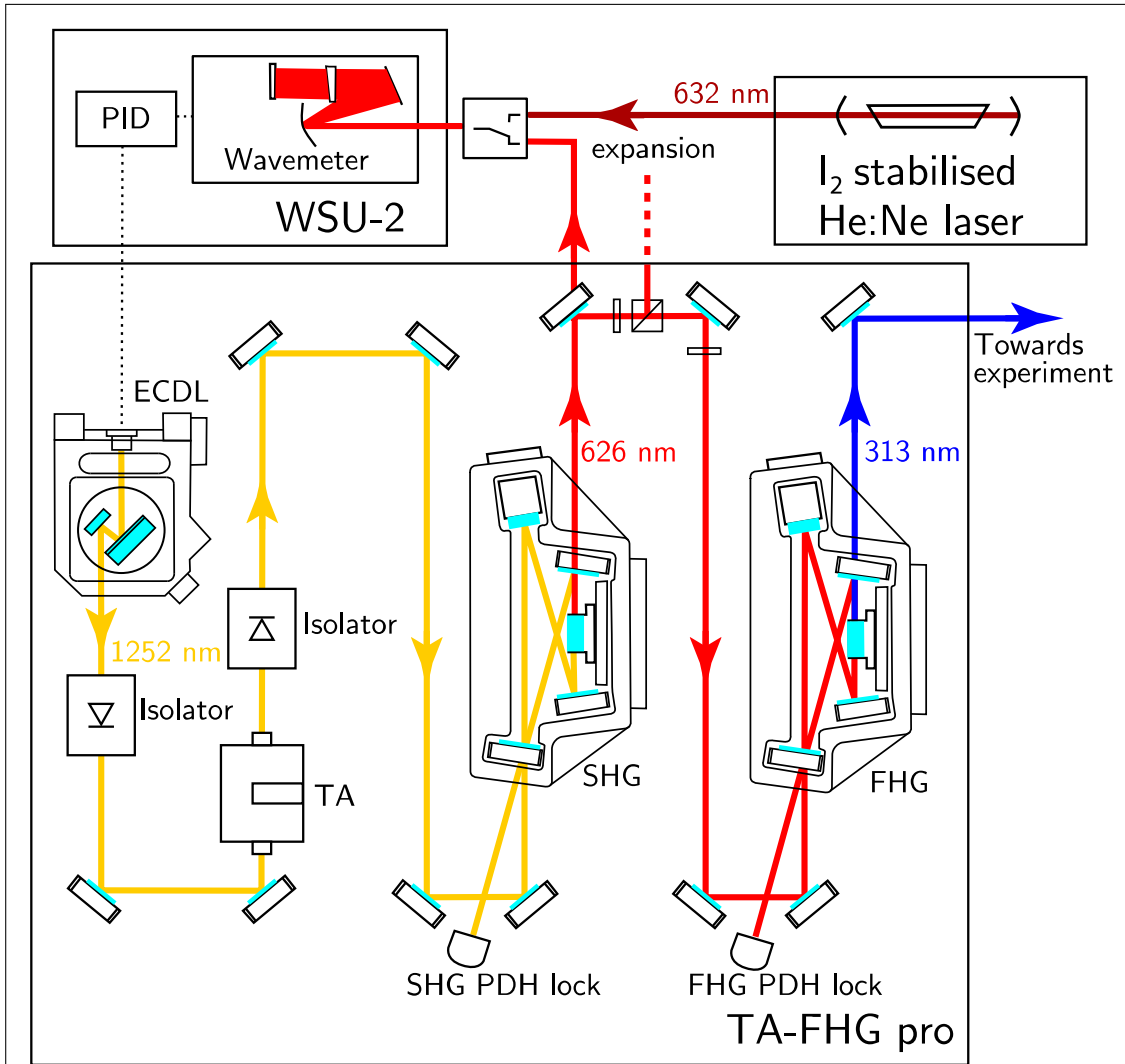
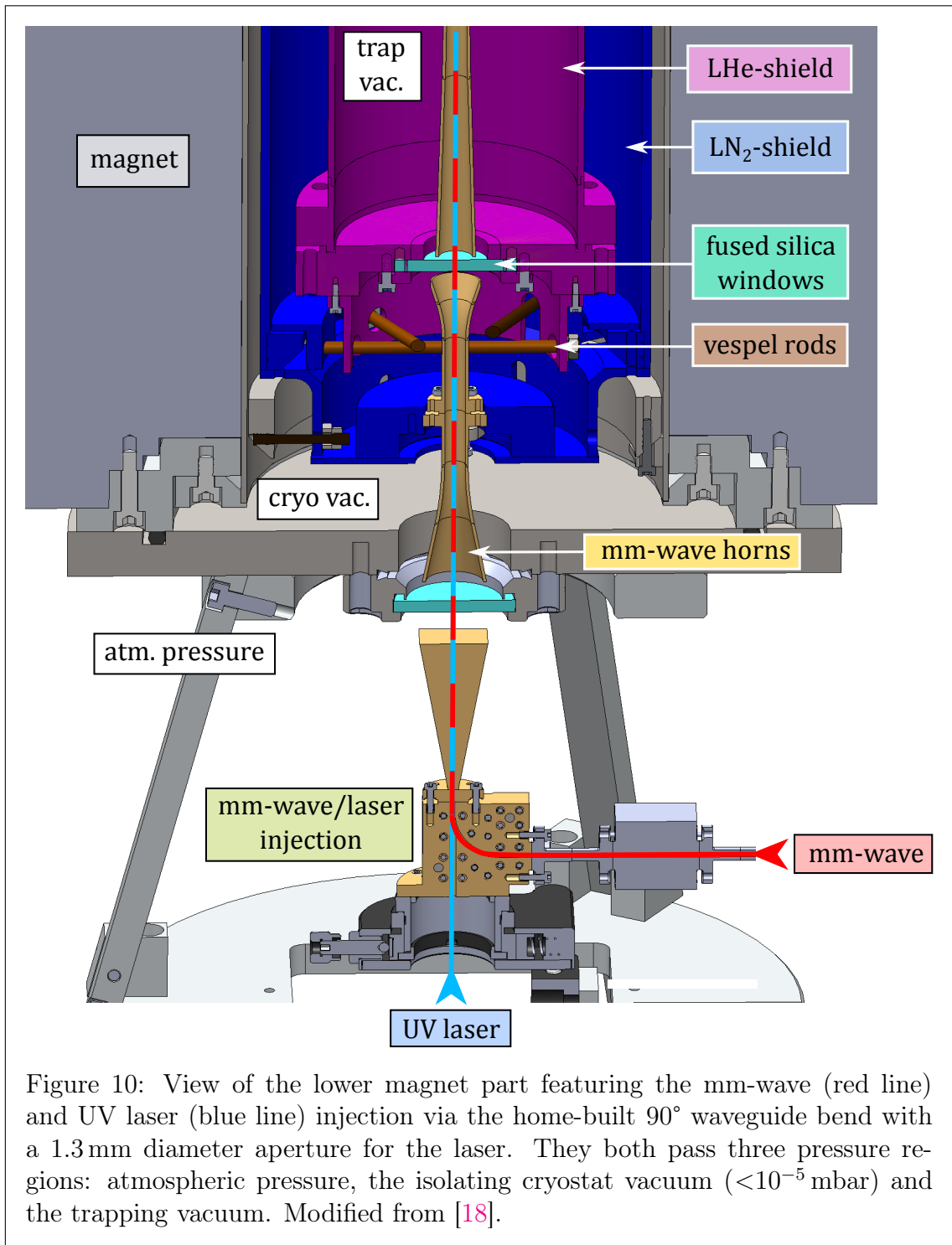


Figure 9: Overview of the laser setup including the wavemeter (top left with the PID loop), the He:Ne reference laser (top right) and the laser source (center box). The laser diode, the TA and the two higher harmonic cavity stages are all in the laser source box. Beam guiding optics are cyan coloured, mode matching optics are not drawn. Finally, the desired UV laser beam exits the housing through a sealable aperture. The scheme is taken from [52].



The mm-wave is brought in line with the cryostat via a vertical 90° bend of the waveguide. We drilled a hole in the bend of the lower frequency waveguide for laser beam access. The hole has a 2 mm diameter. The 112 GHz wave requires smaller waveguides, where such holes can potentially lead to unacceptable losses. Thus, a home-built waveguide bend with a tangential laser aperture of 1.3 mm is used allowing coupling of the laser while providing sufficient mm-wave transmission. It was built in [59].

A breadboard is mounted below the injection setup serving as an assembly area for optics to steer and couple the laser beam into the aperture. The laser is brought to the breadboard as a free beam from the adjacent laser laboratory. An optical telescope on the breadboard reduces the beam waist to fit the aperture. The telescope consists of two plano convex lenses with $f_1 = 150$ mm and $f_2 = 40$ mm in a Keplerian arrangement. The beam waist is reduced by a factor of

$$S = \frac{f_1}{f_2} = 3.75. \quad (37)$$

The free beam path from the laser source to the trap tower is about $D \approx 5$ m and is prone to any form of mechanical vibration near the source. This distance represents a huge lever arm for beam pointing fluctuations in the trap. Especially problematic are fluctuations of the beam propagation angle over this distance. It can lead to a misalignment of the beam with respect to the ion position or even beam clipping at the waveguide aperture. The fluctuations became apparent in [7]. I will present a spatial laser beam alignment and stabilization in the next section 4.

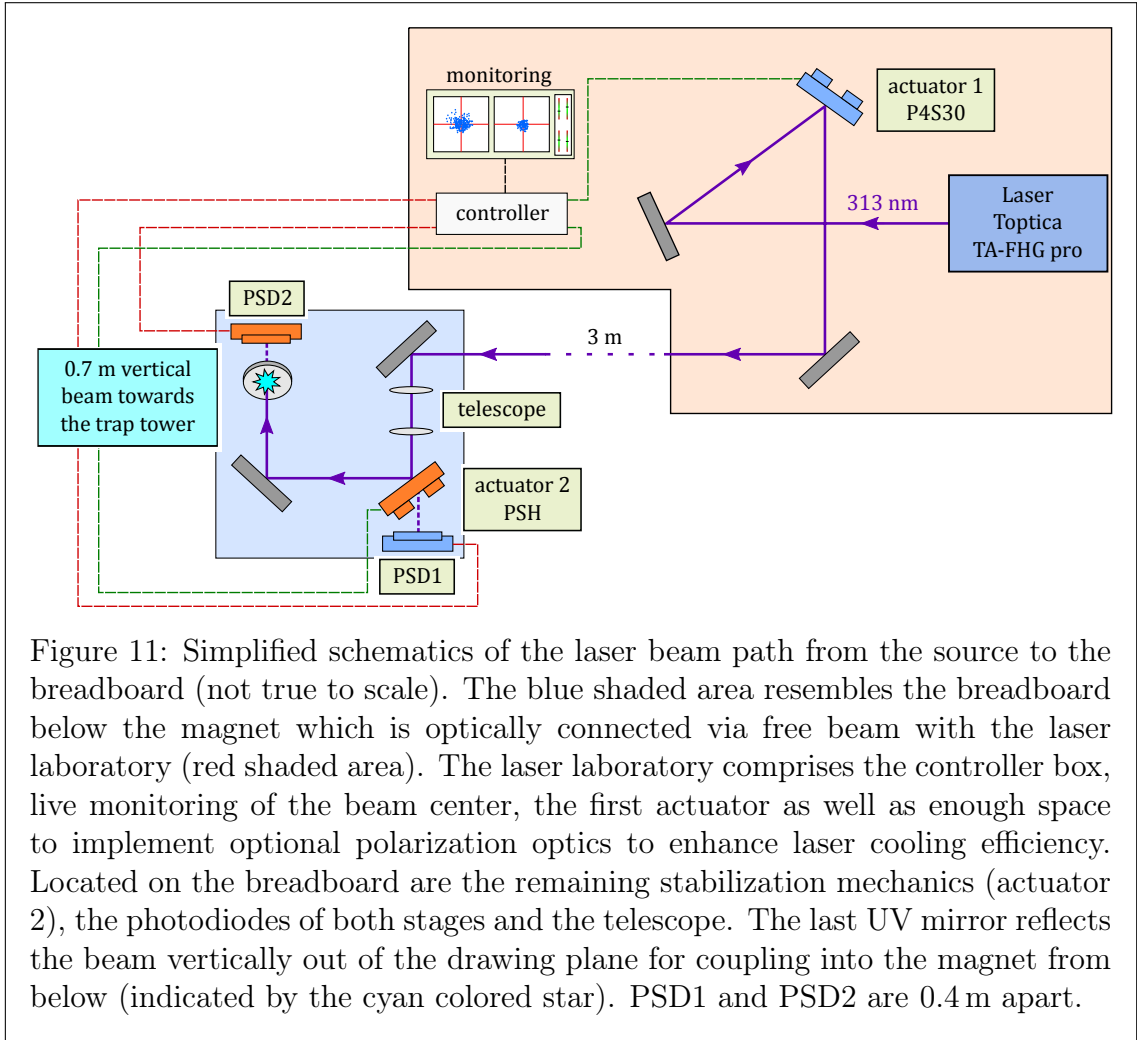


Figure 11: Simplified schematics of the laser beam path from the source to the breadboard (not true to scale). The blue shaded area resembles the breadboard below the magnet which is optically connected via free beam with the laser laboratory (red shaded area). The laser laboratory comprises the controller box, live monitoring of the beam center, the first actuator as well as enough space to implement optional polarization optics to enhance laser cooling efficiency. Located on the breadboard are the remaining stabilization mechanics (actuator 2), the photodiodes of both stages and the telescope. The last UV mirror reflects the beam vertically out of the drawing plane for coupling into the magnet from below (indicated by the cyan colored star). PSD1 and PSD2 are 0.4 m apart.

4 Laser Beam Stabilization

To reduce beam pointing fluctuations inside the trap either the long lever arm of the free beam path can be bypassed by an optical single mode fiber or the laser beam can be actively stabilized by a dedicated regulation system.

Optical fiber bulks are prone to solarization effects giving rise to the formation of active optical color centers, that scatter light out of the guided mode [60] into the fibers radial modes. Solarization is especially problematic for UV radiation and is even more unfavorable for single mode fibers as they hold higher energy densities within their small core diameter. It was shown that the color centers can be passivated by hydrogen bonds [61, 62] to become optically inactive. UV compatible single mode fibers are still in research and not fully commercial yet. There exist construction manuals for H₂-loaded UV fibers showing no degradation within days or weeks after they were initially cured by UV light exposure [60, 63].

Instead of a fiber, we use a laser beam pointing stabilization system (‘Compact’ by MRC Systems) [64]. It also allows us to steer the pointing inside the trap. Its

integration into the free beam path is shown in figure 11. Two UV (200 nm to 1000 nm) position sensitive photodiodes (PSD) combined with two steering actuators (P4S30, PSH) facilitate a 4-axes regulation (position and angle). The P4S30 features a ± 2 mrad regulation angle driven by a stack of 4 piezos. It is placed near the laser and fluctuation source and has a self-resonance frequency above >1200 Hz. The PSH is mounted on the breadboard. It has an aperture for mirror leakage such that the first detector (PSD1) can be placed directly behind the actuator. The PSH construction has a self-resonance of ~ 840 Hz and a ± 1 mrad regulation angle. The second detector (PSD2) is placed behind the last mirror, that couples the beam into the waveguide aperture, and picks up the residual mirror leakage.

The two PSDs have a continuous measurement area and locate the center of maximal intensity of the beam within a $10 \times 10 \text{ mm}^2$ area. They exhibit an integrated digital potentiometer to increase the detection sensitivity by a factor of 20.

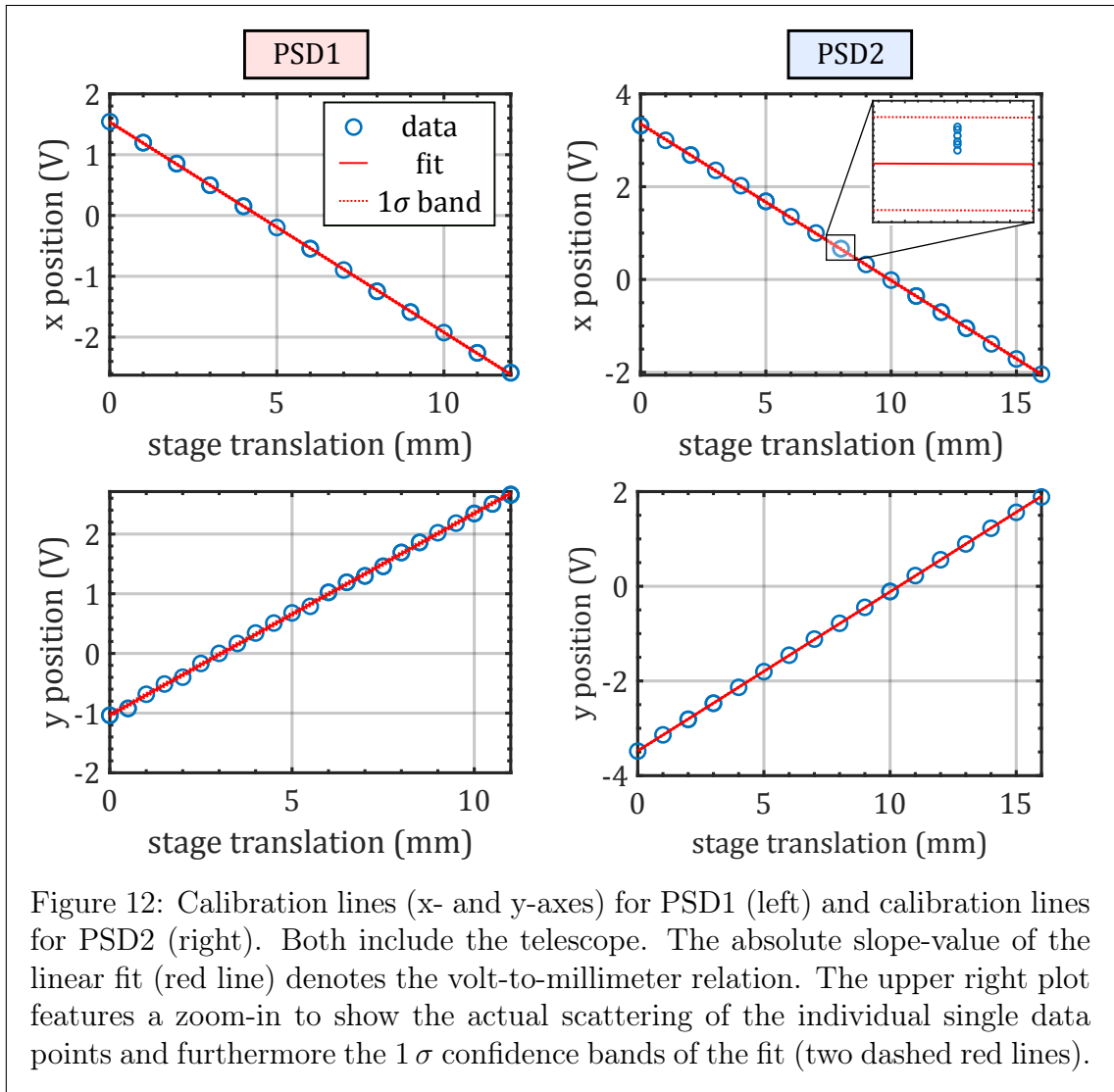
The detected beam position is read out by the controller box that feeds the actuators with a feedback signal based on PID regulation to steer the pointing back to the regulation point. A read-out interface allows live monitoring and data recording of the beam center position. Furthermore, the regulation point can be set manually on the PSDs measurement areas.

A large detector–actuator distance, a small laser beam waist due to the telescope and an optional high beam intensity should allow accurate beam pointing stabilization.

4.1 Calibration

The x- and y-position read out of the two PSDs has to be converted from volts to a length unit. For the calibration one PSD at a time and the telescope were mounted on translation stages (similar to the calibration done in [65]) and moved simultaneously and orthogonal through the laser propagation axis in steps of 0.5 or 1 mm. The beam center position was recorded for 30 s for each step with a data acquisition rate of about 45 Hz. The PSD is then rotated by 90° and the calibration scheme is repeated for the other axis.

The voltage-to-translation ratios with the telescope for each axis and both PSDs are plotted in figure 12. A linear fit model shows a linear dependency in all four cases. I did not average over the individual ~ 1350 acquired data points during each step to circumvent explicit statistical mean error calculation. While they appear as one single data point in the plots of figure 12, the zoom-in reveals their scattering and additionally the 1σ confidence bands of the fits. In table 1 the linear slopes of the fits from the figure are presented. The table includes furthermore the cases without (wo) the telescope (not plotted). The error composition is explained in the caption. Since the telescope reduces the beam translation on the detectors surface, we can determine the real beam size reduction by $S = \text{slope}_{1_{\text{wo}}}/\text{slope}_1$ for the x- and y-axis and get $S_x = 3.647(13)$ as well as $S_y = 3.641(11)$, respectively. The errors are based on Gaussian error propagation. The two values agree with each other well within their error bars but deviate significantly to the nominal S -factor from (37). The reason for the large discrepancy is that the telescope lenses are not perfectly distanced by their combined focal length $f_1 + f_2$. Nonetheless, using the



calculated factors $S_{x,y}$ we determine $\text{PSD2}_{\text{wo},x,y}^{\text{est}} = \text{PSD2} \cdot S_{x,y}$ for both axes. They are listed in the last column of the table.

Table 1: This table lists all voltage-to-mm calibration slopes with and without telescope (wo). The errors arise from the $10\mu\text{m}$ translation accuracy of the translation stages. The 1σ confidence bands of the fits yield errors below $<0.1\text{ mV mm}^{-1}$ in all cases and are thus neglected. Also, errors that result from a geometric misalignment of the stages, such that the translation of detector and telescope are not perfectly orthogonal with respect to the beam direction, are below $<2.2\mu\text{m}$ over 16 mm stage translation and negligible as well.²² The errors for the estimated $\text{PSD2}_{\text{wo}}^{\text{est}}$ values are due to Gaussian error propagation.

(V mm ⁻¹)	slope1	slope2	slope1 _{wo}	slope2 _{wo} ^{est}
x-axis	0.3458(6)	0.3375(4)	1.261(4)	1.231(5)
y-axis	0.3381(6)	0.3361(5)	1.231(3)	1.224(4)

4.2 Performance

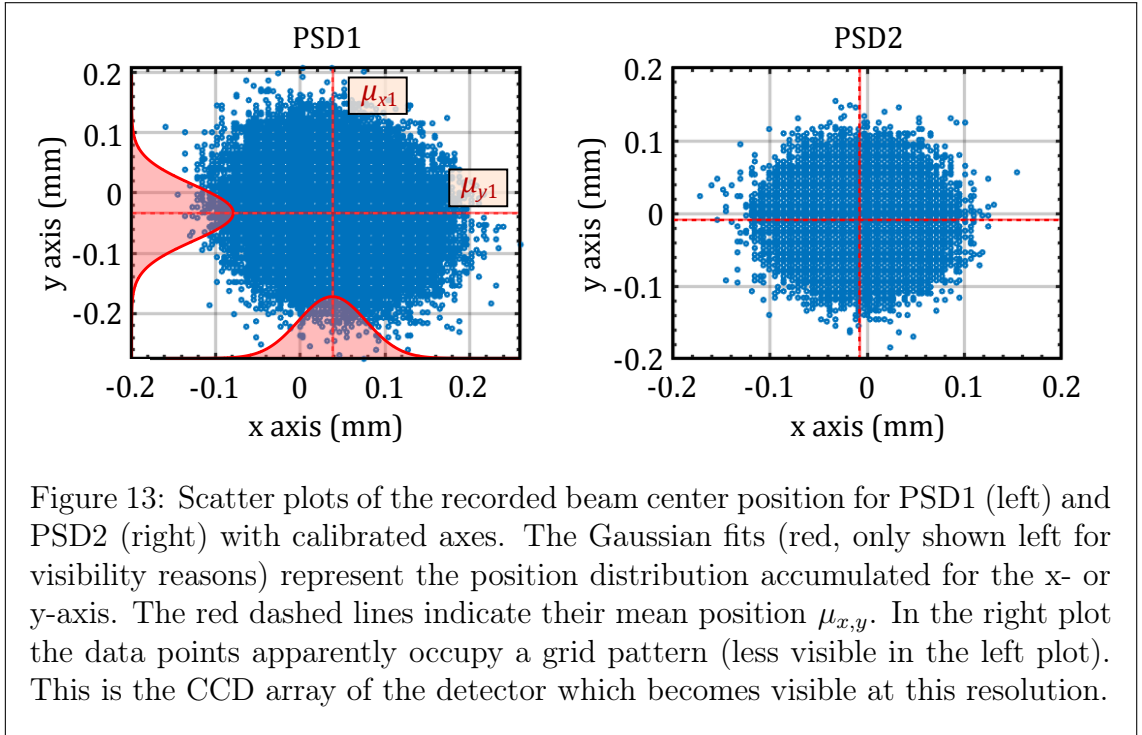
To verify the performance of the stabilization the laser beam center was monitored and recorded for 10 h in a test run including the telescope. Scatter plots of the recorded beam center fluctuations are in figure 13 for the calibrated PSD1 (left) and PSD2 (right). Fitting a normal distribution function to the accumulated data (see left plot) for both axes yields the mean beam center position $\mu_{x,y}$ and the distribution width $\sigma_{x,y}$ for the corresponding axis. They are listed in table 2. The red lines mark the $\mu_{x,y}$ values such that their cross-section denotes the actual mean beam center position.

We do not have a reference performance yet without the stabilization system for comparison. However, in previous experiences it was observed that the beam center underneath the magnet could suddenly shift up to millimeters due to active construction works, door snapping and a variety of other high-impact disturbances. These sudden as well as long term shifts of the beam pointing should be efficiently suppressed by the stabilization to the above estimated precision. This is of course only true as long as the deflection angle does not exceed the mechanical regulation angles of the P4S30 or the PSH.

An analysis of the regulation response of the stabilization system to varying perturbation frequencies of beam fluctuations would also be of interest. Especially beam fluctuations near the actuators' self-resonance frequencies²³ might not be controllable.

²²This would correspond to an orthogonal misalignment angle of $<1^\circ$ which I did not observe.

²³The actual resonance frequency might differ from the one stated above by the manufacturer depending on setup and mounting.



A simple mirror, driven by a sinusoidal disturbance signal of varying frequency, could simulate beam fluctuations. This has been tested in [65] with the same MRC, however only a 2-axes (single P4S30 actuator) regulation was used in their response test. Frequencies between 15 Hz to 300 Hz and 70 Hz to 300 Hz, depending on low or high control bandwidth setting, could not be stabilized effectively.

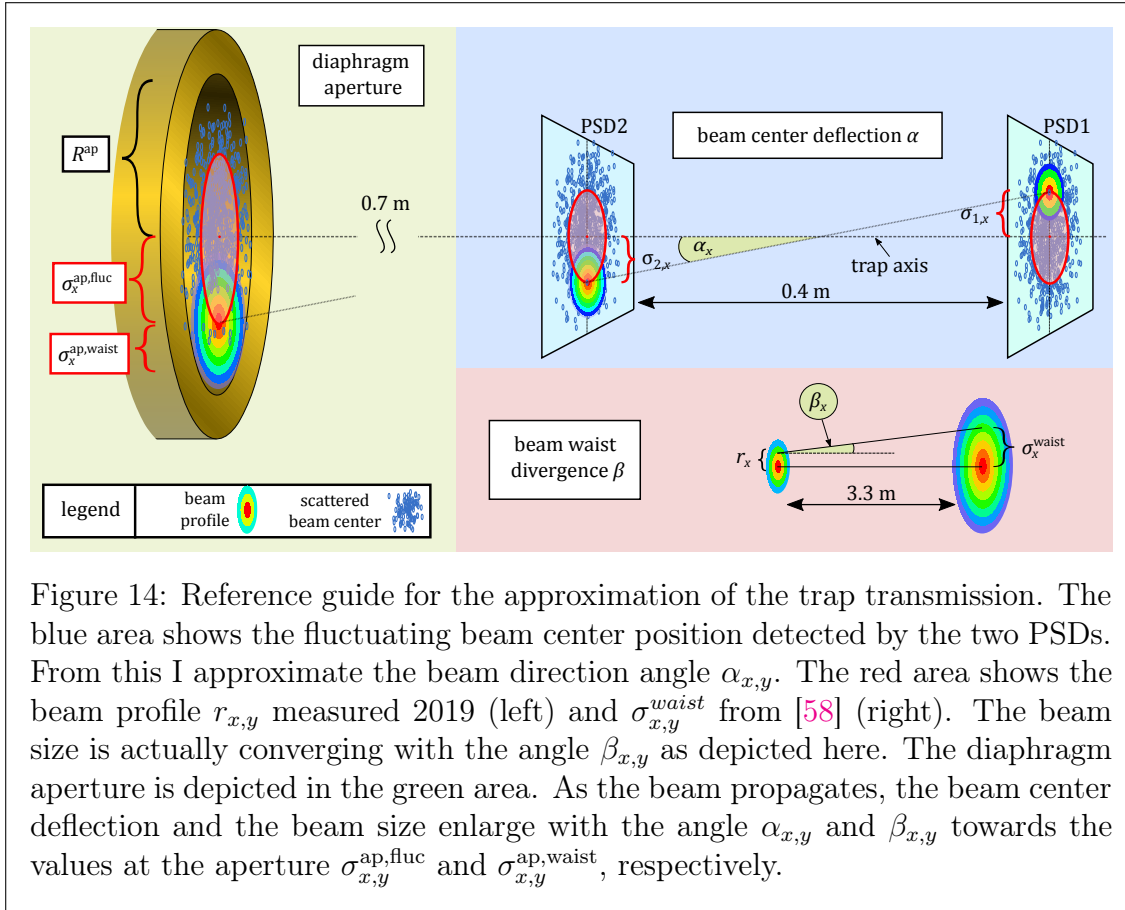
Table 2: The mean of the beam center positions and their distribution widths for PSD1 and PSD2 correspond to the two scatter plots in figure 13. The column labels denote the (x, y) axes of the respective PSD (1 or 2). Errors denote the 1σ confidence interval of the parameters for the normal distribution fits.

(μm)	x1	y1	x2	y2
center μ	38.29(15)	-33.13(17)	-7.46(8)	-9.12(9)
width σ	40.16(11)	47.18(14)	25.24(7)	28.28(7)

4.3 Trap Transmission

Experiences with frequency shifts were made in connection to laser radiation inside the trap tower [7, 66, 67]. Most likely this phenomenon arises due to local charge accumulation in the frozen-out gas monolayer induced by the laser.²⁴ This can turn

²⁴After renewing this monolayer of frozen-out gas by heating and degassing our trap chamber, we have made the observation that the potential settings of our AT were reset back to the settings



out to be a severe problem as this steadily causes local surface potential changes making measurements imprecise or even impossible.

To solve this either the beam is dumped in a controlled fashion inside the trap or it is properly guided out of the trap. The most straightforward way without any further implementation of optics or redesign of the trap tower would be to align the laser beam well enough with the vertical trap axis and have it exit the trap tower through the 3 mm wide diaphragm above the CT with little scattering.

A viewport at the top end of the beamtube is in direct line of sight with the vertical axis of the trap tower (see figure 7). With the cryovalve open the laser beam can be coupled out of that viewport. This can be used to perform an initial beam alignment and to set the regulation point on the PSDs of the stabilization system. The cryovalve is closed afterwards and from there on the beam consistently leaves the trap tower with active stabilization and gets effectively dumped inside the beamtube. The only requirement is a wedged surface of the cryovalve to suppress direct back-reflection into the trap tower. To get an idea of how much laser power is already scattered inside the trapping volume I approximate the laser transmission through the trap tower in the following paragraphs.

used before the laser-campaign in [7]. Therefore, we conclude that the laser had induced charges that were carried away with the degassing procedure.

Since the ion injection diaphragm (see FC1 in figure 8) represents with a diameter of $\rho = 3$ mm the most critical part in the laser beam path, the finite dimension of the laser beam together with an uncompensated deflection angle leads to a clipping of the beam and thus to photons being scattered into the trap volume. The greater the deflection the more laser power is dumped inside the trap tower, leading to uncontrollable frequency shifts. In the following paragraph I approximate the order of magnitude of the laser power transmission through the aperture of the diaphragm. Figure 14 serves as a reference guide for this estimation.

I assume a perfectly aligned regulation point of the stabilization system with the diaphragm aperture center. Then I consider two effects that contribute to power losses due to beam clipping in the x- and y-axis, respectively. First, the beam center fluctuates around the regulation point with the standard deviations $\sigma_{x,y}^{\text{ap,fluc}}$. Second, the beam itself extends over a finite length. On the basis of [58] I assume a Gaussian beam profile for our cooling laser with standard deviations $\sigma_{x,y}^{\text{ap,waist}}$ at the aperture. The overall power distribution across the plane of the aperture is then a superposition of two Gaussian functions with the overall standard deviation

$$R_{x,y} = \sqrt{\left(\sigma_{x,y}^{\text{ap,fluc}}\right)^2 + \left(\sigma_{x,y}^{\text{ap,waist}}\right)^2}. \quad (38)$$

For the estimation of the beam center fluctuation $\sigma_{x,y}^{\text{ap,fluc}}$ at the aperture I consider the following: with an ideally stabilized beam direction, the scattering profile at PSD2 would imprint itself at the aperture in $L_1 \approx 0.7$ m distance with equal size. Since the stabilization is not perfect, I allow a residual deflection angle $\alpha_{x,y}$ of the beam direction. I assume a beam center deflection of $\sigma_{1,x,y} + \sigma_{2,x,y}$ over the 0.4 m distance between the two PSDs (see blue area in figure 14) and calculate the beam deflection angle. Then it is $\sigma_{x,y}^{\text{ap,fluc}} = \sigma_{2,x,y} + \tan(\alpha_{x,y}) \cdot L_1$.

For the estimation of the beam size $\sigma_{x,y}^{\text{ap,waist}}$ at the aperture the beam divergence $\beta_{x,y}$ over the beam path length must be taken into account. I compare the beam profile in front of the breadboard and near the laser source (approx. 3.3 m distance) to estimate the divergence (see red area in figure 14). The former profile $r_{x,y}$ has been measured in 2019²⁵, the latter I can calculate from the beam characterization done in [58]. Then it is $\sigma_{x,y}^{\text{ap,waist}} = r_{x,y} + \tan(\beta_{x,y}) \cdot L_2$, with the distance $L_2 \approx 1.1$ m from the front of the breadboard to the aperture.

The important geometrical values and results are listed in table 3. All values already include the effect of the beam size reduction by the telescope. The minus sign in $\beta_{x,y}$ indicates that the beam is actually converging. Nevertheless, at some point the beam must spread and diverge. I neglect any of this initial convergence of the beam and assume virtual spread-out right from the beginning of the laser aperture. The 1σ widths of the overall laser power distribution at the aperture is given by $R_{x,y}$. In the last column I compare this with the aperture radius $R^{\text{ap}} = 1.5$ mm to evaluate

²⁵The dimensions were $r_y^s = 0.8$ mm and $r_x^s = 0.5$ mm without the beam size reduction by the telescope. Thus, it is approx. $r_y \approx 0.22$ mm and $r_x \approx 0.14$ mm directly after the telescope.

Table 3: Values of the beam size at the breadboard $r_{x,y}$, the deflection and divergence angle $\alpha_{x,y}$ and $\beta_{x,y}$ and the standard deviation of the overall power distribution $R_{x,y}$ together with the relative deviation from the aperture radius. Since this is an order of magnitude estimation only, I do not give errors. All values include the beam size reduction of the telescope.

	r/mm	α/rad	β/rad	R/mm	R^{ap}/R
x-axis	0.14	1.6×10^{-4}	-1.53×10^{-4}	0.355	4.0σ
y-axis	0.22	1.9×10^{-4}	-1.32×10^{-4}	0.377	4.2σ

how much laser power transits the aperture for the respective axis. This corresponds to a surface containing 99.99% of the laser power that can geometrically enter the aperture, while 0.01% of the power is clipped and directly scattered back into the trap volume.

5 Ion-Ion Coupling

Here I present the main part of my thesis. It is accompanied by the appendix [A](#), [B](#) and [C](#) and starts with a motivational introduction, where I explain the reasons for an alternative sympathetic cooling technique and lay the starting point for the idea of a novel coupling scheme. Then, I give an analytical description of the coupling scheme and discuss simulations of it in detail. Afterwards, I illustrate the setup for a proof of principle measurement, review the results and compare them with the simulations.

5.1 Motivation for an Alternative Sympathetic Cooling Technique in a Penning Trap

For sympathetic laser cooling an interaction between one or more particles of interest and a laser cooling medium needs to be established. In the case of Penning traps, where we can deal with ions only, Coulomb interaction is the apparent choice for this coupling. The most straightforward way to achieve coupling is by trapping the ions of interest and the auxiliary ions together in a single Penning trap. Sympathetic laser cooling has been successfully implemented this way in 1986 [\[68\]](#) using a two-species ${}^9\text{Be}^+ / {}^{198}\text{Hg}^+$ plasma and since then improved and extended to other ion species (e.g. [\[69\]](#) used highly charged Xe). Nowadays, also techniques exist that allow sympathetic laser cooling of single ions stored in a spatial double well of micro-traps [\[53, 70, 71\]](#). They arose within fields of application such as quantum simulation, information and logic gate computing. However, even for such advanced sympathetic cooling techniques, they come with a significant drawback for e.g. high-precision g -factor experiments such as ALPHATRAP as the ions cannot be separated on a macroscopic scale. Co-trapping the ion of interest with the laser cooled ion in a single Penning trap perturbs its motion to a highly unwanted degree. To this end, a different cooling technique has to be employed.

In 1990 Heinzen and Wineland [\[14\]](#) proposed a novel sympathetic cooling technique to trap the two ions in two traps that share a common endcap. Their axial motions induce charges in this common endcap and exert forces on the respective other ion, thus enabling indirect Coulomb coupling. In a quantum oscillator approach they calculated a time constant for the energy exchange between the ions – denoted here by the subscripts 1 and 2 – to be

$$t_{\text{ex}} = \frac{\pi \tilde{\omega}_z D_{\text{eff},1} D_{\text{eff},2} \sqrt{m_1 m_2}}{q_1 q_2 \sqrt{N_1 N_2}} C_p. \quad (39)$$

$D_{\text{eff},i}$ is the effective electrode distance of the respective trap, m_i , q_i and N_i are the mass, charge and the amount (in case we are dealing with multiple ions in a cloud) of the respective ion species, $\tilde{\omega}_z$ is the shared and pushed axial frequency of both ions and C_p is the total parallel trap capacitance.²⁶ To evoke an idea, one can think of a

²⁶ C_p combines all stray capacitances into one total parallel capacitor. Since two separate traps are now involved, C_p no longer models one trap but rather combines the stray capacitances of

single HCI in trap 1 that is coupled to the cooling medium consisting of a coherent cloud of $N_2 = 100$ laser-cooled ${}^9\text{Be}^+$ ions in trap 2. The axial modes can couple when their detected frequencies overlap at $\tilde{\omega}_{z,1} = \tilde{\omega}_{z,2} \equiv \tilde{\omega}_0$.²⁷ The radial modes of the HCI can be addressed with sideband coupling together with laser-cooling of the beryllium ions. The above technique is currently implemented in the BASE experiment [72]. Details can be found in [66].

From an experimental point of view a long t_{ex} significantly constrains this cooling technique. Time variations of the trapping fields lead to frequency fluctuations, here referred to as *jitter*. Coherent mode coupling and efficient energy transfer can only happen when frequency overlap is held throughout the coupling operation. Longer t_{ex} are substantially prone to frequency jitter of either ion and will suppress the cooling scheme efficiency. It is therefore important to retain t_{ex} short, which is not necessarily given for low q/m ions. However, the parameters defining t_{ex} allow only limited control to reduce the time constant. One relies on the initial trap and particle composition and lacks the flexibility to apply this cooling technique to different ion species.

This thought was the starting point of this thesis to come up with an alternative concept for sympathetic laser cooling in a Penning trap.

Eq. (39) gives access to a variety of parameters to enhance the coupling strength and shorten t_{ex} . But all of them are bound by practical limitations.

First of all, the coupling is obviously stronger for higher q/m ions. Concerning the cooling medium, singly ionized beryllium is typically the ion of choice. It is easy to produce and provides a convenient 313 nm laser cooling transition. We are not bound to a single beryllium ion but can rather trap up to $N_2 \sim 1000$ ions as a manageable coherent cloud. Unfortunately the square root of the ion number gives this parameter an unfavorable scaling.

The effective electrode distance D_{eff} of measurement traps could be reduced to a few millimeter as long as geometry requirements for a compensated/orthogonal trap are met, which bind e.g. the electrode's radius to its length. But we can see problems of small traps already from the proportionality $\omega_z \propto \sqrt{C_2 U_r / d_{\text{char}}^2}$ from eq. (5). If d_{char} is small, we need to supply a smaller ring potential U_r to retain identical axial frequency. This however worsens the signal-to-noise ratio of the voltage source and also any voltage-to-patch-potential²⁸ ratio. Smaller electrodes are also unwanted because they facilitate image charge shifts and the ion motion is more affected by higher order field imperfections. The beryllium trap (BeT) does not need to meet the high precision standard of a measurement trap. Its radius can be decreased as long as coherent trapping can be controlled and the ions are not lost to the electrode surface. We can also think to lower the coupling frequency $\tilde{\omega}_0$. The resonator detection range limits this to only a small fractional change though.

both traps and their connections.

²⁷We will see in section 5.3 that the pushed frequencies need to overlap rather than the original ones.

²⁸Patch potentials are local charge accumulations on the electrode surfaces. See e.g. [25] for further information.

In contrast to the trap properties discussed so far, C_p is the only trap parameter that does not result in additional jitter. The C_p can be reduced by proper trap design or by shunting it with an inductance which is also shortly mentioned in [14]. The latter is the equivalent to a resonator and was to our knowledge never taken further into consideration. Therefore, we propose a novel coupling technique utilizing a common resonator as the interaction bridge. This brings along two main advantages:

1. We can position the two traps spatially apart anywhere in the trap tower as long as they are both connected to the same resonator.
2. We can effectively minimize C_p by orders of magnitude with the shunting effect of the resonator's inductance.

5.2 Effective Resonator Model

Before I go into the description of the common resonator coupling, it will be useful to describe the resonator impedance somewhat differently than in eq. (18). I break down the impedance into its real and complex part and define the components

$$Z_{\text{res}} = \text{Re}(Z_{\text{res}}) + i \text{Im}(Z_{\text{res}}) \equiv Z_{R_{\text{eff}}} + Z_{C_{\text{eff}}}. \quad (40)$$

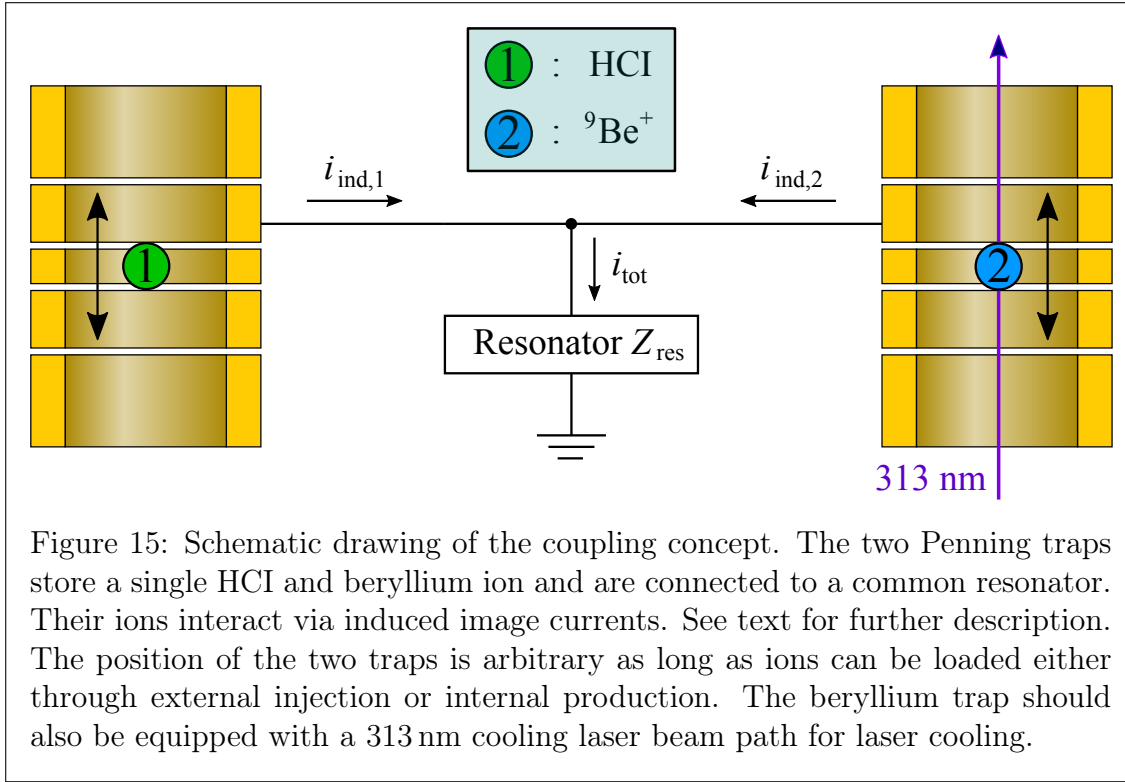
This way the resonator impedance is fully described by a two component series circuit rather than a parallel RLC-circuit: the real part of the resonator is a variably effective resistance R_{eff} and the complex part is a variably effective capacitance C_{eff}

$$\begin{aligned} Z_{R_{\text{eff}}} = R_{\text{eff}} &\quad \longrightarrow \quad R_{\text{eff}}(\omega) \equiv \text{Re}(Z_{\text{res}}), \\ Z_{C_{\text{eff}}} = -\frac{i}{\omega C_{\text{eff}}} &\quad \longrightarrow \quad C_{\text{eff}}(\omega) \equiv -\frac{1}{\omega \text{Im}(Z_{\text{res}})}. \end{aligned} \quad (41)$$

Instead of $Z_{C_{\text{eff}}}$, I could just as well introduce an inductive description for the complex resonator part via $Z_{L_{\text{eff}}}$. With the detuning from the resonator center $\Delta_r = \omega - \omega_r$ we can approximate (see appendix A) the effective resonator components via

$$C_{\text{eff}}(\omega) \approx 2C_p \frac{\Delta_r}{\omega_r} \quad \text{and} \quad R_{\text{eff}}(\omega) \approx \frac{R_p \omega_r^2}{4Q^2 \Delta_r^2}. \quad (42)$$

These approximations do not hold near the resonator center but the relative deviations $\delta C_{\text{eff}}/C_{\text{eff}}$ and $\delta R_{\text{eff}}/R_{\text{eff}}$ between eq. (41) and (42) rapidly fall off with the detuning. For our AT resonator at $\Delta_r = 2\pi \times 50$ Hz they are both approx. $\sim 20\%$ and at $\Delta_r = 2\pi \times 150$ Hz already $\sim 2\%$. Towards very large detuning $\omega_r \ll \Delta_r$ the deviations slowly increase again. No deviation is expected at $\Delta_r \approx 2\pi \times 502$ Hz for C_{eff} and at $\Delta_r \approx 2\pi \times 575$ Hz for R_{eff} .



5.3 Interaction of Two Ions Coupled via a Common Resonator

In this section I derive an analytical description of the two ions coupled via the common resonator. Figure 15 depicts the concept of the ion-ion coupling. For simplicity, I set $N_2 = 1$ to a single beryllium ion. Each ion induces an image current into the resonator according to eq. (16). They combine to an overall current $i_{\text{tot}} = i_{\text{ind},1} + i_{\text{ind},2}$ which gives rise to a voltage drop $u_{\text{tot},\text{sig}}$ across the resonator.²⁹ The resulting retroactive force by the resonator acts on the axial mode of both ions and couples them:

$$\ddot{z}_1 = -\omega_{z,1}^2 z_1 - \frac{q_1}{D_1 m_1} u_{\text{tot},\text{sig}} \stackrel{(22)}{=} -\omega_{z,1}^2 z_1 - \frac{q_1^2 Z_{\text{res}}(\omega_{z,1})}{D_1^2 m_1} \dot{z}_1 - \frac{q_1 q_2 Z_{\text{res}}(\omega_{z,2})}{D_1 D_2 m_1} \dot{z}_2, \quad (43a)$$

$$\ddot{z}_2 = -\omega_{z,2}^2 z_2 - \frac{q_2}{D_2 m_2} u_{\text{tot},\text{sig}} \stackrel{(22)}{=} -\omega_{z,2}^2 z_2 - \frac{q_2^2 Z_{\text{res}}(\omega_{z,2})}{D_2^2 m_2} \dot{z}_2 - \frac{q_2 q_1 Z_{\text{res}}(\omega_{z,1})}{D_2 D_1 m_2} \dot{z}_1. \quad (43b)$$

The amplitudes of the two ions are modulated with the generalized Rabi frequency $\tilde{\Omega}_G$ (similar to the sideband coupling in section 2.5.2), which describes an oscillatory energy/amplitude transfer between the ion modes. I further split Z_{res} into the

²⁹For a cooling medium of N beryllium ions their induced current will be $i_{\text{tot},2} = N_2 i_{\text{ind},2}$ assuming they oscillate coherently.

effective parameters R_{eff} and C_{eff} via eq. (40):

$$\ddot{z}_1 = - \underbrace{\left(\omega_{z,1}^2 + \frac{q_1^2}{D_1^2 m_1 C_{\text{eff},1}} \right)}_{\tilde{\omega}_{z,1}^2} z_1 - \frac{q_1^2 R_{\text{eff},1}}{D_1^2 m_1} \dot{z}_1 - \frac{q_1 q_2 R_{\text{eff},2}}{D_1 D_2 m_1} \dot{z}_2 - \underbrace{\frac{q_1 q_2}{D_1 D_2 m_1 C_{\text{eff},2}}}_{k_1} z_2, \quad (44a)$$

$$\ddot{z}_2 = - \underbrace{\left(\omega_{z,2}^2 + \frac{q_2^2}{D_2^2 m_2 C_{\text{eff},2}} \right)}_{\tilde{\omega}_{z,2}^2} z_2 - \frac{q_2^2 R_{\text{eff},2}}{D_2^2 m_2} \dot{z}_2 - \frac{q_1 q_2 R_{\text{eff},1}}{D_1 D_2 m_2} \dot{z}_1 - \underbrace{\frac{q_1 q_2}{D_1 D_2 m_2 C_{\text{eff},1}}}_{k_2} z_1. \quad (44b)$$

Note that there is a -90° phase shift of the voltage across C_{eff} relative to the voltage drop across R_{eff} . I used $\dot{z} = i\omega_z z$ ³⁰ to incorporate this phase shift into the C_{eff} terms. The frequency shift $\omega_z \rightarrow \tilde{\omega}_z$ of the axial frequency is the resonator pushing effect introduced in eq. (27).³¹ Technically, $C_{\text{eff}}(\omega)$ depends on the original ion frequency and in fact the two ions see the resonator from different frequency positions if $\omega_1 \neq \omega_2$. Therefore, we must distinguish $C_{\text{eff},1} \equiv C_{\text{eff}}(\omega_1)$ and $C_{\text{eff},2} \equiv C_{\text{eff}}(\omega_2)$ for the two ions. For further derivation I omit the R_{eff} damping terms to simplify the calculations. This way I do not take a shift of the Rabi frequency into account, but the shift is in the first place negligible.

In appendix B I derive the generalized Rabi frequency $\tilde{\Omega}_G$ from the above EOM including a small ion detuning $\delta = \tilde{\omega}_{z,2} - \tilde{\omega}_{z,1}$:

$$\tilde{\Omega}_G = \sqrt{\delta^2 + \Omega_\delta^2} \quad \text{with} \quad \Omega_\delta = \frac{q_1 q_2}{D_1 D_2 \sqrt{\tilde{\omega}_0 (\tilde{\omega}_0 + \delta)} m_1 m_2} \frac{1}{C_{\text{eff}}^c(\omega_{z,1}, \omega_{z,2})}. \quad (45)$$

Here some new definitions appear. Without loss of generality it is $\tilde{\omega}_{z,1} \equiv \tilde{\omega}_0$ and $\tilde{\omega}_{z,2} = \tilde{\omega}_0 + \delta$. I also re-define a *combined* effective capacitance $C_{\text{eff}}^c(\omega_{z,1}, \omega_{z,2}) \equiv \sqrt{C_{\text{eff},1} C_{\text{eff},2}}$. For small $\delta \sim \text{Hz}$ however I can just as well write $C_{\text{eff}}^c(\omega_{z,1}, \omega_{z,2}) \approx C_{\text{eff},1} \approx C_{\text{eff},2} \equiv C_{\text{eff}}$. Eq. (42) approximates the deviation between $C_{\text{eff},1}$ and $C_{\text{eff},2}$ to about $\sim 3\%$ for $\delta = 2\pi \times 5 \text{ Hz}$.³² Note that Ω_δ takes on the role of the Rabi frequency Ω_R as long as the ions are detuned. When the detuning vanishes $\delta \rightarrow 0$ it is simultaneously $\tilde{\Omega}_G \rightarrow \Omega_\delta \rightarrow \Omega_R$.

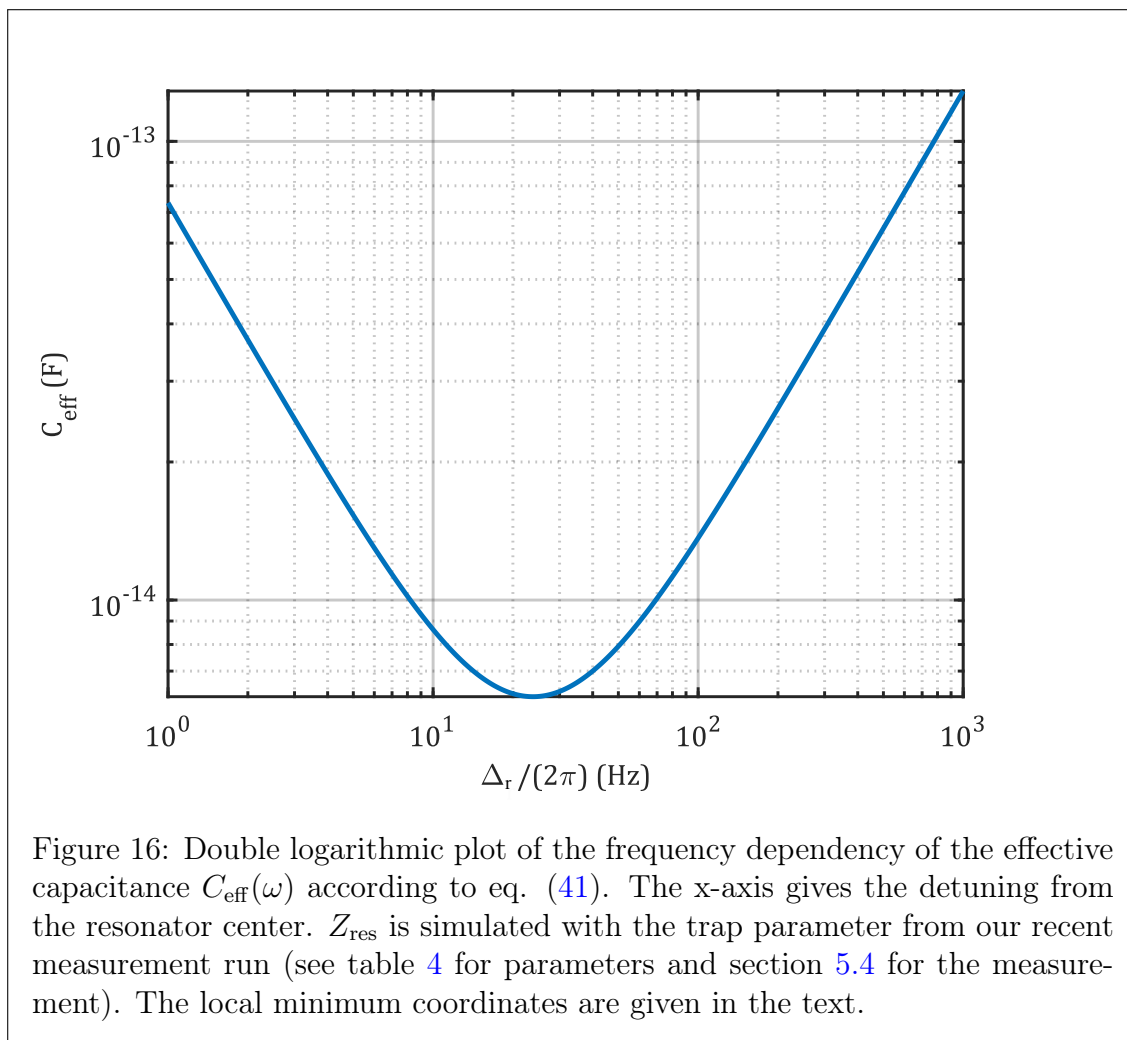
The ion energies are exchanged after half an oscillation of $\tilde{\Omega}_G$. This is often referred to as a π -pulse and allows me to introduce a time constant for one such π -pulse

$$\tau_{\text{ex}}(\tilde{\omega}_0, \delta) = \frac{\pi}{\tilde{\Omega}_G}. \quad (46)$$

³⁰This follows from the general ansatz $z = z_0(t) \exp(i\omega_z z)$ and approximating $\dot{z} = \dot{z}_0 \exp(i\omega_z z) + i\omega_z z_0 \exp(i\omega_z z) \approx i\omega_z z$ by neglecting the second term.

³¹Note that this is only the approximation made in eq. (27). The damping term also contributes to the shift, but this is comparably a very marginal effect though.

³²Remarkably this is independent of Δ_r . The question is whether this deviation is valid which is true at $\Delta_r = 2\pi \times 150 \text{ Hz}$.



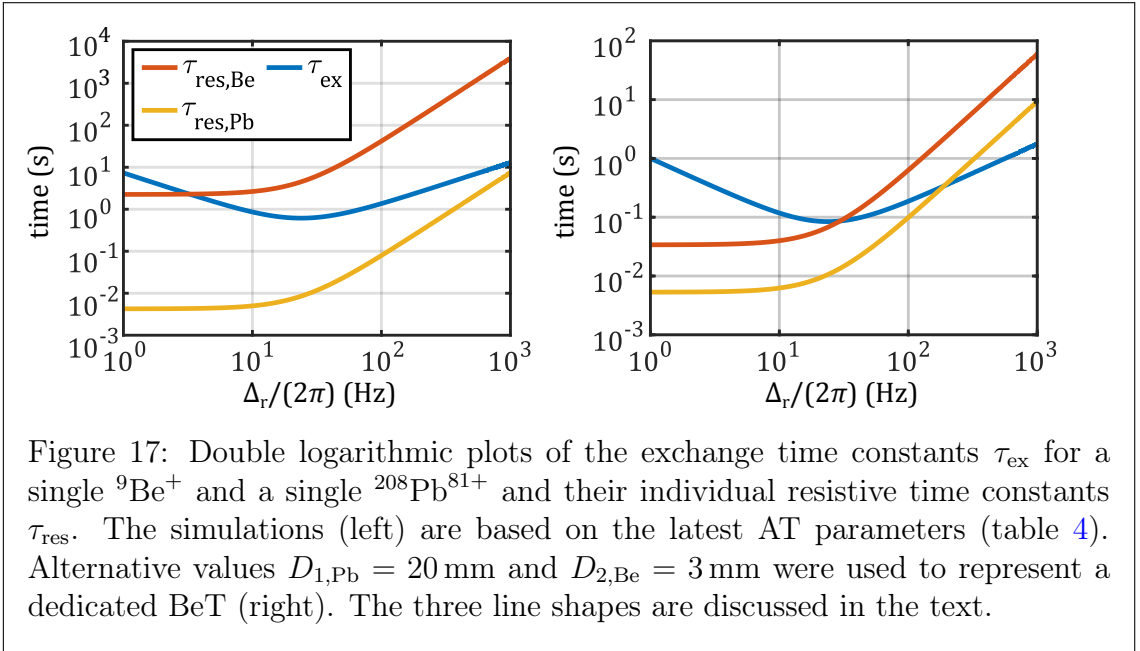
For the perfectly coupled case and if we include N_1, N_2 , our *exchange time* constant becomes identical to the time constant expressed in (39) by Heinzen and Wineland:

$$\tau_{\text{ex}}(\tilde{\omega}_0, \delta = 0) = \frac{\pi \tilde{\omega}_0 D_1 D_2 \sqrt{m_1 m_2}}{q_1 q_2 \sqrt{N_1 N_2}} C_{\text{eff}}. \quad (47)$$

In conclusion, the resonator features similar coupling to eq. (39) with the great advantage that we can control and tune the effective parallel trap capacitance $C_{\text{eff}}(\omega)$ by choosing different coupling positions $\tilde{\omega}_0$.

5.3.1 Tuning C_{eff}

The fundamental idea is to bring the axial coupling frequency $\tilde{\omega}_0$ to a position where $C_{\text{eff}}(\omega)$ translates into a small τ_{ex} , while at the same time the resonator interaction τ_{res} from eq. (25) for each ion is small. Before I explain the latter compromise let me plot the general dependency of $C_{\text{eff}}(\omega)$ in figure 16 for the AT resonator setup (see caption). At $\omega \approx 2\pi \times 24 \text{ Hz}$ a minimal value of $C_{\text{eff}} \approx 6 \times 10^{-3} \text{ pF}$ can be achieved. Compared to the original parallel AT trap capacitance $C_p \approx 21.5 \text{ pF}$ this



corresponds to a principal improvement of τ_{ex} by a factor of $C_p/C_{\text{eff}} \sim 3500$. For very large detuning C_{eff} converges back to $C_{\text{eff}} \xrightarrow{\omega_0 \gg \omega_r} C_p$. I must point out two things here. First, C_p will readjust when a second trap is connected to the resonator. We can estimate it upon measuring the corresponding resonator parameters (Q, ω_r, R_p) .³³ This effect will be small though, because the main contribution to C_p is typically provided by the resonator itself. Second and more importantly, though τ_{ex} can be reduced by a significant amount, this does not mean efficient cooling. The coupling of the ions with the resonator at 4 K have to be taken into account here as well. If I consider a thermalized HCI coupled to a laser-cooled beryllium ion, upon cooling the HCI below the resonator bath temperature, the resonator will immediately act as a heating source to the HCI with the resonator time constant τ_{res} according to eq. (25). Of course, the same holds for the beryllium ion which is laser cooled to the Doppler temperature $T_D = 0.5$ mK. In figure 17 I plot as an extreme example the exchange time $\tau_{\text{ex}}(\omega)$ between a single ${}^9\text{Be}^+$ and hydrogenlike ${}^{208}\text{Pb}^{81+}$, and compare it to their individual $\tau_{\text{res,Be}}$ and $\tau_{\text{res,Pb}}$ resonator time constants.³⁴ The two plots differ only in the trap setup (see caption): (left) I use the effective electrode distances from our latest measurement, (right) I use a small D_{eff} to represent a dedicated beryllium trap setup. A sub-second τ_{ex} would be possible for our current trap setup in the $\Delta_r \sim 2\pi \times 10$ Hz regime, but the heating of the resonator dominates the energy exchange. The HCI features a strong ion-ion coupling but also brings along an unfavorable strong coupling to the resonator. However, with the dedicated beryllium trap the ion-ion coupling dominates already at $\Delta_r \gtrsim 2\pi \cdot 100$ Hz. According to figure 16 still a thousandfold improvement of C_{eff} and τ_{ex} is possible at that detuning. This shows the great conditions and

³³I re-estimate C_p this way in section 5.4.2.

³⁴When the ions are coupled, the resistive heating/cooling of the ions is strictly speaking a combination of the ion's individual τ_{res} . I still plot them individually for a reference scale.

possibilities our sympathetic cooling technique can offer in principle.

An experimental operation scheme to cool the HCI, similar to the technique described in [14], could be based on the steps:

1. Laser is off, move both ions together to the coupling position $\tilde{\omega}_0$ and wait for the voltage source to thermalize.
2. At this coupling position laser cool the beryllium ion or cloud for τ_D down to T_D to initialize the coupling ($\tau_D \ll \tau_{\text{ex}}$).
3. Wait for one τ_{ex} and repeat step 2 to re-initialize the coupling.
4. When the HCI is sufficiently cooled separate the ions ($\tilde{\omega}_{z,1} \neq \tilde{\omega}_{z,2}$) and move them away from the resonator to suppress heating.

During step 2 the HCI will exchange energy with the beryllium. But because of the resonator heating and ion jitter, the energy cannot be transferred completely. Thus, the cooling cycle needs to be repeated (purpose of step 3). Also, during coupling the laser cooling should be turned off as it would suppress the coupling. The beryllium is effectively fixed in position by the strong laser cooling and cannot induce a current into the resonator effectively.

5.3.2 Avoided Crossing Line Shape

So far I have looked at time dynamics of the ion-ion coupling and derived the time constant τ_{ex} for one π -pulse. On the other hand though, focusing on the energy/frequency behavior, two coupled oscillators show a very prominent avoided crossing behavior of their mode energies [38]. The new time-independent orthogonal modes of the coupled axial system (analogous to the double dip in section 2.5.2) oscillate with

$$\Omega_{\pm} = \tilde{\omega}_0 + \frac{\delta}{2} \pm \frac{\tilde{\Omega}_G}{2} = \tilde{\omega}_0 + \frac{1}{2} \left(\delta \pm \sqrt{\delta^2 + \Omega_G^2} \right). \quad (48)$$

The two modes are split by $\Omega_+ - \Omega_- = \tilde{\Omega}_G$. Minimal splitting (or strongest coupling) is achieved at zero detuning, where $\tilde{\Omega}_G \rightarrow \Omega_R$. Now consider ion 1 to be fixed at $\tilde{\omega}_{z,1}$ and ion 2 driven with $\tilde{\omega}_{z,2} = \tilde{\omega}_{z,1} + \delta$ in such a way that the detuning δ increases linearly. Sweeping from negative to positive detuning, the signal of ion 2 would cross the signal of ion 1 on the resonator. But instead, within the regime of small δ , the two axial modes of the ions couple and form the orthogonal modes. No signal crossing occurs due to the non-zero splitting of Ω_+ and Ω_- . The transition from original modes to orthogonal modes is continuous. This is called an *avoided crossing* and appears for any two coupled oscillators.

We are able to simulate the avoided crossing we would produce with our trap setup parameters. For this I treat the two ions and the resonator in the equivalent circuit

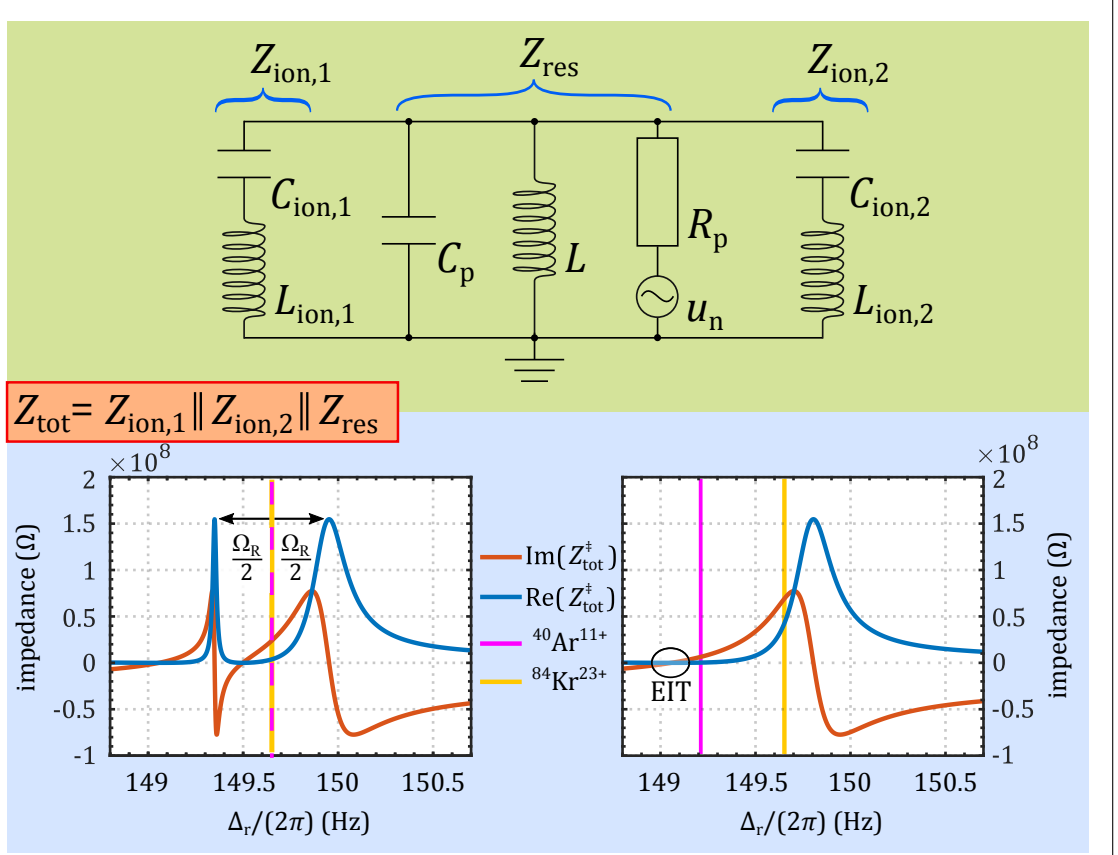


Figure 18: The equivalent circuit of the detection system interacting with two separated ions is shown in the green area. Each ion interacts with the images charges of both ions. This is an extension to 6. The plots of the simulated $Z_{\text{tot}}^{\ddagger}$ are shown in the blue area. The simulations are based on our measurement setup (see table 4 for the corresponding trap values) storing a single $^{84}\text{Kr}^{23+}$ and a $^{40}\text{Ar}^{11+}$ in the two traps. $Z_{\text{tot}}^{\ddagger}$ is plotted for two scenarios with the krypton ion being fixed at $\Delta \approx 2\pi \times 150$ Hz but a different δ in both cases: (left) the strongest coupling position $\delta = 0$ Hz and (right) EIT position $\omega_{\text{Kr}} = \omega_{\text{Ar}}$. In both plots the positions of the pushed frequencies $\tilde{\omega}_{\text{Kr}}$ and $\tilde{\omega}_{\text{Ar}}$ are indicated as the vertical green and pink lines (they overlap in the left plot). While only the blue line shape $\text{Re}(Z_{\text{tot}}^{\ddagger})$ of a thermalized ion is physically detectable, the nodes of the red line shape $\text{Im}(Z_{\text{tot}}^{\ddagger})$ reveal turning points of the impedance. Nodes that feature a sign change from $(- \rightarrow +)$ denote a shortening of the circuit and thus reveal the original frequencies ω_{Kr} and ω_{Ar} (the nodes overlap in the right plot).

model (see figure 18), and study the total impedance Z_{tot}^\dagger of the circuit:

$$Z_{\text{tot}}^\dagger \equiv \underbrace{Z_{\text{ion},1} \parallel Z_{\text{ion},2}}_{Z_{\text{ions}}} \parallel Z_{\text{res}} = \frac{Z_{\text{res}} Z_{\text{ions}}}{Z_{\text{res}} + Z_{\text{ions}}} \quad \text{with} \quad Z_{\text{ions}} = \frac{Z_{\text{ion},1} Z_{\text{ion},2}}{Z_{\text{ion},1} + Z_{\text{ion},2}}. \quad (49)$$

But before I proceed with the avoided crossing emerging from Z_{tot}^\dagger , it is helpful to understand its line shape first. In figure 18 two prominent scenarios for Z_{tot}^\dagger are plotted that represent two different frequency setups of the coupled ions. Without loss of generality I chose $^{84}\text{Kr}^{23+}$ as ion 1 and $^{40}\text{Ar}^{11+}$ as ion 2, since those were later used in our measurements. While the frequency position of ion 1 is identical in both plots, ion 2 is initialized with different δ . The blue and red curves show the real and complex part of Z_{tot}^\dagger for the respective ion setup. The yellow and pink vertical lines indicate $\tilde{\omega}_{z,1}$ and $\tilde{\omega}_{z,2}$ for the individual ions. They are derived by peak detection of Z_{tot} and therefore do not include the ion-ion coupling. This serves as a reference to see at what frequencies the individual ions would actually oscillate. Nodes of $\text{Im}(Z_{\text{tot}}^\dagger)$ with a sign change ($- \rightarrow +$) always denote the original ion frequencies (see section 2.4.3).

The first scenario (left) shows the strongest coupling position where the ion's pushed frequencies overlap perfectly ($\tilde{\omega}_{z,1} = \tilde{\omega}_{z,2}$) and $\text{Re}(Z_{\text{tot}}^\dagger)$ features the two dispersive signals of the orthogonal modes with minimal splitting of Ω_{R} . In this thesis these modes are termed *common* mode u and *counter* mode v to insinuate the induced currents of the two ions in the resonator to be in phase or out of phase, respectively (see appendix D for quantitative details). With a Gedankenexperiment based on the retroactive force from eq. (22) I can assign the modes to their dispersive signals: an induced current exerts a force on the ion which e.g. led to the resonator pushing effect in section 2.4.3. If two induced currents are in phase, they add up constructively and the frequency pushing effect becomes even larger. Therefore, the dispersive signal that spans over a broader dip-to-peak range must be the common mode. For out of phase currents the pushing effect decreases. An alternative point of view is to consider the retroactive forces induced by one ion on the respective other ion. In phase currents have an accelerating impact and shift the common mode to a higher frequency while out of phase currents decelerate the counter mode oscillation to lower frequencies.

In the second plot the other extreme scenario is presented (right). When the original frequencies overlap ($\omega_{z,1} = \omega_{z,2}$) the retroactive forces produced by the currents induced by the counter mode cancel.³⁵ This means that the counter mode experiences no frequency pushing and rather oscillates at the original ion frequency which shortens the circuit ($Z_{\text{tot}}^\dagger \rightarrow 0$, analogous to section 2.4.3). Therefore, the counter mode vanishes and effectively decouples from the resonator. This behavior is similar to electrically induced transparency (EIT) [73].

Interestingly, for the same ion species and equal trap properties for both traps, the

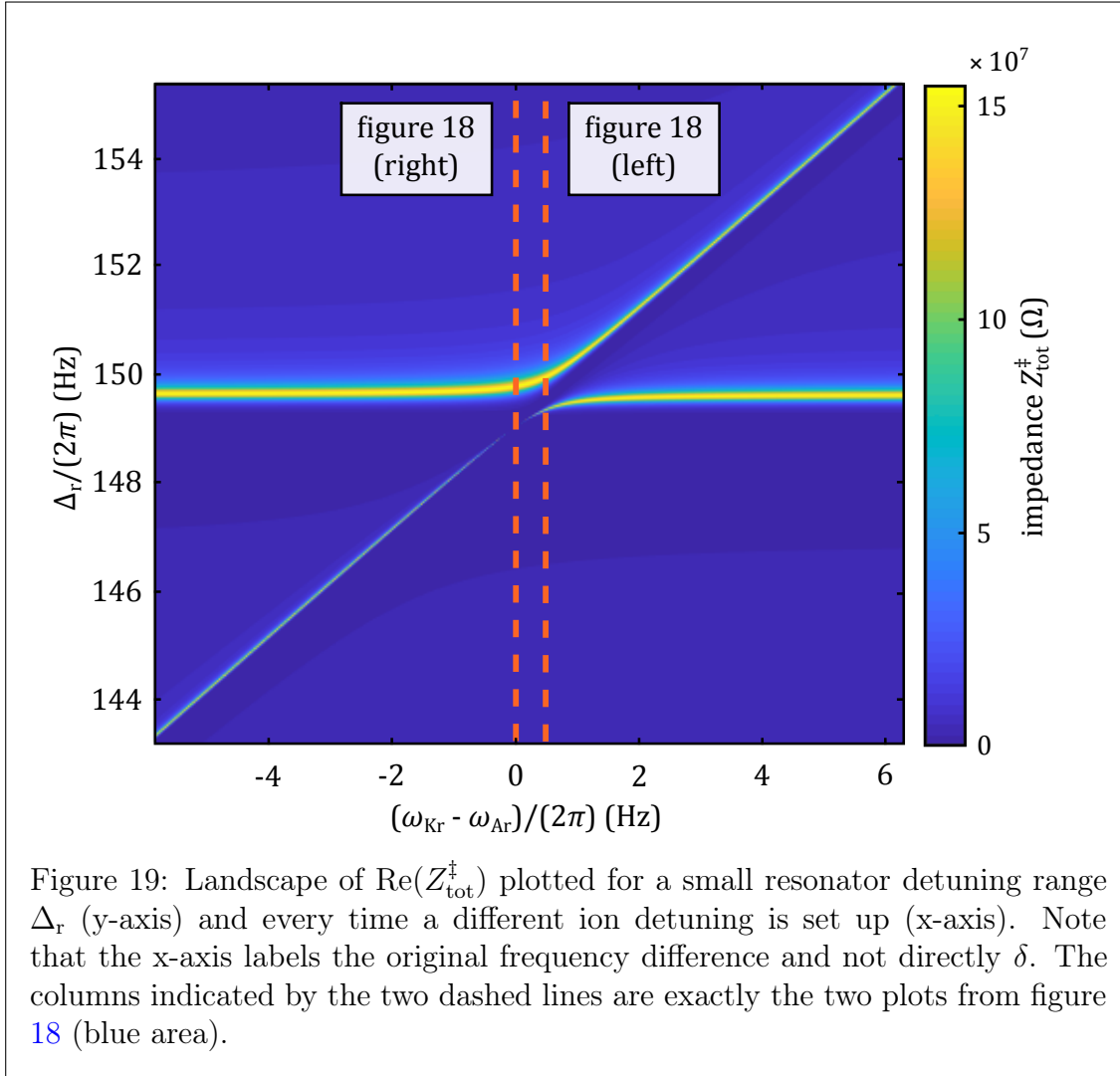
³⁵The overall current itself, induced by the counter mode, however is only zero in the special case of $\frac{q_1}{D_1 \sqrt{m_1}} = \frac{q_2}{D_2 \sqrt{m_2}}$.

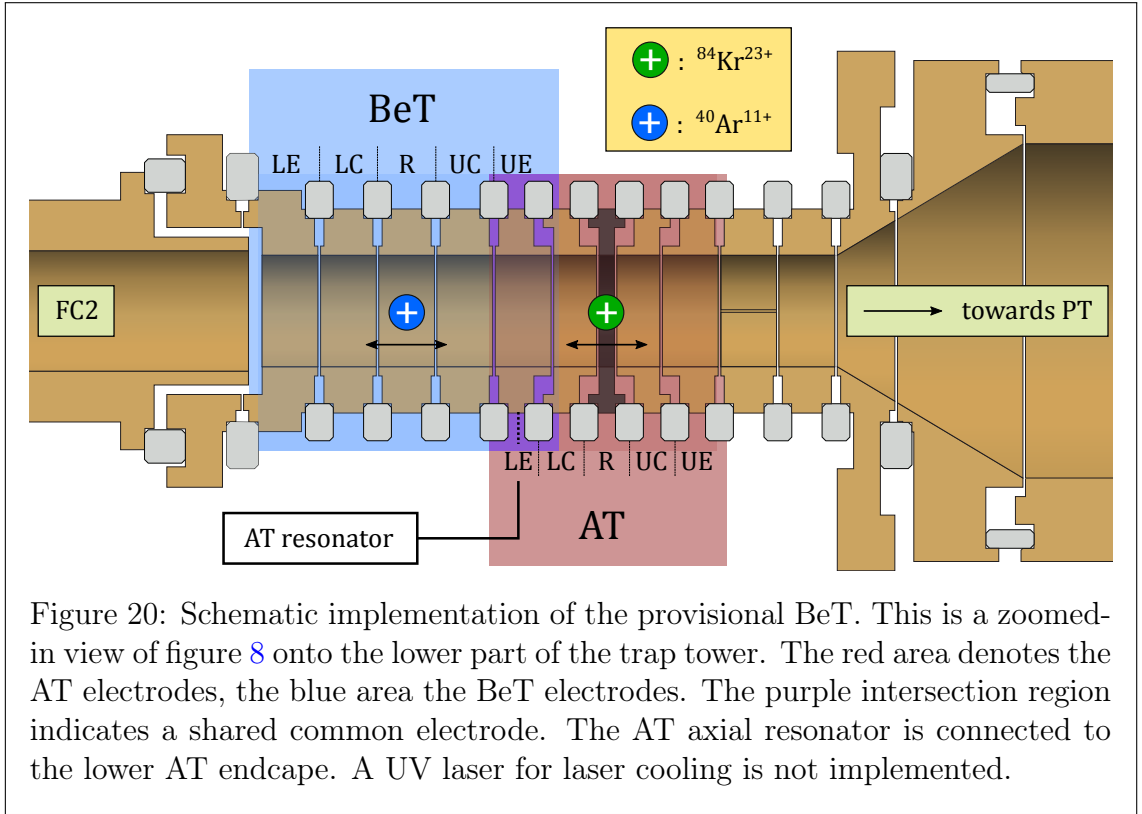
EIT point is exactly at the perfect coupling position because the transparency demands $\omega_{z,1} = \omega_{z,2}$ and the frequency pushing is equally large for identical ions.

Now I proceed with the avoided crossing landscape. I simulate the line shape of $\text{Re}(Z_{\text{tot}}^\ddagger)$ multiple times for a fixed $^{84}\text{Kr}^{23+}$ and a linearly swept $^{40}\text{Ar}^{11+}$. I arrange the acquired line shapes from negative to positive detuning as data columns in a matrix. The landscape of this matrix is plotted in figure 19. Vertical columns of this landscape probe $\text{Re}(Z_{\text{tot}}^\ddagger)$ for a given ion detuning δ (x-axis) within a small frequency range on the resonator flank (y-axis). As an example the dashed orange lines indicate the columns that represent exactly the two plotted scenarios from figure 18 (blue area).

This impedance landscape reveals the sought after avoided crossing line shape of the signal peaks. Depending on the ion species and trap parameters the minimal splitting becomes larger/smaller and additionally the EIT position changes. In the non-coupled case we expect a linear crossing of the signal peaks. The transition from the ion individual modes to the orthogonal modes is continuous.

I should point out here that the simulations of Z_{tot}^\ddagger automatically include all the damping effects of R_{eff} , which we neglected in the analytical derivation in (44) before.





5.4 The Proof of Coupling Measurement

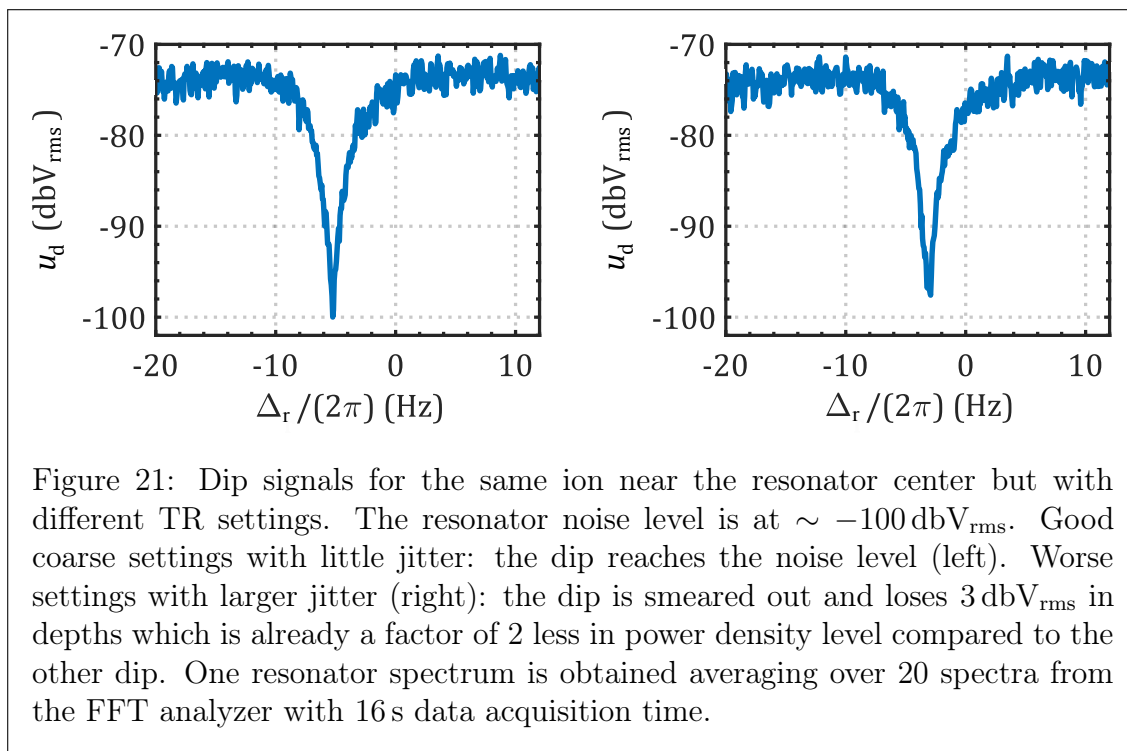
So far I have derived a theoretical description for an alternative coupling scheme with exchange time constant τ_{ex} . Simulations show the avoided crossing pattern in figure 19, which predicts the voltage signal of the common and counter modes of the coupled system. If we can reproduce that pattern with experimental data, this would be an irrevocably proof that coupling between the two ions occurs. We aim to perform a proof of principle measurement that shows ion-ion coupling whose experimental data can be described with our theory.

To this end, from a stack of unengaged electrodes we prepare a provisional third trap (beside the PT and AT) that has a connection to the same resonator as the AT to perform such measurements.

5.4.1 Preparation of the Beryllium Trap - BeT

Since no dedicated beryllium trap has been installed yet at ALPHATRAP and laser cooling will not be required in our proof of principle measurements, we used spare electrodes below the AT as a substitution (see figure 20). This stack of electrodes (BeT)³⁶ was never envisaged for measurement trap operation, thus the voltage settings for these electrodes had to be significantly optimized. After ion injection from the HC-EBIT [47] we ended up with the similar charge-to-mass ratio species $^{84}\text{Kr}^{23+}$ in the AT and $^{40}\text{Ar}^{11+}$ in the BeT.

³⁶The BeT here is not to be confused with the BeT setup in [7].



We operated the BeT with asymmetric tuning ratios to move the trapping well with the ion $\sim 1.5 \text{ mm}$ closer towards the resonator in order to reduce D_{eff} and improve the detected dip width. Unfortunately this trap asymmetry facilitates odd order field imperfections that need to be compensated. In principle, the two different TR for the upper and lower correction electrodes allow a C_4 and C_3 compensation.

We did the optimization process in two steps. First, we compared the depths of an ion dip for different TR settings: the jitter smears out the tip of the dip during the spectrum acquisition which then reaches less down to the noise level (see figure 21). In a better compensated trap higher order field imperfections are more suppressed and the ion frequency is less prone to energy fluctuations. Therefore, we probe the TR for deep ion dips.

Then in a subsequent fine tuning step, starting from the coarse settings, we observed the thermalization process of an excited ion signal. We perform the observation on the flank of the resonator where the thermalization process is slowed down. After a dipolar excitation pulse, the enlarged peak signal shrinks/cool down to its previous thermalized signal shape. This should happen without any frequency drift because ideally no field imperfections are present. The thermalization pattern is probed for small variation steps of the two TRs to spot the setting for a minimal frequency drift where C_3 cancels roughly C_4 .³⁷

Last but not least the two traps are spatially so close together that their voltage settings affect each other: whenever we change voltages of one trap for e.g. moving the ion frequency along the resonator, we also have to adjust the voltages in the

³⁷We only set the trap in a way that the axial motion shows minimal frequency shifts. This does not mean we found the settings for compensated $C_3 = C_4 = 0$ which would additionally suppress frequency shifts of the radial modes.

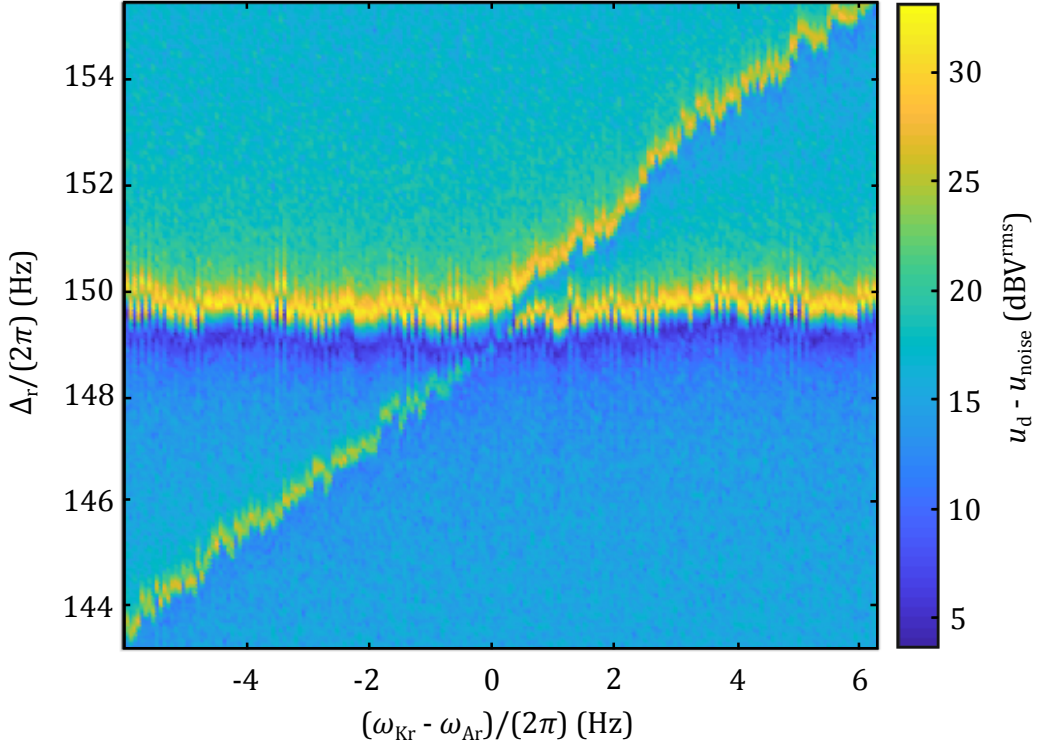


Figure 22: The 201 obtained spectra are layered along the x-axis to form this measurement landscape. Each vertical column represents exactly one of the obtained spectra. The chart is build up analogously to figure 19 except the detected voltage is represented instead of $Z_{\text{tot}}^{\ddagger}$. The apparent pixelated chart background is caused by the resonator noise floor in each spectrum. More details are given in the text.

other trap to compensate the penetrating electric field in it. This effect is fortunately linear to first order within the parallel plate capacitor picture introduced in section 2.4.1.

5.4.2 Avoided Crossing Measurement

After the BeT had been set up, optimized to our best effort and compensated against each other's field, we set the AT ion to a fixed $\Delta_r \approx 2\pi \times 150$ Hz resonator detuning with $\omega_{z,1} \approx 2\pi \times 334\,360$ Hz and the BeT ion frequency to range from approximately $-2\pi \times 6$ Hz $< \delta < 2\pi \times 6$ Hz within 201 steps. During each step one resonator spectrum is acquired, producing a total of 201 spectra. Layering them from negative to positive δ analogous to figure 19 yields the landscape in figure 22. The pattern of the measured spectra looks already at first glance by eye similar to the previous simulation.

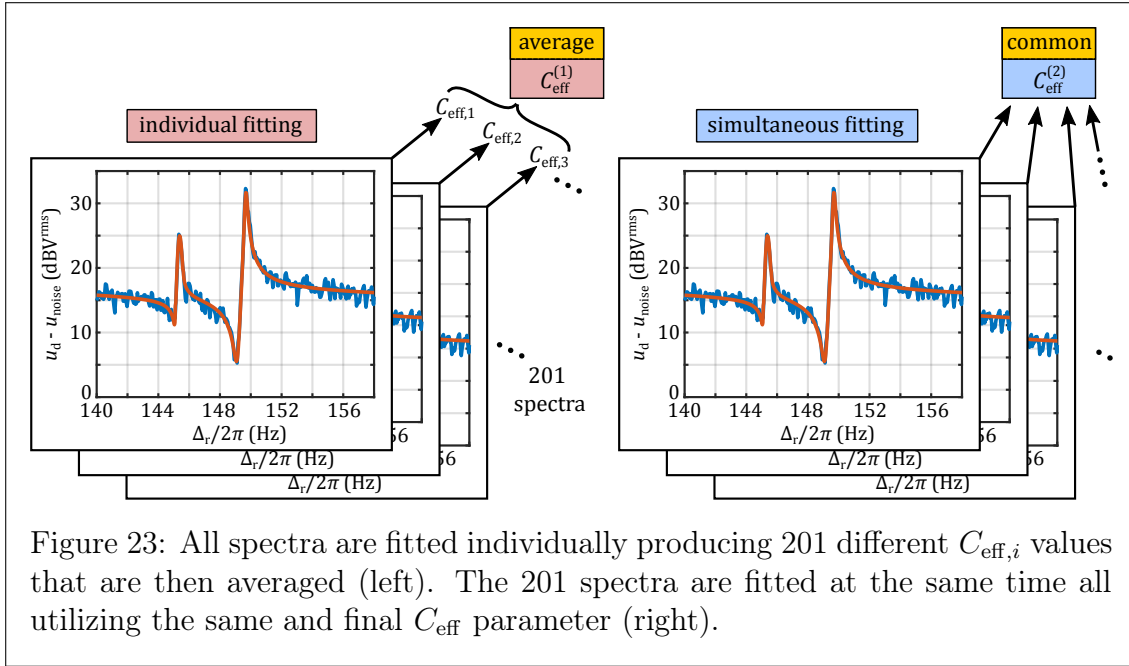


Figure 23: All spectra are fitted individually producing 201 different $C_{\text{eff},i}$ values that are then averaged (left). The 201 spectra are fitted at the same time all utilizing the same and final C_{eff} parameter (right).

Qualitatively, the experimental data clearly reveal an avoided crossing pattern and also feature the EIT as discussed for the simulation. The prominent frequency jumps in the AT line are caused by rounding of the voltage source. The voltage step size to compensate the AT against the gradually increasing BeT voltage is actually smaller than the precision of the voltage source (UM1-14 [74]). The compensation voltages are therefore adjusted down or up by the voltage source which lead to this *bin jumping* like behavior. The smoother frequency fluctuation is caused by voltage source instability and additionally by trap imperfections for the BeT line.

The goal is to extract a value for C_{eff} as it allows us to estimate Ω_R and τ_{ex} for given ion and trap parameters according to eq. (45) and (46). I quantify C_{eff} with two different methods. Each experimental spectrum is fitted via the MATLAB `lsqnonlin`-function with eq. (21b) as the fit model except and $Z \rightarrow Z_{\text{tot}}^\dagger$. However, before I can address C_{eff} as the determining fit parameter, I need to fix several variables in advance in different pre-fits. I give a short rundown of these steps in the following but more technical details and results are covered in appendix C.

1. First, D_{eff} needs to be determined for both traps. $D_{\text{eff,AT}}$ has been calculated before in [18] however, since the trapping potentials of the AT and BeT are significantly affect each other, the axial trapping positions are pulled towards the resonator reducing D_{eff} .
2. Then I must characterize the resonator noise. The resonator itself is fully described by the set of variables (ω_r, Q, \tilde{A}) and any possible detection effect is accounted by $(\tilde{u}_{\text{en}}, \kappa)$. We assume that the resonator properties do not vary over the course of the measurement run so that we can model and separate the Z_{res} part for all fits.

Table 4: This table lists the values of the essential fixed parameters during all four fitting stages. No mean value for the frequencies ($\omega_{\text{AT}}, \omega_{\text{BeT}}, \sigma$) are given due to the fitting procedure of stage 4. The first brackets of all parameters denote the 1σ parameter confidence interval (estimated via the MATLAB nliparci-function) and all necessary error propagation from previous fixed parameters. The second bracket is the statistical error of the mean. See appendix C for more details and the complete derivation of the fixed parameter values.

Parameter	unit	Fixed Value
$D_{\text{eff,AT}}$	mm	17.97(13)(1)
$D_{\text{eff,BeT}}$	mm	24.45(27)(3)
Q		7016(34)(3)
\tilde{A}	V _{rms}	1455(12)(1)
ω_{r}	$2\pi \times \text{Hz}$	334 210.60(11)(1)
u_{en}	V _{rms}	1.885(4)
\tilde{K}_{det}	V _{rms} s	$-8(20)(2) \times 10^{-7}$
σ	$2\pi \times \text{Hz}$	(8)
ω_{AT}	$2\pi \times \text{Hz}$	(13)
ω_{BeT}	$2\pi \times \text{Hz}$	(15)
$C_{\text{eff}}^{(1)}$	10^{-14}F	1.994(35)(2)
$C_{\text{eff}}^{(2)}$	10^{-14}F	1.989(26)

3. In a third step I obtain the frequency settings for every single spectrum and individually pass them to step 4. I consider the parameters ($\omega_{\text{AT}}, \omega_{\text{BeT}}, \sigma$). The first two are the original ion frequencies and σ describes the frequency jitter of the BeT ion. The jitter can be modeled by a Gaussian distribution of width σ around the mean ω_{BeT} . This jitter fitting procedure improves the fitting tremendously.
4. After all the essential variables have been assigned a fixed value by describing Z_{res} via a RLC-circuit, I instead separate it now into $Z_{R_{\text{eff}}}$ and $Z_{C_{\text{eff}}}$ and implement C_{eff} as a variable into the complex part (see section 5.2). The fit model is then fully described by only C_{eff} . The difference in the two methods are that the first one fits C_{eff} for each spectrum individually, which is then averaged to $C_{\text{eff}}^{(1)}$, while the second one fits each spectrum simultaneously with only one common $C_{\text{eff}}^{(2)}$ parameter. Figure 23 gives an idea of the two schemes: (left) is the individual and (right) the simultaneous fitting.

Table 4 lists the results for $C_{\text{eff}}^{(2)}$, $C_{\text{eff}}^{(1)}$ and the current trap parameters. The error budget is explained in the caption. Statistical errors, if any, are dominated by the parameter fitting uncertainty in all cases. $C_{\text{eff}}^{(1)}$ and $C_{\text{eff}}^{(2)}$ deviate $\sim 0.3\%$ from each other, which is well within the range of their relative errors of $\delta C_{\text{eff}}^{(1)}/C_{\text{eff}}^{(1)} = 1.8\%$

Table 5: Simulated and measured results are listed. Initial parameter uncertainties to simulate $\tau_{\text{ex}}^{\text{sim}}$ are negligible. Because I estimated $C_{\text{eff}}^{\text{sim}}$, its error is due to Gaussian error propagation of the D_{eff} uncertainties. For $\tau_{\text{ex}}^{\text{meas}}$ the errors are calculated via error propagation as well. No statistical error propagation was given because they were either negligible compared to their 1σ parameter uncertainty (in the case of both D_{eff}) or the error propagation itself could be neglected completely (in the case of ω_{AT}). The leading error is given by $C_{\text{eff-nliparci}}$.

	$C_{\text{eff}}/10^{-14}\text{ F}$	$\Omega_{\text{R}}/(2\pi\times\text{Hz})$	$\tau_{\text{ex}}/\text{s}$
simulation	1.958(25)	0.59	0.841
measurement	1.989(26)	0.58(1)	0.856(16)

and $\delta C_{\text{eff}}^{(2)}/C_{\text{eff}}^{(2)} = 1.3\%$. This makes a distinction between the two results redundant. I choose the more precise value $C_{\text{eff}}^{(2)}$ as the representative effective capacitance of our measurement. The smaller overall error of $C_{\text{eff}}^{(2)}$ compared to $C_{\text{eff}}^{(1)}$ is due to a smaller parameter confidence interval (see table 9). This is because the simultaneous fitting routine provides a larger spectrum of meaningful residuals available to minimize (better statistics), whereas the individual fitting routine relies only on the residuals of one individual spectrum at a time. With the determined ω_{r} for the present trap setup we can estimate the parallel AT trap capacitance to be $C_{\text{p}} = L^{-1}\omega_{\text{r}}^{-2} \approx 21.6\text{ pF}$, if we assume $L = 10.5\text{ mH}$ has not changed since its quantification in [18]. Our measurement shows an effective reduction of the parallel trap capacitance by a factor of ~ 1100 . Remarkably, our $D_{\text{eff,AT}}$ value deviates by 9σ from the value estimated in [18] as a result of the altered ion position caused by the BeT trapping potential described in fitting step 1.

I can now calculate the experimental values for τ_{ex} and Ω_{R} and compare them with the simulated ones. The results are given in table 5.

The estimation of $\tau_{\text{ex}}^{\text{sim}}$ is straightforward: I simulate the $Z_{\text{tot}}^{\ddagger}$ line shape with the newly calculated resonator parameters and read out the minimal splitting of the common and counter mode (which is directly Ω_{R}) and the coupling position $\tilde{\omega}_0^{\text{sim}}$ both with negligible small error. This allows me to calculate back to the corresponding $\tau_{\text{ex}}^{\text{sim}}$ and then $C_{\text{eff}}^{\text{sim}}$ via eq. (46) and (47). For the experimental value of τ_{ex} it is done the other way around: we have measured C_{eff} and calculate τ_{ex} via (47). I just miss a quantification of the experimental overlap frequency $\tilde{\omega}_0$. However, one measurement condition was the fixation of the AT ion frequency. Therefore, I assume that the coupling must have happened at $\tilde{\omega}_0 = \tilde{\omega}_{\text{AT}}$. To this end, I average all obtained ω_{AT} from fitting stage 3 and calculate $\tilde{\omega}_{\text{AT}}$ via its definition in eq. (44). I end up with $\omega_{\text{AT}} = 2\pi \times 334\,359.66(13)(13)\text{Hz}$ and $\tilde{\omega}_0 = 2\pi \times 334\,360.24(13)(13)\text{Hz}$.³⁸ Unfortunately the bin jumping of the AT frequency gives rise to a relatively large statistical error (second bracket). The absolute deviation $\tilde{\omega}_0^{\text{sim}} - \tilde{\omega}_0 = 2\pi \times 0.07\text{ Hz}$

³⁸The uncertainty $\Delta\omega_{\text{AT}}$ in the error budget of $\tilde{\omega}_0$ dominates other contributions. The errors of ω_{AT} and $\tilde{\omega}_0$ therefore happen to be identical.

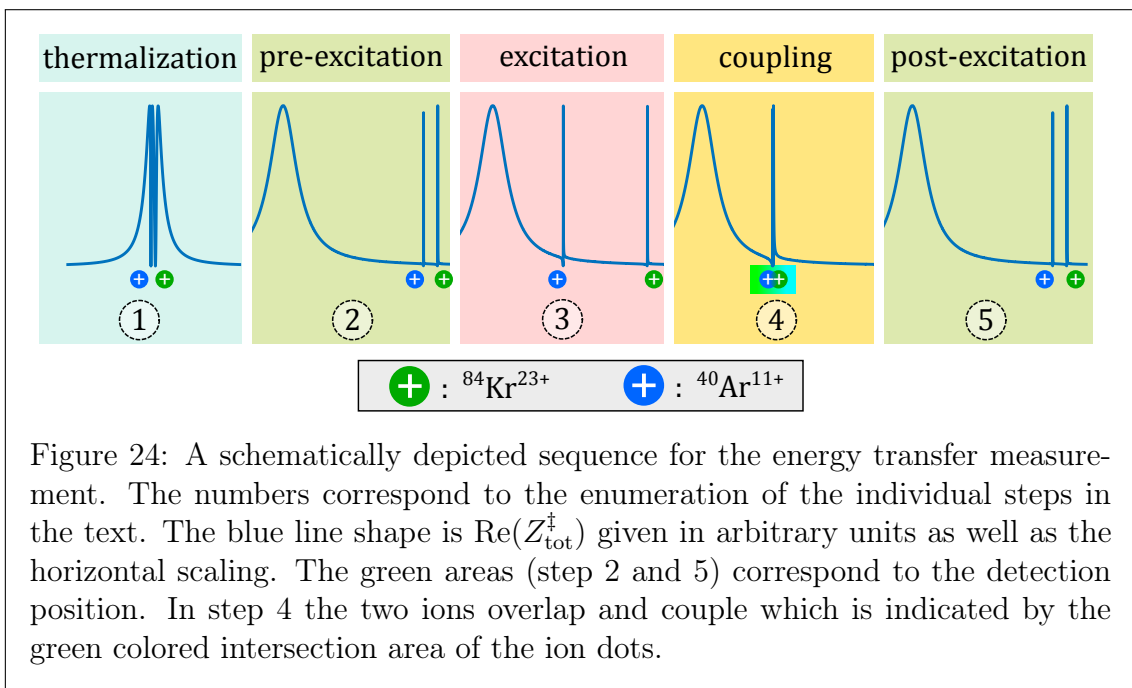


Figure 24: A schematically depicted sequence for the energy transfer measurement. The numbers correspond to the enumeration of the individual steps in the text. The blue line shape is $\text{Re}(Z_{\text{tot}}^{\dagger})$ given in arbitrary units as well as the horizontal scaling. The green areas (step 2 and 5) correspond to the detection position. In step 4 the two ions overlap and couple which is indicated by the green colored intersection area of the ion dots.

is well within the 1σ range.

The measurement is in good agreement with the simulation. Measured and simulated C_{eff} deviate by 0.9σ considering their combined errors and τ_{ex} deviates by 0.9σ from the simulation which confirms reliance on our C_{eff} fit model and the algorithm itself. This is additionally supported by the redundant initial difference between the two fitting routines at this level of precision. For the fitting algorithm we used the approximation $C_{\text{eff}}^c(\omega_{z,1}, \omega_{z,2}) \approx C_{\text{eff}}$ at small δ (see section 5.3) in the fit model. This leads to a deviation to C_{eff}^c of roughly 0.5% for some Hz detuning.³⁹ The effect is approximately linear in δ . The deviation is in fact in the order of the measured C_{eff} error. However, the measurement was executed with good δ symmetry meaning that the amount of data featuring negative detuning (C_{eff} is underestimated) is roughly equal to the amount of data featuring positive detuning (C_{eff} is overestimated). Therefore, I expect the effect of the deviation to be strongly suppressed and I do not take it into account further.

5.4.3 Energy Transfer Measurement

Apart from the avoided crossing measurement we aim to experimentally demonstrate direct energy transfer between the two coupled ions. The idea is to have an excited ion transfer its energy to a thermalized ion back and forth in Rabi cycles.

Our measurement procedure is the following (see figure 24):

1. First, both ions are thermalized at the resonator center to 4 K.

³⁹Because we set the AT ion position as the coupling position in this measurement ($C_{\text{eff,AT}} = C_{\text{eff}}$), we can write $\frac{C_{\text{eff}}^c - C_{\text{eff}}}{C_{\text{eff}}^c} = 1 - \frac{C_{\text{eff}}}{\sqrt{C_{\text{eff,AT}} C_{\text{eff,BeT}}}} = 1 - \sqrt{\frac{C_{\text{eff,AT}}}{C_{\text{eff,BeT}}}} \approx 0.5\%$

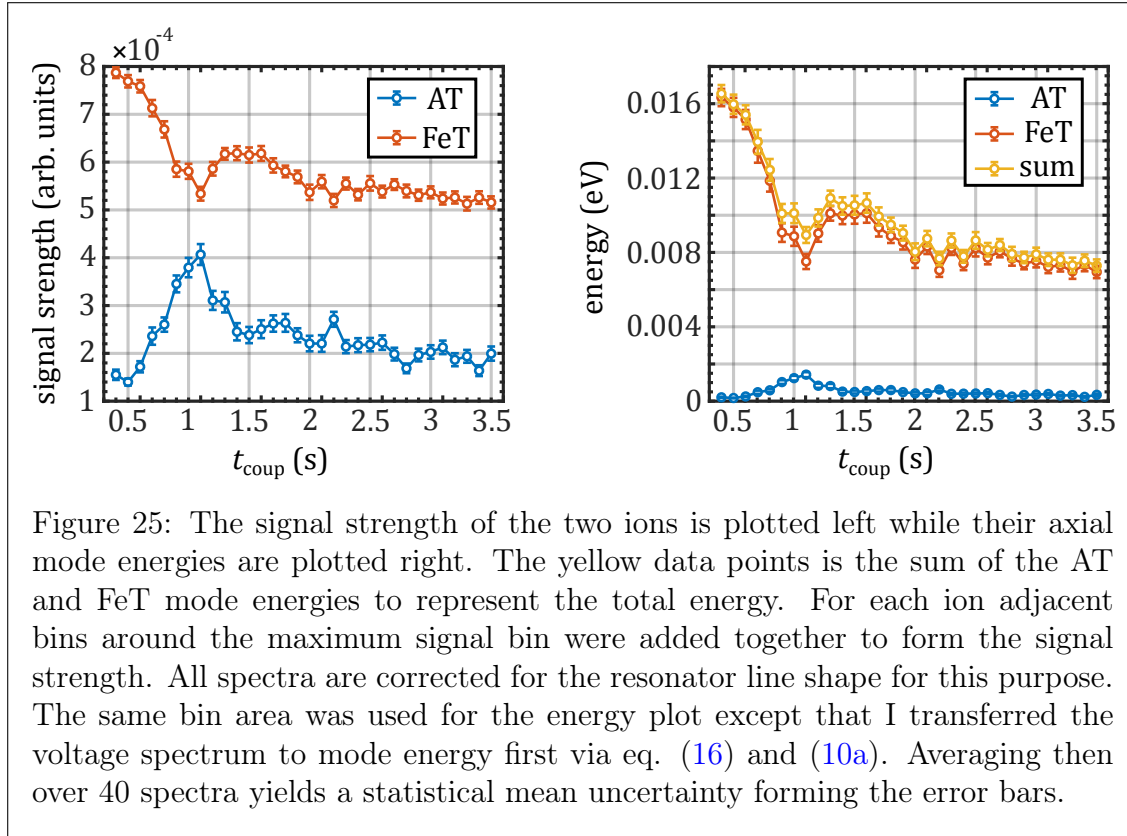


Figure 25: The signal strength of the two ions is plotted left while their axial mode energies are plotted right. The yellow data points is the sum of the AT and FeT mode energies to represent the total energy. For each ion adjacent bins around the maximum signal bin were added together to form the signal strength. All spectra are corrected for the resonator line shape for this purpose. The same bin area was used for the energy plot except that I transferred the voltage spectrum to mode energy first via eq. (16) and (10a). Averaging then over 40 spectra yields a statistical mean uncertainty forming the error bars.

2. The cold ions are moved far off the resonator center $\Delta_{r,AT} \approx 500$ Hz and $\Delta_{r,BeT} \approx 400$ Hz to suppress resistive coupling or ion coupling. This position marks our *detection position* at which we now acquire a pre-excitation spectrum for reference.
3. Now one ion is excited. To ensure excitation of only the BeT ion, the AT ion is detuned further to $\delta > 1$ kHz (this depends on the excitation burst length).
4. To enable coupling and energy transfer we move the AT ion directly on top of the BeT ion with $\tilde{\omega}_{AT} \approx \tilde{\omega}_{BeT}$. The coupling takes place at roughly $\Delta_r \sim 2\pi \times 160$ Hz resonator detuning..
5. After a specific coupling time t_{coupl} we separate the ions and move them back to the detection position to acquire post-excitation spectrum proofing energy transfer.

We repeat this cycle several times which allows us to average the pre- and post-excitation spectra. The coupling time ranges between $0.4 \text{ s} \leq t_{coupl} \leq 3.5 \text{ s}$ in steps of 0.1 s. From the spectra I can extract the induced rms-currents i_{ind}^{rms} of the ions and from there their axial amplitude and energy. Since our impedance line shape model does not describe excited ions but only thermalized ones, we cannot apply the model for any fitting analysis. We solely rely on the frequency bin width resolution of our FFT analyzer and add up adjacent frequency bins of the peak signals to cover the total signal strength.

In figure 25 the ion's signal strength and their mode energies are plotted against t_{coup} . A clear transfer in signal strength and energy can be recognized at least for the first π -pulse with an exchange time of about $\tau_{\text{ex}} \sim 0.6$ s. The coupling and energy transfer starts only at $t_{\text{coup}} \sim 0.5$ s and not at time zero, that is why we omitted lower coupling times here. The reason for the coupling delay is most likely due to the thermalization of the UM1-14 voltage source after any voltage settings are changed. During this process the ion frequencies, driven by the drifting voltage, converge towards the coupling position and energy transfer can effectively begin. We could circumvent this problem by the implementation of an external switch such that the UM1-14 does not need to change the supply voltage. Moreover, the signal/energy transfer appears to be incomplete. A first reason is, that the coupling position is not exactly $\tilde{\omega}_{\text{AT}} = \tilde{\omega}_{\text{BeT}}$ but rather the ions are detuned by roughly $\delta \sim 2\pi \times 0.5$ Hz. A second reason is the jitter of the ions due to voltage instability and trap imperfections which leads in principle to two decoherence effects. On one hand, the various cycles within one time step are not initialized with the same δ such that the amount of transferred energy fluctuates from cycle to cycle. On the other hand, decoherence of the ions within one cycle occurs. The latter is facilitated by the fact that the transferred energy leads additionally to energy-dependent frequency shifts. Especially the BeT suffers from trap imperfections and on top of that the ion was excited to about equivalently a few hundred Kelvin. Ultimately, the resonator dissipates any excess energy of the ions and brings the energy transfer to relaxation. Even though the ions are placed far off the resonator center, the resistive cooling time constant is still only in the order of ~ 1 s for the AT ion and ~ 3.5 s for the BeT ion⁴⁰. We do not know all the effects the jitter can cause in this measurement and cannot model them any further within this thesis' framework. But we assume the energy transfer process reacts sensory to it causing the Rabi cycles to faint rapidly. Despite all the unknown effects it is remarkable that the plots indicate an exchange time of roughly $\tau_{\text{ex}} \sim 0.6$ s which is only about $\sim 10\%$ off the value predictable via eq. (46).⁴¹

Another open question is the total energy line shape (right). Since there should be literally no other energy sink except the resonator, we expect a monotone exponential energy decay only. Instead a prominent dip in the total energy curve is visible. We believe the problematic point here is the extraction of the ion energies from the bin signal strengths of the spectra. A multitude of difficulties complicate and make this extraction inaccurate: the ion jitter over time ($\omega_z(t) \neq \text{const.}$), the ion frequency dependency on its energy ($\omega_z(E) \neq \text{const.}$), the low signal-to-noise ratio (SNR) due to short spectrum acquisition times and possible frequency bleeding, the large bin resolution of ~ 0.5 Hz and imperfect traps in general.

⁴⁰As I already mentioned in footnote 34 I must give τ_{res} for the common mode of the coupled ions. However, the τ_{res} of the individual ions are a reference scale.

⁴¹The coupling position is roughly the same as in the avoided crossing measurement. Therefore, I can expect the Rabi frequencies Ω_R to be about equal. With an ion detuning of $\delta \sim 2\pi \times 0.5$ Hz the exchange time is $\tau_{\text{ex}} \sim 0.65$ s.

6 Outlook

Over the course of this thesis the first cornerstones towards sympathetic laser cooling via ${}^9\text{Be}^+$ were laid. I implemented an active laser stabilization system to tackle the hindering laser beam pointing fluctuations of our cooling laser inside the Penning trap that we observed in [7]. The system was calibrated (section 4.1) and in a first test run (section 4.2) we could stabilize the laser beam below the magnet to $\sigma_x = 25.24(7) \mu\text{m}$ and $\sigma_y = 28.28(7) \mu\text{m}$ corresponding to a 1σ width of the normally distributed x- and y-components of the beam center position. From this and the laser characterization in [58] I approximated a lower limit of the laser power scattered in our trap tower (section 4.3). The diaphragm at the top of the trap tower exposes the crucial aperture that cuts off $<0.01\%$ of the laser power injected into the trap chamber.

Tests to perform in the future would be on the one hand the comparison of beam fluctuation between stabilized and unstabilized laser beams and on the other hand the investigation of the regulation response to different interference frequencies. Generally, problematic are abrupt mechanical impacts produced by unusual occurring events such as door slamming. Their impact on the beam center position should be effectively suppressed as long as the beam pointing shift is in the regulation range of the actuators. Furthermore, the stabilization system allows us to steer and align the laser beam in situ in the trap chamber.

We also introduced and demonstrated an alternative coupling technique that aims to increase the effectiveness compared to the already existing common endcap method. Our technique utilizes a common tank circuit instead. I proposed a reduction of the trap capacitance C_p by three orders of magnitude (section 5.3.1) and therefore reduce the exchange time constant accordingly. This proposal was tested successfully in a proof of principle measurement in two parts: the demonstration of the avoided crossing pattern in section 5.4.2 and the energy transfer in section 5.4.3.

The avoided crossing measurement confirmed ion-ion coupling via the resonator with $C_{\text{eff}} = 1.989(26) \times 10^{-14} \text{ F}$. This result agrees within 0.9σ with our simulation of the Z_{tot}^\ddagger line shape model yielding $C_{\text{eff}}^{\text{sim}} = 1.958(25) \times 10^{-14} \text{ F}$. The result corresponds to a shunting of our parallel trap capacitance $C_p = 21.6 \times 10^{-12} \text{ F}$ at a coupling position of $\tilde{\omega}_0 \approx \omega_r + 2\pi \times 150 \text{ Hz}$ by a factor of ~ 1100 and therefore reduces the exchange time constant likewise.

The energy transfer measurement was successful in the way that it demonstrated a π -pulse in signal/energy transfer between the two ions. A clear and meaningful analysis within this thesis' framework, especially of the fainting data point tail and the correct energy extraction, could not be given due to lack of experience and practical knowledge, as such a measurement has not been performed yet and the experimental setup was only provisional. However, effective sympathetic cooling does require only the very first π -pulse which was in fact demonstrated.

The results of this thesis encourage to design a dedicated BeT on a more profound basis than it was done during our work. To enhance the coupling, the design of the trap can be optimized with respect to a low trap capacitance C_p and a low D_{eff} .

Furthermore, we can make use of the special feature that the BeT can be placed spatially apart from other traps. A BeT placed off-centered to the trap tower axis solves the problem of laser induced frequency shifts since the laser can exit the BeT safely through an aperture parallel to the trap tower. This way beam back-scattering into the trap tower and resulting potential shifts would be strongly suppressed. In our case though, the beam pointing stabilization system should already be sufficient to guide the beam with little scattering through our trap tower. Beside the BeT one can also take an additional dedicated coupling trap for the HCI into consideration. The HCI is then moved from the measurement traps to this coupling trap in which it is highly efficiently cooled by the laser-cooled beryllium ions in the BeT.

With the sympathetic cooling technique, the BeT and/or an additional HCI coupling trap implemented in our setup, it will be interesting to test the practical limits of method, which q/m ion species could be cooled efficiently and to ultimately perform temperature measurements on them [75] to associate a temperature with the ions.

Currently, we investigate and derive an even more extended and promising technique for sympathetic cooling based on this tank assisted coupling [76]. It utilizes many repeated but only short coupling cycles of time scales $\tau_c \ll \tau_{ex}$ in order to soften the requirements of the frequency overlap stability even further and reduce the influence of the resonator heating dramatically. There, we numerically simulated for the H_2^+ molecular ion an equilibrium temperature of $T_{eq} \approx 10$ mK which agrees with the presented theoretical description.

I want to give a final remark on the EIT point. The presented concept of cooling relies until now on the reduction of the exchange time constant to practicable time scales with $\tau_{ex} \ll \tau_{res}$. Depending on the refinement of the sympathetic cooling technique there might be weakly interacting target ions with low q/m ratio for which the above criteria cannot be fulfilled for any amount of beryllium ions N_{Be} . The EIT frequency position features a unique setting for cooling. As mentioned, the counter mode decouples from the resonator and is not influenced by its resistive heating. However, the counter mode v contributes to the target ion's axial oscillation approximately N_{Be} times more than the common mode u (see appendix D). With sufficient large $N_{Be} \gg 1$ the common mode can therefore be kept thermalized with the resonator at 4 K with negligible impact on the target ion. A sophisticated cooling of the counter mode at the EIT position could expose a technique to cool down virtually any arbitrary target ion in a Penning trap since there is no heating.

A future planned experiment at ALPHATRAP will be precision spectroscopy of forbidden rovibrational levels of molecular hydrogen H_2^+ ions on the bases of the novel spectroscopy technique presented in [7]. It is a promising candidate to provide a test of the CPT-theorem [77] and the determination of fundamental constants such as the electron-to-proton mass ratio [78].

The implementation of sympathetic cooling will bring important advantages: a cold molecular ion reduces amplitude dependent frequency shifts, reduces the first and second order Doppler shift and improves the accuracy of the phase sensitive fre-

quency measurements (PNA) [4].

With our current trap setup and parameters used in this thesis a single H_2^+ ion coupled to a single beryllium ion would exhibit exchange times in the order of 10^4 s according to the common endcap method (eq. (39)). However, with two dedicated coupling traps for the two ions (both $D_{\text{eff}} \sim 3$ mm) and the effective thousandfold reduction of the trap capacitance of our proposed method, cooling of H_2^+ becomes viable with exchange times in the order of a few seconds or possibly lower.

References

- [1] K. P. Jungmann. Fundamental interactions. *Hyperfine Interactions*, 172(1-3):5–14, 2006.
- [2] K. Blaum. High-accuracy mass spectrometry with stored ions. *Physics Reports*, 425(1):1–78, 2006.
- [3] D. Hanneke, S. Fogwell, and G. Gabrielse. New Measurement of the Electron Magnetic Moment and the Fine Structure Constant. *Physical Review Letters*, 100(12), 2008.
- [4] S. Sturm, A. Wagner, B. Schabinger, and K. Blaum. Phase-sensitive cyclotron frequency measurements at ultralow energies. *Physical Review Letters*, 107(14):143003, 2011.
- [5] S. Sturm, I. Arapoglou, A. Egl, M. Höcker, S. Kraemer, T. Sailer, B. Tu, A. Weigel, R. Wolf, J. C. López-Urrutia, and K. Blaum. The ALPHATRAP experiment. *European Physical Journal Special Topics*, 227(13):1425–1491, 2019.
- [6] I. Arapoglou. *First measurement of the ground-state g-factor of boronlike argon $^{40}\text{Ar}^{13+}$ in Alphatrap*. PhD thesis, Ruprecht-Karls-Universität, Heidelberg, 2019.
- [7] A. Egl. *High-Precision Laser Spectroscopy of the Fine Structure in $^{40}\text{Ar}^{13+}$ at ALPHATRAP*. PhD thesis, Ruprecht-Karls-Universität, Heidelberg, 2020.
- [8] M. H. Holzscheiter. Cooling of particles stored in electromagnetic traps. *Physica Scripta*, 1988(T22):73, 1988.
- [9] W. M. Itano, J. C. Bergquist, J. J. Bollinger, and D. J. Wineland. Cooling methods in ion traps. *Physica Scripta*, 1995(T59):106, 1995.
- [10] S. Mavadia, J. F. Goodwin, G. Stutter, S. Bharadia, D. R. Crick, D. M. Segal, and R. C. Thompson. Control of the conformations of ion Coulomb crystals in a Penning trap. *Nature Communications*, 4, 2013.
- [11] S. L. Rolston and G. Gabrielse. Cooling antiprotons in an ion trap. *Hyperfine Interactions*, 44(1-4):233–245, 1989.
- [12] G. Z. Li, R. Poggiani, G. Testera, and G. Werth. Adiabatic cooling of ions in the penning trap. *Zeitschrift für Physik D Atoms, Molecules and Clusters*, 22(1):375–382, 1991.
- [13] G. Z. Li, R. Poggiani, G. Testera, and G. Werth. Adiabatic cooling of antiprotons in a Penning trap. *Hyperfine Interactions*, 76(1):281–284, 1993.
- [14] D. J. Heinzen and D. J. Wineland. Quantum-limited cooling and detection of radio-frequency oscillations by laser-cooled ions. *Physical Review A*, 42(5):2977–2994, 1990.

-
- [15] H. Dehmelt. Continuous Stern-Gerlach effect: Principle and idealized apparatus. *Proceedings of the National Academy of Sciences*, 83(8):2291–2294, 1986.
- [16] L. S. Brown and G Gabrielse. Geonium theory: Physics of a single electron or ion in a Penning trap. *Reviews of Modern Physics*, 58(1):233–311, 1986.
- [17] F. G. Major, V. N. Gheorghe, and G. Werth. *Charged Particle Traps*. Springer-Verlag, Berlin, Heidelberg, 2005.
- [18] A. Weigel. *Detection Electronics Design and First Observation of Bound-Electron Spin Transitions at the ALPHATRAP g -Factor Experiment*. PhD thesis, Ruprecht-Karls-Universität, Heidelberg, 2019.
- [19] J. Ketter. *Verbesserungen der Ionennachweissysteme des Präzisions-Penningfallen- Massenspektrometers TRIGA-TRAP*. Diploma thesis, Johannes Gutenberg-Universität, Mainz, 2009.
- [20] J. Ketter. *Theoretical treatment of miscellaneous frequency-shifts in Penning traps with classical perturbation theory*. PhD thesis, Ruprecht-Karls-Universität, Heidelberg, 2015.
- [21] G. Gabrielse. Relaxation calculation of the electrostatic properties of compensated Penning traps with hyperbolic electrodes. *Physical Review A*, 27(5):2277–2290, 1983.
- [22] E. N. Nikolaev, I. A. Boldin, R. Jertz, and G. Baykut. Initial experimental characterization of a new ultra-high resolution FTICR cell with dynamic harmonization. *Journal of the American Society for Mass Spectrometry*, 22(7):1125–1133, 2011.
- [23] J. Ketter, T. Eronen, M. Höcker, S. Streubel, and K. Blaum. First-order perturbative calculation of the frequency-shifts caused by static cylindrically-symmetric electric and magnetic imperfections of a Penning trap. *International Journal of Mass Spectrometry*, 358(1):1–16, 2014.
- [24] J. Tan and G. Gabrielse. One electron in an orthogonalized cylindrical Penning trap. *Applied Physics Letters*, 55(20):2144–2146, 1989.
- [25] F. Köhler. *Bound-Electron g -Factor Measurements for the Determination of the Electron Mass and Isotope Shifts in Highly Charged Ions*. PhD thesis, Ruprecht-Karls-Universität, Heidelberg, 2015.
- [26] H. G. Dehmelt. Radiofrequency Spectroscopy of Stored Ions I: Storage. *Advances in Atomic, Molecular and Optical Physics*, 3(C):53–72, 1968.
- [27] W. Shockley. Currents to conductors induced by a moving point charge. *Journal of Applied Physics*, 9(10):635–636, 1938.
- [28] S. Ramo. Currents Induced by Electron Motion. *Proceedings of the IRE*, 27(9):584–585, 1939.

-
- [29] R. M. Weisskopf. *Detecting Single, Trapped Ions*. PhD thesis, Massachusetts Institute of Technology, 1988.
- [30] M Höcker. *Precision Mass Measurements at THE-Trap and the FSU trap*. PhD thesis, Ruprecht-Karls-Universität, Heidelberg, 2016.
- [31] J. B. Johnson. Thermal Agitation of Electricity in Conductors. *Nature*, 119(2984):50–51, 1927.
- [32] H. Nyquist. Thermal Agitation of Electric Charge in Conductors. *Physical Review*, 32(1):110–113, 1928.
- [33] S. Sturm. *The g -factor of the electron bound in $^{28}\text{Si}^{13+}$: The most stringent test of bound-state quantum electrodynamics*. PhD thesis, Johannes Gutenberg-Universität, Mainz, 2012.
- [34] H. G. Dehmelt. Radiofrequency Spectroscopy of Stored Ions II: Spectroscopy. *Advances in Atomic, Molecular and Optical Physics*, 5(C):109–154, 1969.
- [35] M. P. Bradley. *A Sub-ppb Measurement of the Mass of Cesium for a New Determination of the Fine-Structure*. PhD thesis, Massachusetts Institute of Technology, 2000.
- [36] D. J. Wineland and H. G. Dehmelt. Principles of the stored ion calorimeter. *Journal of Applied Physics*, 46(2):919–930, 1975.
- [37] A. Weigel. *Entwicklung des kryogenen Nachweissystems für ALPHATRAP und THE-Trap*. Master’s thesis, Ruprecht-Karls-Universität Heidelberg, 2019.
- [38] S. Ulmer. *First Observation of Spin Flips with a Single Proton Stored in a Cryogenic Penning Trap*. PhD thesis, Ruprecht-Karls-Universität, Heidelberg, 2011.
- [39] E. A. Cornell, R. M. Weisskoff, K. R. Boyce, and D. E. Pritchard. Mode coupling in a Penning trap: π pulses and a classical avoided crossing. *Physical Review A*, 41(1):312–315, 1990.
- [40] A. Wagner, S. Sturm, F. Köhler, D. A. Glazov, A. V. Volotka, G. Plunien, W. Quint, G. Werth, V. M. Shabaev, and K. Blaum. g Factor of Lithiumlike Silicon $^{28}\text{Si}^{11+}$. *Physical Review Letters*, 110(3):033003, 2013.
- [41] F. Heiße, F. Köhler-Langes, S. Rau, J. Hou, S. Junck, A. Kracke, A. Mooser, W. Quint, S. Ulmer, G. Werth, K. Blaum, and S. Sturm. High-Precision Measurement of the Proton’s Atomic Mass. *Physical Review Letters*, 119(3):033001, 2017.
- [42] D. A. Glazov, F. Köhler-Langes, A. V. Volotka, K. Blaum, F. Heiße, G. Plunien, W. Quint, S. Rau, V. M. Shabaev, S. Sturm, and G. Werth. g Factor of Lithiumlike Silicon: New Challenge to Bound-State QED. *Physical Review Letters*, 123(17):173001, 2019.
-

-
- [43] J. Alonso, K. Blaum, S. Djekic, H. J. Kluge, W. Quint, B. Schabinger, S. Stahl, J. Verdú, M. Vogel, and G. Werth. [A miniature electron-beam ion source for in-trap creation of highly charged ions](#). *Review of scientific instruments*, 77(3):03A901, 2006.
- [44] B. Franzke. [The heavy ion storage and cooler ring project ESR at GSI](#). *Nuclear Inst. and Methods in Physics Research, B*, 24-25(PART 1):18–25, 1987.
- [45] H. J. Kluge, T. Beier, K. Blaum, L. Dahl, S. Eliseev, F. Herfurth, B. Hofmann, O. Kester, S. Koszudowski, C. Kozhuharov, G. Maero, W. Nörtershäuser, J. Pfister, W. Quint, U. Ratzinger, A. Schempp, R. Schuch, Th Stöhlker, R. C. Thompson, M. Vogel, G. Vorobjev, D. F.A. Winters, and G. Werth. [Chapter 7 HITRAP: A Facility at GSI for Highly Charged Ions](#). In *Advances in Quantum Chemistry*, volume 53 of *Advances in Quantum Chemistry*, pages 83–98. Academic Press, 2008.
- [46] A. J. González Martínez, J. R. Crespo López-Urrutia, D. Fischer, R. Soria Orts, and J. Ullrich. [The heidelberg EBIT: Present results and future perspectives](#). *Journal of Physics: Conference Series*, 72(1), 2007.
- [47] P. Micke, S. Kühn, L. Buchauer, J. R. Harries, T. M. Bücking, K. Blaum, A. Cieluch, A. Egl, D. Hollain, S. Kraemer, T. Pfeifer, P. O. Schmidt, R. X. Schüssler, Ch Schweiger, T. Stöhlker, S. Sturm, R. N. Wolf, S. Bernitt, and J. R. Crespo López-Urrutia. [The Heidelberg compact electron beam ion traps](#). *Review of Scientific Instruments*, 89(6):063109, 2018.
- [48] T. Sailer. [A Laser Ion Source for the ALPHATRAP Experiment](#). Master’s thesis, Ruprecht-Karls-Universität Heidelberg, 2017.
- [49] I. Bergström, C. Carlberg, T. Fritioff, G. Douysset, J. Schönfelder, and R. Schuch. [SMILETRAP - A Penning trap facility for precision mass measurements using highly charged ions](#). *Nuclear Instruments and Methods in Physics Research, Section A: Accelerators, Spectrometers, Detectors and Associated Equipment*, 487(3):618–651, 2002.
- [50] M. Turkalj Orešković. [Development of a cryogenic vacuum valve and an electromechanical switch for ALPHATRAP](#). Master’s thesis, Ruprecht-Karls-Universität, Heidelberg, 2014.
- [51] M. Schuh, F. Heiße, T. Eronen, J. Ketter, F. Köhler-Langes, S. Rau, T. Segal, W. Quint, S. Sturm, and K. Blaum. [Image charge shift in high-precision Penning traps](#). *Physical Review A*, 100(2):023411, 2019.
- [52] TOPTICA Photonics AG. [TA-FHG pro Manual](#). TOPTICA Photonics AG, Lochhamer Schlag 19, 82166 Graefelfing, Germany, 2019.
- [53] D. J. Wineland, C. Monroe, W. M. Itano, D. Leibfried, B. E. King, and D. M. Meekhof. [Experimental Issues in Coherent Quantum-State Manipulation of Trapped Atomic Ions](#). *Journal of Research of the National Institute of Standards and Technology*, 103(3):259–328, 1998.
-

-
- [54] A. E. Kramida. Critical Compilation of Wavelengths and Energy Levels of Singly Ionized Beryllium (Be II). *Physica Scripta*, 72(4):309–319, 2005.
- [55] T. Andersen, K. A. Jessen, and G. Sørensen. Mean-life measurements of excited electronic states in neutral and ionic species of beryllium and boron. *Physical Review*, 188(1):76–81, 1969.
- [56] HighFinesse GmbH. *HighFinesse / Wavelength Meter WS8-2*. HighFinesse GmbH, Wöhrdstr. 4, 72072 Tübingen, Germany, 2020.
- [57] Lasertex Co. Ltd. *Frequency Laser Standard: Iodine stabilised He-Ne laser*. Lasertex Co. Ltd., ul. Swojczycka 26, 51-501 Wrocław, Poland, 2019., 2020.
- [58] S. Kraemer. Towards Laser Cooling of Beryllium Ions at the ALPHATRAP Experiment. Master’s thesis, Ruprecht-Karls-Universität, Heidelberg, 2017.
- [59] T. P. Steinsberger. Microwave injection for the ALPHATRAP experiment and developments of the multi-reflection time-of-flight technique of the ISOLTRAP experiment. Master’s thesis, Ruprecht-Karls-Universität, Heidelberg, 2018.
- [60] C. D. Marciniak, H. B. Ball, A. T. H. Hung, and M. J. Biercuk. Towards fully commercial, UV-compatible fiber patch cords. *Optics Express*, 25(14):15643, 2017.
- [61] P. Karlitschek, G. Hillrichs, and K. F. Klein. Influence of hydrogen on the colour center formation in optical fibers induced by pulsed UV-laser radiation. Part 2: All-silica fibers with low-OH undoped core. *Optics Communications*, 155(4-6):386–397, 1998.
- [62] P. Karlitschek, G. Hillrichs, and K. F. Klein. Influence of hydrogen on the colour center formation in optical fibers induced by pulsed UV-laser radiation. Part 1: All silica fibers with high-OH undoped core. *Optics Communications*, 155(4-6):376–385, 1998.
- [63] Y. Colombe, D. H. Slichter, A. C. Wilson, D. Leibfried, and D. J. Wineland. Single-mode optical fiber for high-power, low-loss UV transmission. *Optics Express*, 22(16):19783, 2014.
- [64] MRC Systems GmbH Medizintechnische Systeme. *Laser Beam Stabilisation System "Compact" User Manual*. MRC Systems GmbH - Medizintechnische Systeme, Hans-Bunte-Str. 8, 69123 Heidelberg, Germany, 2019.
- [65] S. Bogen. Frequenz-, Leistungs- und Positionsstabilisierung von UV-Lasersystemen für Frequenzmetrologie mit hochgeladenen Ionen. Master’s thesis, Ruprecht-Karls-Universität Heidelberg, 2019.
- [66] M. Bohman, A. Mooser, G. Schneider, N. Schön, M. Wiesinger, J. Harrington, T. Higuchi, H. Nagahama, C. Smorra, S. Sellner, K. Blaum, Y. Matsuda, W. Quint, J. Walz, and S. Ulmer. Sympathetic cooling of protons and antiprotons with a common endcap Penning trap. *Journal of Modern Optics*, 65(5-6):568–576, 2018.

-
- [67] J. Home. Seminar on Precision Physics and Fundamental Symmetries: Quantum computing with trapped ions, 2020.
- [68] D. J. Larson, J. C. Bergquist, J. J. Bollinger, Wayne M. Itano, and D. J. Wineland. Sympathetic cooling of trapped ions: A laser-cooled two-species nonneutral ion plasma. *Physical Review Letters*, 57(1):70–73, 1986.
- [69] L. Gruber, J. P. Holder, J. Steiger, B. R. Beck, H. E. DeWitt, J. Glassman, J. W. McDonald, D. A. Church, and D. Schneider. Evidence for highly charged ion Coulomb crystallization in multicomponent strongly coupled plasmas. *Physical Review Letters*, 86(4):636–639, 2001.
- [70] K. R. Brown, C. Ospelkaus, Y. Colombe, A. C. Wilson, D. Leibfried, and D. J. Wineland. Coupled quantized mechanical oscillators. *Nature*, 471(7337):196–199, 2011.
- [71] M. Harlander, R. Lechner, M. Brownnutt, R. Blatt, and W. Hänsel. Trapped-ion antennae for the transmission of quantum information. *Nature*, 471(7337):200–203, 2011.
- [72] C. Smorra, K. Blaum, L. Bojtar, M. Borchert, K.A. Franke, T. Higuchi, N. Leefer, H. Nagahama, Y. Matsuda, A. Mooser, M. Niemann, C. Ospelkaus, W. Quint, G. Schneider, S. Sellner, T. Tanaka, S. Van Gorp, J. Walz, Y. Yamazaki, and S. Ulmer. BASE - The Baryon Antibaryon Symmetry Experiment. *The European Physical Journal Special Topics 2015 224:16*, 224(16):3055–3108, 2015.
- [73] E. Jordan, K. A. Gilmore, A. Shankar, A. Safavi-Naini, J. G. Bohnet, M. J. Holland, and J. J. Bollinger. Near Ground-State Cooling of Two-Dimensional Trapped-Ion Crystals with More than 100 Ions. *Physical Review Letters*, 122(5), 2019.
- [74] Stahl-Electronics. *3-channel ultra high precision voltage sources UM 1-14 LN*. Stahl-Electronics, Kellerweg 23, 67582 Mettenheim, Germany, 2020.
- [75] S. Djekic, J. Alonso, H. J. Kluge, W. Quint, S. Stahl, T. Valenzuela, J. Verdú, M. Vogel, and G. Werth. Temperature measurement of a single ion in a Penning trap. *The European Physical Journal D - Atomic, Molecular, Optical and Plasma Physics*, 31(3):451–457, 2004.
- [76] T. Bingsheng, F. Hahne, I. Arapoglou, A. Egl, F. Heiße, M. Höcker, T. Sailer, A. Weigel, K. Blaum, and S. Sturm. A tank-circuit assisted coupling method for sympathetic laser cooling. *To be submitted*.
- [77] E. G. Myers. *CPT* tests with the antihydrogen molecular ion. *Phys. Rev. A*, 98:010101, 2018.
- [78] S. Schiller and V. Korobov. Tests of time independence of the electron and nuclear masses with ultracold molecules. *Phys. Rev. A*, 71:032505, 2005.

7 Acknowledgements

Right now at this moment I'm wondering how many questions I've actually asked this year. There must have been a million, for sure. In the background Donkey Kong music is playing almost unnoticed. I guess it is the same as when I wrote my first page here. I have long forgotten how often the same playlist has been played. A year ago I wouldn't have believed to sit here in the dark in melancholy and type the last words of my thesis on the blinding screen. Of course, I'm happy to write the final period, and yet I will miss writing this thesis, because I am very happy to be able to work on what I think is such an exciting project in such a great environment. Therefore, it is only appropriate to at least thank everyone who has personally supported and accompanied me with the work.

Dear Klaus, you have created a great environment with exceptional working conditions. It is a pleasure to study under your supervision. I respect your dedication and trust to our science, your work groups and really each and every one of us. I don't think that this is a given.

Furthermore, I also thank Alexander Dorn for taking on the role of second reviewer. Dear Sven, I can only repeat what others have already thanked you for. It is fascinating when you draw from your infinite know-how, pour your knowledge over smoking heads and still create great motivation. I appreciate that you give us freedom to choose and responsibility. I enjoy being part of ALPHATRAP. Dear Bingsheng, you taught me the necessary techniques. But you also took every thought, idea and question I had seriously and you took your time for it. I give you high credit for that and I think that we had very profitable discussions because of this. I could not have been happier to work with you on this measurement. You are a great, funny person and you wear cool shoes. Dear Alex and Tim, I thank you for being irreplaceable contact persons for me, especially at the beginning when I had to find my way around. It is always a joy being around you two to listen to you ramble or your fool's talk – it makes the atmosphere so much more lively. I will never want to move into another office. Oh, and I almost forgot to point out your scientific expertise. Dear Fabian, one can recognize your fascination at first sight. Thank you for giving me input and helping me out as well. I appreciate that you always have an opinion on whatever topic. Dear Jonathan and Charlotte, you two are super friendly. I really can see myself working with you together and next to you forming the next generation of PhD students.

Moreover, I want to reach out to Ioanna, Andreas and the members of Pentatrap and THE-trap. I wish you all the best.

Erklärung:

Ich versichere, dass ich diese Arbeit selbstständig verfasst habe und keine anderen als die angegebenen Quellen und Hilfsmittel benutzt habe.

Heidelberg, den (Datum)

Appendices

A Effective Resonator Parameters

Writing out eq. (18) explicitly yields

$$\begin{aligned} Z_{\text{res}}(\omega) &= \left[\frac{1}{R_p} + i \left(\frac{\omega}{\omega_r^2 L} - \frac{\omega_r^2 C}{\omega} \right) \right]^{-1} \\ &= \left[\frac{1}{R_p} \left(1 + iQ \left(\frac{\omega}{\omega_r} - \frac{\omega_r}{\omega} \right) \right) \right]^{-1}. \end{aligned} \quad (50)$$

From here we can approximate the two parameters C_{eff} and R_{eff} .

A.1 Effective Capacitance C_{eff}

The complex part of the impedance Z_{res} is

$$\text{Im}(Z_{\text{res}}) = \frac{Z_{\text{res}} - Z_{\text{res}}^*}{2} = \frac{R_p Q \left(\frac{\omega_r}{\omega} - \frac{\omega}{\omega_r} \right)}{1 + Q^2 \left(\frac{\omega}{\omega_r} - \frac{\omega_r}{\omega} \right)^2}. \quad (51)$$

With the detuning from the resonator $\Delta_r = \omega - \omega_r$ we can further write

$$\text{Im}(Z_{\text{res}}(\omega)) = -\frac{QR_p \left(\frac{\omega_r + \Delta_r}{\omega_r} - \frac{\omega_r}{\omega_r + \Delta_r} \right)}{1 + Q^2 \left(\frac{\omega_r + \Delta_r}{\omega_r} - \frac{\omega_r}{\omega_r + \Delta_r} \right)^2} \approx -\frac{QR_p \left(\frac{\omega_r + \Delta_r}{\omega_r} - \frac{\omega_r}{\omega_r + \Delta_r} \right)}{Q^2 \left(\frac{\omega_r + \Delta_r}{\omega_r} - \frac{\omega_r}{\omega_r + \Delta_r} \right)^2}. \quad (52)$$

The approximation in the denominator is the most critical one compared to following simplifications. It is only valid for a sufficiently large detuning, in our case a few ten Hertz. The brackets cancel and we rewrite the denominator

$$\text{Im}(Z_{\text{res}}(\omega)) = -\frac{R_p}{Q \frac{\Delta_r(2\omega_r + \Delta_r)}{\omega_r(\omega_r + \Delta_r)}} = -\frac{R_p \omega_r}{Q \Delta_r} \frac{\omega_r + \Delta_r}{2\omega_r + \Delta_r} \approx -\frac{R_p \omega_r}{2Q \Delta_r} \stackrel{(19)}{=} -\frac{1}{2C_p \Delta_r}. \quad (53)$$

The expression for the effective capacitance is then

$$C_{\text{eff}} = -\frac{1}{\text{Im}(Z_{\text{res}})(\omega_r + \Delta_r)} = \frac{2C_p \Delta_r}{\omega_r + \Delta_r} \approx 2C_p \frac{\Delta_r}{\omega_r}. \quad (54)$$

A.2 Effective Resistance R_{eff}

The real part of the impedance reads

$$\text{Re}(Z_{\text{res}}(\omega)) = \frac{Z_{\text{res}} + Z_{\text{res}}^*}{2} = \frac{R_p}{1 + Q^2 \left(\frac{\omega}{\omega_r} - \frac{\omega_r}{\omega} \right)^2} \stackrel{(*)}{\approx} \frac{R_p}{Q^2 \left(\frac{\Delta_r(2\omega_r + \Delta_r)}{\omega_r(\omega_r + \Delta_r)} \right)^2} \quad (55a)$$

$$= \frac{R_p \omega_r^2 (\omega_r + \Delta_r)^2}{Q^2 \Delta_r^2 (2\omega_r + \Delta_r)^2} \approx \frac{R_p \omega_r}{4Q^2 \Delta_r^2} \quad (55b)$$

Again, the approximation made in (\star) practicably limits the validation of the calculations near the resonator center.

B Derivation of the Rabi Frequency with and without Detuning

Our starting point are the EOMs (44). As already mentioned, for this estimation we leave out the damping terms.

B.1 No Detuning - Ideal Coupling

For now let us consider a perfectly coupled scenario $\tilde{\omega}_{z,1} = \tilde{\omega}_{z,2} \equiv \tilde{\omega}$:

$$\ddot{z}_1 = -\tilde{\omega}^2 z_1 - k_1 z_2, \quad (56a)$$

$$\ddot{z}_2 = -\tilde{\omega}^2 z_2 - k_2 z_1. \quad (56b)$$

We expect the motions to be amplitude modulated with the Rabi frequency. The ansatz $z_i = z_{0i}(t)e^{i\tilde{\omega}t}$ gives access to the time varying amplitude $z_{0i}(t)$. We write out the time derivatives and get

$$\ddot{z}_{01} + 2i\tilde{\omega}\dot{z}_{01} - \tilde{\omega}^2 z_{01} = -\tilde{\omega}^2 z_{01} - k_1 z_{02}, \quad (57a)$$

$$\ddot{z}_{02} + 2i\tilde{\omega}\dot{z}_{02} - \tilde{\omega}^2 z_{02} = -\tilde{\omega}^2 z_{02} - k_2 z_{01}. \quad (57b)$$

We further neglect the acceleration terms. Considering that the amplitudes vary with the Rabi frequency in time, which is much slower than their actual ion's axial frequency, justifies the simplification in our case. We are thus left with only

$$2i\tilde{\omega}\dot{z}_{01} = -k_1 z_{02}, \quad (58a)$$

$$2i\tilde{\omega}\dot{z}_{02} = -k_2 z_{01}. \quad (58b)$$

We can decouple the equations if we take the time derivative of (58a) and insert (58b) to estimate the Rabi frequency Ω_R

$$2i\tilde{\omega}\dot{z}_{01} = -k_1\dot{z}_{02} = \frac{k_1 k_2}{2i\tilde{\omega}} z_{01} \quad \longrightarrow \quad \ddot{z}_{01} = -\overbrace{\frac{k_1 k_2}{4\tilde{\omega}^2}}^{\frac{1}{4}\Omega_R^2} z_{01}, \quad (59a)$$

$$\Omega_R = \frac{q_1 q_2}{\tilde{\omega} D_1 D_2 \sqrt{m_1 m_2} C_{\text{eff}}(\omega)}. \quad (59b)$$

Note that the effective capacitance $C_{\text{eff}}(\omega)$ corresponds to the original frequency ω and not the pushed common coupling frequency $\tilde{\omega}$.

B.2 With Detuning - Real Coupling

Now consider that one ion has a slightly different frequency. Without loss of generality we set $\tilde{\omega}_{z,1} = \tilde{\omega}$ and $\tilde{\omega}_{z,2} = \tilde{\omega} + \delta$. The small difference in frequency is expressed

by the detuning $\delta = \tilde{\omega}_{z,2} - \tilde{\omega}_{z,1}$. The coupled EOMs without damping terms are

$$\ddot{z}_1 = -\tilde{\omega}^2 z_1 - k_1 z_2, \quad (60a)$$

$$\ddot{z}_2 = -(\tilde{\omega} + \delta)^2 z_2 - k_2 z_1. \quad (60b)$$

Again we choose the ansatz $z_1 = z_{01}(t)e^{i\tilde{\omega}t}$ and $z_2 = z_{02}(t)e^{i(\tilde{\omega}+\delta)t}$:

$$\ddot{z}_{01} + 2i\tilde{\omega}\dot{z}_{01} - \tilde{\omega}^2 z_{01} = -\tilde{\omega}^2 z_{01} - k_1 z_{02}e^{i\delta t}, \quad (61a)$$

$$\ddot{z}_{02} + 2i(\tilde{\omega} + \delta)\dot{z}_{02} - \tilde{\omega}^2 z_{02} = -\tilde{\omega}^2 z_{02} - k_2 z_{01}e^{-i\delta t}. \quad (61b)$$

The exact same argument as above allows us to neglect the acceleration terms. The coupled amplitudes now read

$$2i\tilde{\omega}\dot{z}_{01} = -k_1 z_{02}e^{i\delta t}, \quad (62a)$$

$$2i(\tilde{\omega} + \delta)\dot{z}_{02} = -k_2 z_{01}e^{-i\delta t}. \quad (62b)$$

The time derivative of (62a) is

$$2i\tilde{\omega}\ddot{z}_{01} = -k_1\dot{z}_{02}e^{i\delta t} - i\delta k_1 z_{02}e^{i\delta t} = k_1 e^{i\delta t}(\dot{z}_{02} + i\delta z_{02}). \quad (63)$$

Inserting \dot{z}_{02} for z_{01} and z_{02} for \dot{z}_{01} leaves over a decoupled expression and the exponential factor cancel out. We can extract the detuned Rabi frequency Ω_δ

$$2i\tilde{\omega}\ddot{z}_{01} = -2\tilde{\omega}\delta\dot{z}_{01} + \frac{k_1 k_2}{2i(\tilde{\omega} + \delta)} z_{01} \quad \longrightarrow \quad \ddot{z}_{01} = i\delta\dot{z}_{01} - \overbrace{\frac{k_1 k_2}{2\tilde{\omega}(\tilde{\omega} + \delta)}}^{\frac{1}{4}\Omega_\delta^2} z_{01}, \quad (64a)$$

$$\Omega_\delta = \frac{q_1 q_2}{D_1 D_2 \sqrt{\tilde{\omega}(\tilde{\omega} + \delta)} m_1 m_2} \frac{1}{C_{\text{eff}}(\omega_{z,1}, \omega_{z,2})}, \quad (64b)$$

where $C_{\text{eff}} = \sqrt{C_{\text{eff},1} C_{\text{eff},2}}$ was defined. However, due to the complex damping term the amplitude is modulated by the generalized Rabi frequency

$$\tilde{\Omega}_G = \sqrt{\delta^2 + \Omega_\delta^2}. \quad (65)$$

Analogous to the ideally coupled case the effective capacitance depends on the original ion frequencies. The detuning was defined in a way to keep the coupled equations at a minimal complexity but please note that δ has the frequency pushing effect already included.

C Avoided Crossing Fitting Routines

Here I cover the most important technical details and concerns of the avoided crossing fitting analysis. Any fit described here is based on the MATLAB `lsqnonlin` function. The values of a set of parameter describing the fit model from eq. (21b) are varied to fit the experimental data. Depending on the context of Z different parameters are probed.

I use the term *to fix a parameter* when one or more parameters are being probed and their final value is thoroughly fixed for any other subsequent fit in order to address other important measurands.

We speak of *to let a parameter free* when such a parameter is necessarily used to guide the fit model but not fixed for the subsequent fits.

C.1 Effective Electrode Distance D_{eff}

The first step is to estimate $D_{\text{eff,AT}}$ and $D_{\text{eff,BeT}}$. The dip signal of a single ion at the resonator center is fitted with D_{eff} as the fit parameter. However, in order to extract the ion properties from the dip signal we need to characterize the underlying resonator noise signal first. The resonator itself is actually fully described by the parameter set (Q, ω_r, \tilde{A}) . The optional \tilde{u}_{en} and $\tilde{\kappa}_{\text{det}}$ represent possible detection effects. These parameters are priorly estimated from spectra of an empty AT without applied voltages. They serve only as an initial guiding input value for the actual resonator fitting to properly converge.

With the help of the initial resonator input we can fix the resonator finally on basis of the sought after ion spectrum. This time however the full line shape Z_{tot} is fitted and the mean resonator parameters $(Q, \omega_r, \tilde{A}, \tilde{u}_{\text{en}}, \tilde{\kappa})$ are fixed out of 150 spectra while the ion parameters $(\omega_i, D_{\text{eff},i}, \sigma)$ are let free. This is done for the AT and the BeT accordingly. In the same way but now with an already fixed resonator noise the jitter σ of the BeT ion can be extracted and additionally fixed. This jitter parameter is explained in the frequency fitting stage C.3. At last, the other two parameters are fixed together as well yielding a final mean D_{eff} value for both traps.

Unfortunately we estimated D_{eff} not until 3 months after our measurement campaign. The resonator properties might have drifted within that timescale leaving them not comparable with the avoided crossing resonator results. E.g. micro displacements of the electrodes during the LHe tank refilling process might cause a change in ω_r . However, D_{eff} is a pure trap geometry parameter and should not change significantly to first order from these small micro displacements.

During the D_{eff} determination the trap stored a single $^{40}\text{Ca}^{16+}$. The fitting had to be done with the available ion. We rescaled the voltage settings for $^{40}\text{Ar}^{11+}$ with the calcium charge-to-mass ratio in order to reproduce the same double well potential used during the measurement campaign. This represents the same prior D_{eff} and therefore hand over the correct value.

Table 6: Mean results of D_{eff} fitting for both traps and their absolute error contributions. The MATLAB *nliparci*-function is the leading error and gives the 1σ confidence interval of the parameter value. The other error represent the parameter error propagation throughout all fitting steps.⁴² Additionally the statistical standard error of the mean is given in the second bracket arising from averaging over 150 fixed values per parameter from each spectrum.

	$D_{\text{eff,AT}}/\text{mm}$	$D_{\text{eff,BeT}}/\text{mm}$
nliparci	0.12	0.22
ΔQ	0.01	0.01
ΔA	0.05	0.08
$\Delta\omega_r$	<0.01	<0.01
Δu_{en}	<0.01	<0.01
$\Delta\tilde{\kappa}_{\text{det}}$	<0.01	<0.01
$\Delta\sigma$		0.12
stat. mean	0.01	0.03
Total	17.97(13)(1)	24.45(27)(3)

Nevertheless, as shown in table 6 the fixed mean effective electrode distances D_{eff} for both traps are estimated with a relative uncertainty of approximately $\sim 1\%$.

C.2 Resonator Parameters

The second fitting stage covers the characterization of the resonator for the avoided crossing measurement spectra. Ideally, we would have recorded the resonator noise before the measurement run with an underlying empty and grounded trap for this purpose. We obtained 201 spectra containing the two ion signals, and we aim to extract the resonator parameters while excluding the coupling region from the fitting. However, it is important to use Z_{tot} here instead of only Z_{res} . Z_{tot} is slightly lowered in a broad vicinity around the coupling region compared to Z_{res} . Fitting only the Z_{res} model therefore increases the residuals to the actual data in that vicinity thus effectively shifting in our case the center ω_r by approximately ~ 1 Hz closer to the coupling region.

Hence, $(Q, \omega_r, \tilde{A}, \tilde{u}_{\text{en}}, \tilde{\kappa}_{\text{det}})$ are fixed while $(\omega_{\text{AT}}, \omega_{\text{BeT}}, \sigma)$ are let free. The mean values of the fixed resonator parameters are listed in table 7 with the same error scheme as is table 6.

⁴²E.g. the resonator parameters were fixed at some point prior to the final D_{eff} fitting but still come along with their own nliparci-errors, which need to be included. The propagation is gauged by varying the corresponding parameter with its fixation value \pm its nliparci-error. We then compare the consequential $D_{\text{eff,err}}$ with the original unperturbed value and give their difference as the error propagation (e.g. compare D_{eff} estimated originally via $(Q, \omega_r, \tilde{A}, \tilde{u}_{\text{en}}, \tilde{\kappa}, \sigma)$ with $D_{\text{eff,err}}$ estimated via $(Q \pm \Delta Q, \omega_r, \tilde{A}, \tilde{u}_{\text{en}}, \tilde{\kappa}, \sigma)$).

Table 7: The total values are the mean values of the resonator parameter that were fixed for each of the 201 measurement spectra. The uncertainties are calculated and presented in the exact same way as in table 6.

	$\omega_r/(2\pi \times \text{Hz})$	Q	\tilde{A}/V^{rms}	$\tilde{u}_{\text{en}}/V^{\text{rms}}$	$\tilde{\kappa}/(V^{\text{rms}} \text{ s})$
nliparci	0.11	34	12	0.004	20×10^{-7}
$\Delta D_{\text{eff,AT}}$	0.01	<1	<1	<0.001	$<1 \times 10^{-7}$
$\Delta D_{\text{eff,AT}}$	0.01	<1	<1	<0.001	$<1 \times 10^{-7}$
stat. mean	0.01	3	1	<0.001	2×10^{-7}
Total	334210.60(11)(1)	7016(34)(3)	1455(12)(1)	1.885(4)	$-8(20)(2) \times 10^{-7}$

C.3 Ion Frequencies and Jitter

After the resonator parameters (i.e. Z_{res}) were fixed, we can investigate the small frequency window $-2\pi \times 10 \text{ Hz} < \omega_{\text{AT}} < 2\pi \times 10 \text{ Hz}$ containing the coupling region. This step aims to fix the frequency parameter set $(\omega_{\text{AT}}, \omega_{\text{BeT}}, \sigma)$. The first two represent the original frequencies of the AT and BeT ion while the latter describes the BeT ion jitter, that leads to the signal smear-out.

We use a normal distribution to model BeT frequency fluctuation that occurs during the total acquisition time of a spectrum, because the voltage source exhibits normally distributed voltage fluctuations on a short scale.⁴³ σ is then the width of the frequency distribution around the actual mean value ω_{BeT} .

To this end, during the fitting we prepare 100 frequency entries normally distributed around ω_{BeT} with standard deviation σ . This yields 100 impedance line shapes Z_{tot} with equal parameter settings except for ω_{BeT} , which are averaged to a mean line shape. According to this procedure the values of $(\omega_{\text{AT}}, \omega_{\text{BeT}}, \sigma)$ for all 201 spectra are stored in a matrix and passed on to the C_{eff} fitting stage rather than being averaged as before. However, I unify their individual errors and give them in table 8. Although the ion setup differs over the measurement course for their frequency and jitter uncertainties I see no reason to systematically change.

C.4 C_{eff} Fitting Routines

Now that the frequencies and the BeT jitter have been fixed and recorded in a matrix, I can finally estimate C_{eff} via the two different techniques/routines. During both routines I assign each spectrum its corresponding frequency setup $(\omega_{\text{AT}}, \omega_{\text{BeT}}, \sigma)$ from the previously recorded frequency matrix while maintaining the resonator parameters thoroughly fixed. This is done to account for the AT frequency bin jumping and the sweep through of the BeT ion.

Table 9 lists the end results for our two fitting routines—the effective trap capaci-

⁴³Additional drifts may happen, mainly due to temperature shifts of the source, but these occur on a long timescale.

Table 8: Results of the frequency fitting. Again, the parameter uncertainties and the error propagation of priorly fixed parameters are given.

Contribution	$\omega_{\text{AT}}/(2\pi \times \text{Hz})$	$\omega_{\text{BeT}}/(2\pi \times \text{Hz})$	$\sigma/(2\pi \times \text{Hz})$
nliparci	0.0009	0.0014	0.0051
$\Delta D_{\text{eff,BeT}}$	<0.0001	0.0004	0.0004
$\Delta D_{\text{eff,AT}}$	0.0009	0.0001	0.0002
$\Delta\omega_r$	0.0001	0.0001	<0.0001
ΔQ	0.0003	0.0003	0.0001
$\Delta\tilde{A}$	<0.0001	0.0001	0.0001
$\Delta\tilde{u}_{\text{en}}$	<0.0001	<0.0001	<0.0001
$\Delta\tilde{\kappa}$	<0.0001	<0.0001	<0.0001
Total error	<0.0013	<0.0015	<0.0008

tance. The first method $C_{\text{eff}}^{(1)}$ is the mean value of the 201-times fixed C_{eff} parameter and thus features a statistical error of the mean value, while $C_{\text{eff}}^{(2)}$ had to be fixed only once.

However, for both routines some spectra in the very vicinity of $\tilde{\omega}_{\text{AT}} = \tilde{\omega}_{\text{BeT}}$ were unable to be fitted properly because the original ion frequencies could not be detected under the signal noise. To that effect a total of 18 out of the initial 201 spectra were excluded from the analysis within this final stage.

Table 9: Presented are the total values of the effective trap capacitance for both fitting routines and their error contributions according to table 6 except for both parameters D_{eff} and $\Delta\omega_{\text{AT}}$.

Contribution	$C_{\text{eff}}^{(1)}/(10^{-14} \text{ F})$	$C_{\text{eff}}^{(2)}/(10^{-14} \text{ F})$
nliparci	0.025	0.002
$\Delta D_{\text{eff,BeT}}$	0.016	0.016
$\Delta D_{\text{eff,AT}}$	0.006	0.006
$\Delta\omega_{\text{r}}$	0.001	0.001
ΔQ	0.005	0.005
$\Delta\tilde{A}$	0.002	0.002
$\Delta\tilde{u}_{\text{en}}$	<0.001	<0.001
$\Delta\tilde{\kappa}$	<0.001	<0.001
$\Delta\omega_{\text{AT}}$	0.017	0.017
$\Delta\omega_{\text{BeT}}$	0.005	0.005
$\Delta\sigma$	0.003	0.003
stat. mean	0.002	
Total	1.994(36)(2)	1.989(26)

D Time-Independent Modes of the Coupled Ion System

I use the following notation. The subscripts 1 and 2 correspond to an arbitrary ion 1 and the ${}^9\text{Be}^+$ ions, respectively. E.g. D_1 and D_2 denote the effective trap length of the ion 1 and the beryllium trap. N is the number of beryllium ions and Z denotes the ion's charge state. We treat all beryllium ions as one coherent cloud with

$$q_2 = \frac{N}{Z}q_1 \equiv \frac{N}{Z}q \quad \text{and} \quad \frac{q_2}{m_2} = \beta \frac{q_1}{m_1} \equiv \beta \frac{q}{m}. \quad (66)$$

For the counter mode we consider the general Ansatz $v = z_1 + \gamma z_2$ with γ being an arbitrary constant. We know that the signal voltage for the counter mode v must vanish at the EIT position $\omega_{z,1} = \omega_{z,2} = \omega_z$, which implies:

$$\left(\frac{q_1}{m_1 D_1} + \gamma \frac{q_2}{m_2 D_2} \right) u_{\text{sig}} \stackrel{!}{=} 0 = \frac{q}{m} \left(\frac{1}{D_1} + \gamma \frac{\beta}{D_2} \right) \quad \longrightarrow \quad \gamma = -\frac{D_2}{\beta D_1}. \quad (67)$$

We can already write down the counter mode as a superposition of the individual ion oscillations as

$$v = z_1 - z_2 \frac{D_2}{\beta D_1} \quad (68)$$

Because the counter mode does not induce a signal, the overall induced current is exclusively given by the common mode u

$$i_{\text{tot}} = i_{\text{ind},1} + i_{\text{ind},2} = \frac{q_1}{D_1} \dot{z}_1 + \frac{q_2}{D_2} \dot{z}_2 = \frac{q}{D_1} \left(\dot{z}_1 + \frac{N D_1}{Z D_2} \dot{z}_2 \right) \equiv \frac{q}{D_1} \dot{u} \quad (69)$$

This allows us writing down the common mode as

$$u = z_1 + z_2 \frac{N D_1}{Z D_2}. \quad (70)$$

To elaborate the influence of the new orthogonal modes on the individual ion modes we rewrite z_1 and z_2 in terms of v and u . For this we introduce a new constant $\alpha = 1 + \frac{\beta N D_1^2}{Z D_2^2}$. Note that $\alpha \propto N$. After some algebra, we come up with

$$z_1 = \frac{u + v(\alpha - 1)}{\alpha} \quad \text{and} \quad z_2 = \frac{u - v \beta D_1}{\alpha D_2}. \quad (71)$$